In medium static quark anti-quark potential from lattice QCD

by

Gaurang Parkar

Thesis submitted in fulfilment of
the requirements for the degree of
PHILOSOPHIAE DOCTOR
(PhD)

Faculty of Science and Technology
Department of Mathematics and Physics
2024

University of Stavanger
NO-4036 Stavanger
NORWAY
www.uis.no

ISBN: 978-82-8439-253-0
ISSN: 1890-1387
PhD: Thesis UiS No. 775

Preface

This thesis is submitted in partial fulfilment of the requirements for the degree of Philosophie Doctor (PhD) at the University of Stavanger, Faculty of Science and Technology, Norway. The research has been carried out at the University of Stavanger from August 2019 to the date of submission of this thesis.

First of all I would like to thank the University of Stavanger and the Norwegian research foundation for providing me with the resources and the funding to pursue my PhD. I am grateful to the HISQ and HotQCD collaboration for providing me with data and computing resources and for fruitful discussions during our weekly meetings. I would also like to thank Bjørn Auestad for being a very kind and helpful institute leader. I would like to thank my office mates Abhijit, Oleg, Jonas, Gerhard, Magdalena, Divya, Paolo, Vegard for wonderful discussions on very obscure and random topics and sometimes wasting precious time from a workday. It was crucial for providing mental support during stressful times. I would like to thank my group members Alexander (Lehmann), Rasmus and Daniel for having long and fruitful discussions which were very valuable in providing with new ideas which I had not considered before. Lastly, I would like to thank for supervisor Alexander Rothkopf for conceptualizing ideas for my project and providing guidance over the course of the last four years.

Gaurang Parkar
Stavanger, February 2024

Abstract

In this thesis we present recent progress in the quest to study the properties of the quark gluon plasma in relativistic heavy ion collisions through a better understanding of the binding of heavy quark and anti-quark pairs (quarkonium). We present two studies investigating the complex binding potential between heavy quarks using non-perturbative lattice QCD simulations and modern data analysis techniques that were contributed to and performed as a part of this PhD project. The first study utilizes state of the art simulations with 2+1 flavours of dynamical light HISQ quarks. This study revealed a complex potential with an unscreened real part. Its results were in stark contrast to previous studies on quenched and full QCD lattices which had all shown a complex potential with a screened real part. This unusual result motivated a second study, where we re-investigated the potential on high resolution quenched lattices to confirm their robustness using the same methods deployed in the full QCD study. We found that the analysis techniques applied to the raw correlators confirms previous results, i.e. resulting in a complex potential with a screened real part. Applying the same analysis after performing a recently proposed subtraction procedure leads instead to an unscreened potential akin to the first study on HISQ lattices.

Table of Contents

1 Introduction

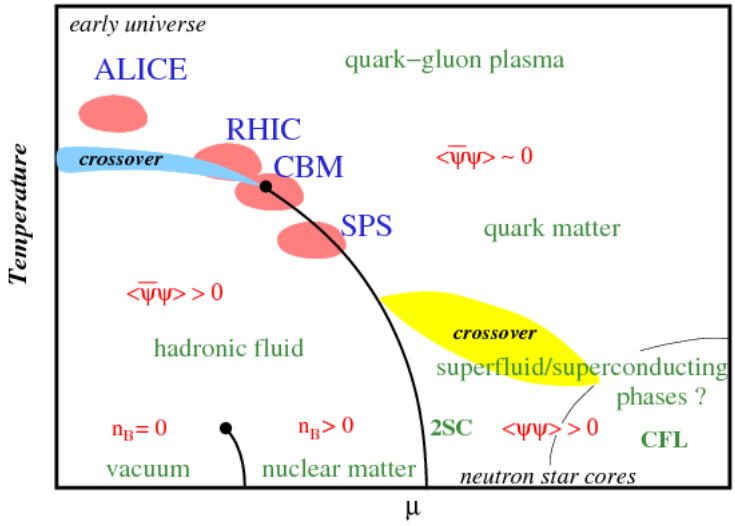

Figure 1.1: A schematic representation of the QCD phase diagram taken from [1].

Quantum Chromodynamics (QCD) is the theory of the strong force which describes interactions between quarks and gluons. It predicts that nuclear matter undergoes a phase transition at temperatures present shortly after the BigBang and thus plays a central role in cosmological models [2] of the early universe. Cosmological models of the early universe predict that several phase transitions have taken place, the QCD confinement-deconfinement phase transition which occurs at $T \approx$ 155MeV is of particular interest to this thesis. As the universe cools near this transition temperature, the quarks and gluons transition from a deconfined *quark-gluon plasma* (QGP) phase to a confined phase consisting of hadrons. The study of the QCD phase diagram which includes the confinement-deconfinement phase transition has been of great theoretical interest over the past three decades. Figure 1.1 shows a schematic representation of the QCD phase diagram as a function of temperature T and chemical potential μ. It was postulated that this phase transition can also be studied experimentally in relativistic

heavy-ion collisions at RHIC at Brookhaven National Lab (gold-gold collisions) and LHC (ALICE, CMS and ATLAS) at CERN (lead-lead collisions). In addition to heavy-ion collisions and early universe, the deconfined quarks and gluons are also predicted to exist in the interior of neutron stars [3]. The focus of this thesis is, however, to study the properties of quark gluon plasma in heavy-ion collisions.

Due to advancement in computing power in recent years, lattice QCD simulations have contributed substantially in understanding the QCD phase diagram (see [4] for a recent review on the current state of progress). The following are some of the key findings: It was established that the transition was a crossover phase transition with a transition temperature of T_c = 156.5MeV at zero chemical potential. Furthermore, the equation of state was calculated [5] and used as an input in the hydrodynamical models of the QGP [6].

1.1 Phenomenology of Heavy-ion collisions

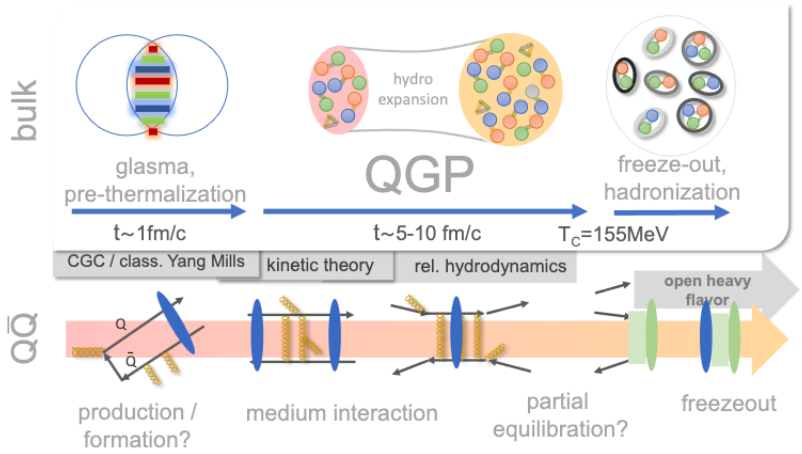

Figure 1.2: A schematic picture of different stages of heavy ion collisions showing a life cycle of heavy quarkonium (bottom) and the relevant effective field theory (grey) at each stage. The figure has been taken from [7] courtesy A. Rothkopf.

A lot of work has gone into understanding different stages of heavy ion collisions sketched in fig. 1.2. In heavy ion collisions gold (Au) or lead (Pb) nuclei are accelerated to ultra relativistic energies and collided to create matter which is high in energy density but low in baryon density. The model of colour glass condensate [8] (CGC) has been used to describe these heavy ion collisions. In this model, at the instant of collision the partons (sea of quarks and gluons) are able to interact with each other, generating strong colour electric and magnetic field called *glasma*. These strong fields then break down into light quarks and gluons. After a short pre-thermalization phase (around 1 fm) equilibriate into the quark gluon plasma (QGP) through energy and momentum exchanges. The evolution of the quark gluon plasma can be described hydrodynamically [9]. It expands and cools over the crossover transition of T_c = 156.5MeV[10] below which it enters the hadronic phase consisting of mesons and baryons in what is called *chemical freeze out*. These continue to interact until the *kinetic freeze out* is reached.

This dynamical picture of heavy-ion collisions is described not through a direct computation of QCD but, instead through effective field theory (EFT), which have been developed to capture physics at different stages of heavy-ion collisions as there exist clear separation of scales in the system. The grey boxes in fig. 1.2 describe these EFT's. Classical Yang-Mills can explain the behaviour at the earliest stage and the evolution continues into kinetic theory and finally into relativistic hydrodynamics.

We now introduce the concept of hard-probes to study the quark-gluon matter in heavy ion collisions. The terms *hard* and *soft* refers to different well separated scales. These probes can be produced in the collision and serve as indicators of the properties of the medium like temperature, viscocity, energy density and transport coefficients [11]. Hard probes measured by the CMS and ATLAS experiments at the LHC are jets, quarkonium, and electroweak gauge bosons .

This thesis focuses on heavy quarkonium, the bound state of quark

and anti-quark pair. For charm constituent quarks they are referred to as charmonium, for bottom constituents as bottomonium states. Here the hard scale refers to the mass of heavy quarks (m_c = 1.3GeV and m_b = 4.6GeV). The goal of studying quarkonium production is its use as gauge of temperature in the coloured medium created in heavy-ion collisions.

In experiment, the deviations in measured yields between say a p + p collision to that of any other type of collision p + A or A+A is expressed via the nuclear modification factor R_{xA} given by

$$R_{xA}\left(p_T\right) = \frac{1}{\langle N_{\text{coll}} \rangle} \frac{dN_{xA}/dp_T}{dN_{pp}/dp_T}, \tag{1.1}$$

where p_T is the transverse momentum and the prefactor $< N_{coll} >$ is the total number of binary collisions necessary for correct normalization. If the system simply reflects a scaled up version of p-p collisions this ratio would be unity.

A quarkonium bound state may be formed during the pre-thermalization phase of the collision, and then interacts with the hot medium during the QGP phase. Being in the presence of the hot medium will reduce its interaction strength and the state can either survive the medium or it could *melt* (the $q\bar{q}$ pair gets decorrelated) depending on the energy and time-scales. If enough pairs are present then quarkonium pairs can also be regenerated at hadronization. If the medium has long enough lifetime then the heavy quarks could also equilibriate with the surroundings. After leaving the QGP phase some of the quarkonium states decay into a lowest lying (vacuum) state and make its way to the detector. Due to presence of separation of scales that we will discuss later, the quarkonium in vacuum can be treated non-relativistically and its states can be classified using the schemes as atomic physics using spin, angular momentum and total spin $^{2S+1}L_J$. The commonly studied states are S-wave ground states called Υ (bottomonium) and J/ψ (charmonium). In addition excited S-wave states and P-wave states $^3P_1$, χ_{c1} and χ_{b1} are also relevant. Dilepton-yields in PbPb-collisions

at $\sqrt{S_{NN}}$ = 5.02 TeV have been studied in [12] and are shown in fig. 1.3 with the nuclear modification factor shown in fig. 1.4. The different peaks denote the ground state $\Upsilon(1S)$ and the following excited states $\Upsilon(2S)$ and $\Upsilon(3S)$. The peak positions in the figure represent the masses of the bound states. The suppression of these excited states in Pb-Pb collisions as opposed to p-p collisions can be explained by the presence of the QGP, which arises due to the partial melting bound state with the hot environment.

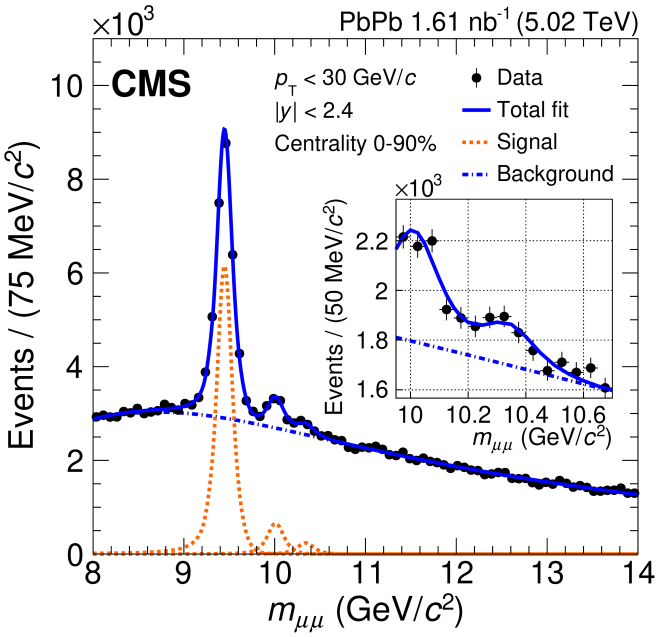

Figure 1.3: Dimuon yields of and PbPb collisions as measured in [12]. The solid curves show the result of the fit, whereas the orange dashed and blue dash-dotted curves represent the three Υ states and the background, respectively.

The binding energies of quarkonium states are $E^{\Upsilon}_{\text{bind}} \approx 1.1$ GeV and $E^{J/\psi}_{\text{bind}} \approx 0.64$ GeV which are obtained by subtracting ground state energies from the open heavy flavour threshold. This high binding energy of the quarkonium bound state compared to the medium can be repro-

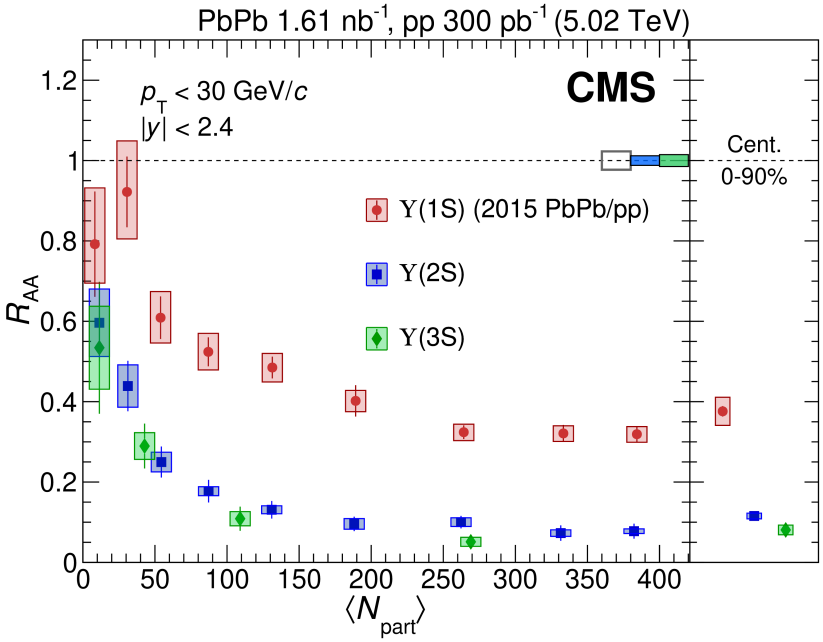

Figure 1.4: Nuclear modification factors for $\Upsilon(1S)$ $\Upsilon(2S)$ and $\Upsilon(3S)$ meson production in PbPb collisions, as a function of centrality, displayed as the average number of participating nucleons as measured in [12].

duced by a simple potential model called the *Cornell potential*. The Cornell potential contains a Coulombic part at small distances followed by linearly rising one at larger distances, terminating in a constant part after string-breaking. These states provide us with a direct connection between experiment on one side and a microscopic description of QCD on the other.

The seminal work by Matsui and Satz [13] presented inightful ideas about the production of heavy quarkonium. It presented two key ideas:

- The presence of the deconfined medium in heavy ion collisions will interfere with the binding of the heavy quarks through color

screening and thus prevent formation of a bound state.

- The absence of a bound state will lead to a supression of quarkonium yields.

Their paper however, does not make a prediction about quarkonium yields after hadronisation. In addition, the authors of [14] made model calculations which predicted the mass shift from below the phase transition.

The quarkonium states that we want to study in the QGP can only be measured in experiment after hadronisation. A first principles computation of hadronisation from QCD has not been achieved, however several models inspired by QCD are used in phenomenology. Thus, in practice, the yield of J/ψ in heavy-ion collisions can instead be well described by the statistical model of hadronisation [15; 16] and has been confirmed by observations at LHC [17]. The statistical model argues that at energy scales of LHC charmonium production is the smoking gun for deconfinement [16] and even if no charmonium states survive the QGP phase, hadronization at the phase boundary of the many tens of charm quarks expected in a single central Pb-Pb collision could lead to an enhanced, production probability when compared to nucleon-nucleon reactions scaled by the number of hard collisions in the Pb-Pb system. Thus, the study of the evolution of quarkonium bound states is the key in establishing a theoretical description of the QGP.

1.2 Effective theories of heavy quarkonium

In the previous section we have seen examples of how evolution of the quarkonium bound state can serve as a probe for QGP phase in heavy-ion collisions. However, the study of the dynamical properties of these bound states present two key challenges. The first one being that the temperatures involved in the confinement-deconfinement transitions are beyond the range where standard perturbative calculations work due to strong coupling of QCD. This issue can be overcomed by using non perturbative lattice QCD calculations. This, in turn brings us to the

second challenge i.e. methods of calculating dynamical quantities directly on the lattice from real-time simulations has not yet been well established due to the presence of the notorious sign problem. Significant efforts are being made to reduce the severity of the sign problem and there has been a lot of effort in recent years trying to overcome the sign problem (see [18] for a recent review). However, these efforts are still far away from being able to simulate QCD. Thus, we instead, resort to effective field theory descriptions to extract information at different relevant energy scales if they are well separated. The EFT framework let's us study the physics of quarkonia through a potential which can be then obtained from QCD using a matching procedure. The task of computing this potential is easier than that of simulating the full theory.

To simplify our case we first start at zero temperature, where there is a clear separation of scales present i.e. the mass of the heavy quark M is much larger than its relative velocity v. In addition to this scale the mass of the heavy quark is also greater than Λ_{QCD}. Thus we can exploit these separations now i.e $M >> mv >> mv^2$ and $M >> \Lambda_{QCD}$. First we integrate out the *hard scale* M, doing this makes the energies of the quark and gluon fields less than what is required for the creation of a heavy quark anti-quark pair. The absence of pair creation eventually results in an effective theory that is non-relativistic called NRQCD [19; 20]. NRQCD gives us a non-relativistic approximation to the Dirac Lagrangian. The lagranginan is formulated by expansion in a dimensionless parameter v which is the relative velocity of the heavy quark. We start by removing the rest mass from the total energy by a field redefinition

$$\Psi(x) = e^{-iMc^2t}\tilde{\Psi} \tag{1.2}$$

This modification still fullfills the Dirac equation. Then we can break up the Dirac four spinors into two two-spinors

$$\bar{\Psi} = \begin{bmatrix} \psi \\ \chi \end{bmatrix} \tag{1.3}$$

Inserting into the dirac equation and since the theory is non-relativistic we can ignore higher order terms of $1/c$ since c is greater than any velocity that appears in the theory we obtain

$$\chi = \frac{i}{2Mc}\vec{\sigma}.\vec{D}\psi. \tag{1.4}$$

Here $\vec{\sigma}$ is the pauli matrix. We can now insert back into the Dirac lagrangian and obtain the lagrangian for the ψ field given by

$$L_\psi(x) = \bar{\psi}(x)\big(iD_0 + \frac{1}{2M}(i\vec{D}^2) + \frac{g}{2Mc}\vec{\sigma}.\vec{B}\big)\psi(x) \tag{1.5}$$

Here $B_i = \epsilon_{ijk}F^{jk}$ is the chromomagnetic field. The total lagrangian for NRQCD is therefore

$$\begin{aligned}\mathcal{L}_{\text{NRQCD}} =&\psi^\dagger\left[iD_0 + \frac{c_\text{k}}{2M}\vec{D}^2 + \frac{c_\text{F}}{2M}\vec{\sigma}\cdot(g\vec{B}) + \frac{c_\text{D}}{8M^2}(\vec{D}\cdot(g\vec{E}) - (g\vec{E})\cdot\vec{D})\right.\\
&\left.+i\frac{c_\text{S}}{8M^2}\vec{\sigma}\cdot(\vec{D}\times(g\vec{E}) - (g\vec{E})\times\vec{D})\right]\psi\\
&+\chi^\dagger\left[iD_0 - \frac{c_\text{k}}{2M}\vec{D}^2 - \frac{c_\text{F}}{2M}\vec{\sigma}\cdot(g\vec{B}) + \frac{c_\text{D}}{8M^2}(\vec{D}\cdot(g\vec{E}) - (g\vec{E})\cdot\vec{D})\right.\\
&\left.+i\frac{c_\text{S}}{8M^2}\vec{\sigma}\cdot(\vec{D}\times(g\vec{E}) - (g\vec{E})\times\vec{D})\right]\chi\\
&+\mathcal{L}^{(2)}\Big|_{4f} + \mathcal{L}_\text{G} + \mathcal{L}_\text{light} + O\left(M^{-3}\right)\end{aligned} \tag{1.6}$$

Here $E_i = F_{0i}$ is called the chromo-electric field. The term $\mathcal{L}_g$ is the lagrangian consisting of only gauge fields and $\mathcal{L}_{light}$ comprises of the light fields. These two terms remain unaffected by the NRQCD approximation. The spectrum of the Υ system was investigated using the Lattice NRQCD approach to heavy quarks and ignoring light quark vacuum polarization in [21].

We can further focus on the binding properties of the heavy quark antiquark pair at the ultrasoft scale Mv^2 by integrating out the soft scale mv, which is a theory of color singlet S and octet O wavefunctions, called potential NRQCD or pNRQCD [22]. In this theory we have two cutoffs, $M > \Lambda^p_{EFT} > Mv$ for the spacial momentum and $Mv >$

Λ^2_{EFT} for the energy of the heavy quarks. Instead of writing fields in terms of $\psi(x)$and $\chi(x)$ it is helpful to instead consider the Quarkonium wavefunctions to establish a power counting scheme:

$$\Psi(x_1, x_2, t)_{ab} \sim \psi(x_1, t)_a \chi\,\dagger\,(x_2, t)_b \tag{1.7}$$

This object can be further decomposed into singlet S and octet O wavefunctions.

$$\begin{aligned}
&\Psi\left(\mathbf{x}_1, \mathbf{x}_2, t\right) = \Psi(\mathbf{r}, \mathbf{s}, t) = \\
&\mathcal{P}\left[\exp\left\{ig\int_{\mathbf{x}_1}^{\mathbf{x}_2}\mathbf{A}d\mathbf{z}\right\}\right] S(\mathbf{r}, \mathbf{s}, t) \\
&+\mathcal{P}\left[\exp\left\{ig\int_{\mathbf{R}}^{\mathbf{x}_1}\mathbf{A}d\mathbf{z}\right\}\right] O(\mathbf{r}, \mathbf{s}, t)\mathcal{P}\left[\exp\left\{ig\int_{\mathbf{x}_2}^{\mathbf{R}}\mathbf{A}d\mathbf{z}\right\}\right]
\end{aligned} \tag{1.8}$$

This form makes the transformation of the S and O under colour rotations by ultrasoft gluons explicit. The choice of quark mass to be used in these equations is an area of active research. In addition to this the gauge fields that remain explicit degrees of freedom appear in pNRQCD appear in the lagrangian as a multipole expansion. Thus, the general pNRQCD lagrangian can be written in terms of singlet and octet wavefunctions as

$$\begin{aligned}
\mathcal{L}_{\text{pNRQCD}} = \int d^3\mathbf{r}\mathrm{Tr}\Big[S^\dagger\big[i\partial_0 - \big(\frac{\mathbf{D}^2}{2M} + V_S^{(0)} + \frac{V_S^{(1)}}{m_Q} + \dots\big)\big]S + \\
O^\dagger\big[iD_0 + \frac{\mathbf{D}^2}{2M} + V_O^{(0)} + \frac{V_O^{(1)}}{m_Q} + \dots\big)\big]O\Big] + \\
V_A(r)\mathrm{Tr}\Big[O^\dagger\mathbf{r}g\mathbf{E}S + S^\dagger\mathbf{r}g\mathbf{E}O\Big] + \\
V_B(r)\mathrm{Tr}\Big[O^\dagger\mathbf{r}g\mathbf{E}O + O^\dagger O\mathbf{r}g\mathbf{E}\Big] + O\big(r^2, \frac{1}{m_Q^2}\big) + \\
\mathcal{L}_{light\ quarks,gluons}
\end{aligned} \tag{1.9}$$

The quantity r describes the separation distance between the heavy-quark and anti quark pair. The first two terms in the equation look like

a Schrödinger-like equation in which the gluonic terms integrated out appear as Wilson coefficients in the form of time-independent potential terms V_S and V_O. For the purpose of our studies we will restrict ourselves to the static potential which are just the first terms ($V_S^{(0)}$ and $V_S^{(0)}$) in the expansion of powers of inverse mass. In addition to this, in the third and fourth terms we have the gluonic contribution which manifests itself in dipole-like interactions arising between the colour singlet S and colour octet O governed by Wilson coefficients V_A and V_B. These effects are considered to be non-potential effects. In the situation when $mv^2 \ll \Lambda_{QCD}$ the non-potential terms can be absorbed into the time-independent potential terms and it can be shown that the potential is now just the static energy [22], which can be computed from lattice correlation functions.

So far, all the considerations that we have made is at zero temperatures. At finite temperature the problem gets more complicated as there are additional energy scales involved. At asymptotically high temperature (weak coupling) the hierarchy of $T \gg m_D \approx gT \gg gT^2$ holds. These thermal affects can affect the pNRQCD picture in a non-trivial way with affecting both the potential and non-potential terms. Thus, it needs to be established whether the potential holds for finite temperature, and if it does, how must its form be modified.

At this point, it is worth noting that in addition to effective field theory (EFT) descriptions there has been developments in understating the evolution of heavy quarkonia using the open quantum systems approach [23; 24; 25; 26; 7; 27]. In this approach the degrees of freedom are separated into an environment E and a small subsystem S. In this case the thermal QCD medium represents the environment and the small subsystem S represents the two body quarkonium system which is described by a total hermitian hamiltonian. This hamiltonian can be further decomposed into H_E which contains only the effects of the environment E and H_S which only contains the effects of S. The time evolution of the system can now be studied through the evolution of the density matrix. Since we are not interested in studying the evolution

of the medium we can trace over the medium degrees of freedom and obtain the reduced density matrix σ_S for S. The equation of motion for σ_S is knows as the GKS or Lindblad equation. This approach has been used to reveal the subtle interplay between screening and decoherence in a hot QCD medium.

1.3 Wilson loop and the potential

We now describe how the potential can be related to observables computed from the QCD lagrangian. We first need to connect the EFT description of quarkonium to QCD by identifying correlation functions with the same physics content in both pictures called matching. We begin by defining the Wilson-loop in Minkowsiki time

$$W_{\square}(t,r) = \langle \exp[ig \int_{\square} dz^{\mu} A_{\mu}] \rangle_{\mathrm{QCD}} \tag{1.10}$$

The integration is carried out over temporal distance t and spacial distance r. The fields A^a_μ are the gauge fields in by the $SU(3)$ algebra described by the generators T^a. It has been shown that in the static limit $m_Q \to \infty$ at zeroth order in the multipole expansion the Wilson loop is the appropriate quantity which we can identify with the unequal time correlation function of two color singlet fields in pNRQCD [22].

$$W_{\square}(t,r) \equiv \langle S(0,r) S^{\dagger}(t,r) \rangle_{\mathrm{pNRQCD}}. \tag{1.11}$$

This Wilson loop has been computed perturbatively [28] by selecting a specific hierarchy of energy scales (involving the system temperature), which is captured by the resummed perturbation theory called hard-thermal loops (HTL). The authors showed that in the late real-time limit, a weakly coupled Wilson loop at finite temperature evolves solely according to a Schrödinger-like equation

$$\lim_{t\to\infty} i\partial W_{\square}(t,r) = \lim_{t\to\infty} \Phi(t,r) W_{\square}(t,r) = V_{\square}(r) W_{\square}(t,r) \tag{1.12}$$

The quantity $V_{\square}(r)$ is the time independent potential which was shown to be complex. The quantity $\Phi(t,r)$ contains both potential and non-potential effects. The static time-independent potential can thus be

defined as

$$V_{\square}(r) = \lim_{t\to\infty} \frac{i\partial_t W_{\square}(t,r)}{W_{\square}(t,r)} \tag{1.13}$$

The authors of [28] also showed that the complex potential in HTL has a screened real part.

Note that the potential defined above is only for the singlet and it is also possible to describe the octet potential. The potential described by the limit in eq. (1.13) has been calculated perturbatively, and it is unclear whether or not such a limit would exist in a fully non-perturbative setting since the potential is defined as a late time limit of the Wilson loop in Minkowski time and it is not directly established how this translates to in the euclidean time setting which we have access to non perturbatively. In this thesis we will investigate the existence of this limit and try to identify the real and imaginary parts of this potential.

1.4 Lattice QCD

Lattice QCD has been the state of the art tool available to access the evolution of quarks and gluons at both zero and finite temperatures using numerical methods combined with high performance computing to simulate the path integral non perturbatively. In this formalism space-time is discretized into a four dimensional grid. In contrast to the traditional way where one deals with the gauge fields A^a_μ which lies in the $SU(3)$ algebra, in this approach we instead consider the link variables

$$U_\mu(x) = \exp[-igA^a_\mu(x + a/2)T^a] \tag{1.14}$$

which now live in the group. Since the gauge fields can be interpreted as parallel transport of quarks, these link variables are placed on the links of the spacetime grid and fermions are placed on the nodes of the grid. The UV cutoff of the theory is now automatically introduced in

terms of the finite lattice spacing and the IR cutoff is introduced from the fact that now there is a finite box size which corresponds to the number of lattice points in each direction.

The path integral is approximated stochastically from this formalism using Monte Carlo simulations where gauge configurations are generated with probabilities proportional to the negative exponential of the action. Due to the notorious sign problem, the simulations cannot be carried out in minkowski time and thus one has to perform a wick rotation into imaginary (euclidean) time. The lagrangian in euclidean space-time can be obtained by modifying the QCD lagrangian by $L_E = -L(t \rightarrow i\tau, A \rightarrow iA_4)$ which has the form

$$L_E(\bar{\psi}, \psi, A_i) = \frac{1}{4g^2} F^a_{i,j} F^a_{i,j} + \sum_{f=1}^{N_f} \bar{\psi}^f_{\alpha,a}((\gamma_i)_{\alpha\beta}(D_i)_{a,b} + m^f \delta_{\alpha\beta}\delta_{ab})\psi^f_{\beta,b} \tag{1.15}$$

The index i runs from 1 to 4 with 4 being the imaginary time index. We also need to introduce the Euclidean form of the Dirac matrices, $\gamma_4 = \gamma^M_0$ and $\gamma_i = -i\gamma^M_i$ where γ^M are the gamma matrices in minkowski space. The Euclidean Dirac matrices follow the anti commutation relations $\{\gamma_i, \gamma_j\} = \delta_{ij}$.

We are interested in the physics at finite temperature which we will do by making the imaginary time axis periodic. The path integral representation of the partition function above with inverse temperature β (1/T) and volume V can be written as

$$\begin{aligned} Z(T,V) &= \int D[U] D\psi D\bar{\psi} \exp\left(- \int_0^\beta d\tau \int_V d^3x L_E \right) \\ &\equiv \int D[U] D\psi D\bar{\psi} e^{-S_E} \end{aligned} \tag{1.16}$$

Here the discretised bosonic fields obey periodic boundary conditions in τ while the fermionic fields obey anti-periodic boundary conditions.

The finite extent of the spacial axes is a discretisation artifact while the finite extent of the temporal axis represents the temperature of the system. In practice all lattice simulations are at finite temperatures as we can only have a finite box size. The T=0 simulations are done by making the box size in the temporal direction large enough that the effects are negligible. The $D[U]$ is the *Haar measure* integrating over link variables in $SU(3)$ space. The term e^{-S_E} can be interpreted as an unnormalised probability distribution and can be simulated using monte carlo simulations. The expectation values of operators can thus be easiely calculated;

$$\begin{aligned}\langle O\left(\tau_1, \tau_2, \ldots\right)\rangle &= \frac{1}{Z}\,\mathrm{Tr}\left[e^{-\beta H}\hat{O}\left(\tau_1, \tau_2, \ldots\right)\right] \\ &= \frac{1}{Z}\int \mathcal{D}[U]\int \mathcal{D}[\psi,\bar{\psi}]O\left(U,\psi,\bar{\psi},;\tau_1,\tau_2,\ldots\right)e^{-S_E}\end{aligned} \tag{1.17}$$

The lattice action contains two terms, i.e. the gauge part and the fermion part. There are several discretisation schemes that have been developed which all converge to the right action (lagrangian from eq. (1.15)) in the limit that lattice spacing goes to zero. The simplest choice for gluonic fields is the Wilson plaquette action given by

$$S_E^g = \frac{\beta}{N_c}\sum_{\mathbf{n}}\sum_{i=1}^{4}\sum_{j<i}\left(\frac{1}{\xi_0}\,\mathrm{Re}\,\mathrm{Tr}\left[1 - U_{ij}(\mathbf{n})\right] + \xi_0\,\mathrm{Re}\,\mathrm{Tr}\left[1 - U_{0i}(\mathbf{n})\right]\right). \tag{1.18}$$

The above action is the general action for anisotropic lattices (spacial lattices spacing is different from temporal lattices spacing) with bare anisotropy parameter ξ_0. The quantity $U_{\mu\nu}(n)$ is called the plaquette which is defined as the product of link variables eq. (1.14) and can be represented as

$$U_{\mu\nu}(\mathbf{n}) = U_\mu(\mathbf{n})U_\nu(\mathbf{x}+\hat{\mu})U_\mu^\dagger(\mathbf{n}+\hat{\nu})U_\nu^\dagger(\mathbf{n}). \tag{1.19}$$

In recent years there have been some developments in the gauge action that make numerical problems less severe when implementing chiral

fermions [29]. Also, it was found that using the improved gauge action is numerically advantageous for the Dirac operator. The Luscher-Weisz gauge action was developed with coefficients from tadpole improved perturbation theory. In addition to the plaquette term of the Wilson action, the Luscher-Weisz action includes a sum over all 2×1 rectangles and a sum over all parallelograms, i.e. all possible closed loops of length 6 along the edges of all 3-cubes.

$$S[U] = \beta_1 \sum_{pl} \frac{1}{3} \mathrm{Re\,Tr} \left[1 - U_{pl}\right] + \beta_2 \sum_{rt} \frac{1}{3} \mathrm{Re\,Tr} \left[1 - U_{rt}\right] \tag{1.20}$$

$$+ \beta_3 \sum_{pg} \frac{1}{3} \mathrm{Re\,Tr} \left[1 - U_{pg}\right] \tag{1.21}$$

where β_1 is the principal parameter while β_2 and β_3 can be computed from β_1 using one loop perturbation theory and tadpole improvement [30]. We will use this improved gauge action for our study in chapter 3.

The fermionic part of the action gauge invariant and is expressed in terms of grassmann valued quark fields. Directly representing these fields as matrices can prove quite costly so, instead we exploit the fact that the fermionic part of the action only has bilinear terms and carry out a gaussian integral over the fields. This results in the fermion determinant. This determinant can be expressed as a path integral over bosonic fields given by

$$\begin{aligned} Z &= \int \mathcal{D}[U] \int \mathcal{D}[\bar{\psi}, \psi] \exp\left\{ - \int dx \bar{\psi} K \psi \right\} e^{-S_E^g} \\ &= \int \mathcal{D}[U] \det K[U] e^{-S_E^g} = \int \mathcal{D}[U] \frac{1}{\det K^{-1}[U]} e^{-S_E^g} \\ &= \int \mathcal{D}[U] \int \mathcal{D}[\phi] e^{-S_E^g - \phi^* K^{-1}[U] \phi}. \end{aligned} \tag{1.22}$$

Naively placing fermionic fields on the lattice results in more fermionic states than expected which is called the *fermion doubling* problem

that is deeply connected to chiral symmetry breaking on the lattice explained by the Nielsen-Ninomiya theorem [31; 32]. Various discretisation schemes have thus been proposed like introducing staggered fermions and improved versions of it like the highly improved staggered quark action (HISQ) [33] and Wilson fermions [34]. Wilson fermions are more advantageous since explicitly break chiral symmetry but is generally not used due to the large computational costs associated. We have used the HISQ action for our study of the potential in full QCD. There are however some drawbacks of using the HISQ action are two fold : they have a reminisce of chiral symmetry still remaining so they don't completely get rid of the doublers and the second one is that it introduces non-monotonicitiy in the effective masses of the Wilson line correlator which is a manifestation of positivity violation in the spectral function. We will get back to this issue later on in the thesis in chapter 3.

The path integral is now estimated stochastically via Monte Carlo simulations in which a computer is used to generate configurations with a probability distribution which corresponds to the Euclidean Feynman weight. For the purpose of efficiently choosing configurations hybrid monte carlo schemes have been developed which the update is combined with solving Hamiltonian's equation of motion for fermions and gluons. If the number of configurations is large enough, the central limit theorem says that the the resulting probability distribution will be gaussian. Thus, after initial thermalization one can compute the ensemble average as the mean of observable O along the Markov chain of length N.

$$\langle O \rangle = \frac{1}{N} \sum_{i=1}^{N} O_i. \tag{1.23}$$

For the purposes of reducing computational costs, only the light quarks u , d and s are considered dynamically. In the vocabulary of lattice field theory literature the dynamical fermion content as $N_f = 2 + 1$ indicate the mass degenerate fermions u and d and the single massive s

quark. Sometimes, to further reduce computational costs the fermions are not treated dynamically and the fermion determinant is set to unity. This is known as the *quenched* approximation. In this thesis we will present studies on both quenched and $2+1$ flavour QCD.

Once the observables are computed from a lattice simulation, the results need to be extrapolated to vanishing lattice spacing $a_\mu \to 0$ to recover the continuous spacetime physical theory. In addition to this the thermodynamic limit $V \to \infty$ must also be taken. In practice, the continuum limit is taken by running simulations for different values of a while keeping the volume constant and then extrapolating to $a \to 0$. The a dependence of the simulation can also be computed from a scaling analysis and thus we can extrapolate to the infinite volume limit.

1.5 Wilson Loop and Spectral structure

In section 1.3 we have defined the static potential via the Wilson loop correlation function in real time.

$$\lim_{t\to\infty} i\partial W_\square(t,r) = \lim_{t\to\infty} \Phi(t,r) W_\square(t,r) = V_\square(r) W_\square(t,r) \tag{1.24}$$

However, in practice a lattice simulation is done in euclidean time or imaginary time and thus generally do not have direct access to this information except for the zero temperature case where one the limit $\tau \to \infty$ can be taken to get the limit of $t \to \infty$. For this purpose the spectral decomposition has been established non-perturbatively by taking the infinite mass limit of the point split heavy-meson correlation function [35]

$$W_\square(t,r) = \int_{-\infty}^{\infty} d\omega\ \rho_\square(\omega,r)\, e^{i\omega t}. \tag{1.25}$$

It has been proposed that this decomposition[36] links the real time Wilson loop correlator to the imaginary time correlator calculated on

the lattice via the same positive definite spectral function given by

$$W_\square(t,r) = \int_{-\infty}^{\infty} d\omega\, \rho_\square(\omega,r)\, e^{i\omega t} \quad \Longleftrightarrow W_\square(\tau,r) = \int_{-\infty}^{\infty} d\omega\, \rho(\omega,r) e^{-\omega\tau}. \tag{1.26}$$

Thus the potential can be extracted from the spectral function via

$$V(r) = \lim_{t\to\infty} \frac{\int_{-\infty}^{\infty} d\omega\ \omega\ e^{-i\omega t}\ \rho_\square(\omega,r)}{\int_{-\infty}^{\infty} d\omega\ e^{-i\omega t}\ \rho_\square(\omega,r)}. \tag{1.27}$$

By definition, the Wilson loop (in both continuum and on the lattice) exhibits a simple behavior under time reversal. As a complex quantity, it turns into its complex conjugate which follows from the spectral decomposition in eq. (1.26)

$$W_\square(-t,r) = W^*_\square(t,r) \tag{1.28}$$

This relation arises from the fact that $W_\square$ is defined from an exponentiation of Hermitian matrices multiplied with the imaginary unit and thus is valid non-perturbatively.

We will now follow the footsteps of calculations proposed in [37] and derive a functional form for the spectral function and link the real and imaginary parts of the potential to the position and width of the dominant peak in the spectral function. If we assume that the limit in eq. (1.13) is well defined we may then define a characteristic time scale t_{relax} beyond which the the function $\Phi(t,r)$ reduces to the time independent $V(r)$. Below we will confirm that t_{relax} indeed is connected to the region in time over which non-potential effects remain relevant for the evolution of the Wilson loop.

We may therefore *without loss of generality* write $\Phi(t,r) = V(r)+\phi(t,r)$ with $\phi(t > t_{\text{relax}}, r) = 0$[1] Since, as an SU(3) group element, the Wilson

[1]If we instead had an arbitrary relation $\Phi(t,r) = F[V(r);t,r]$ with $F[V(r);t > t_{\text{relax}},r] = V(r)$ we may always define the function $\phi(t,r)$ as $\Phi(t,r) = V(r) - (F[V(r);t,r] - V(r)) \equiv V(r) - \phi(t,r)$.

loop can only take on finite values the imaginary part of of the potential $Im[V](r) < 0$ must be negative.

Following this splitting up of the $\Phi(t,r)$ into a time dependent ($t < t_{relax}$) and independent part ($t > t_{relax}$) and plugging it into the definition of the potential

$$i\partial_t W_\square(t,r) = \Phi(t,r) W_\square(t,r), \tag{1.29}$$

we arrive at a general functional form

$$W_\square(t,r) = \exp\Big[-i\Big(\mathrm{Re}[V](t)t + \mathrm{Re}[\sigma](t,r)\Big) - |\mathrm{Im}[V](r)|t + \mathrm{Im}[\sigma](t,r)\Big]. \tag{1.30}$$

We have introduced the quantity $\sigma(t,r) = \int_0^t \phi(t,r)dt$ making reference to the function $\phi(t,r)$ and which thus asymptotes to $\sigma_\infty(r) = \sigma(|t| > t_{\mathrm{relax}}, r) = \int_0^\infty \phi(t,r)dt$.

As the spectral decomposition amounts to a simple Fourier transform, it can be readily inverted to yield

$$\rho_\square(r,\omega) = \frac{1}{2\pi}\int_{-\infty}^{\infty} dt\, \exp\Big[i\Big(\omega - \mathrm{Re}[V](r)\Big)t - i\mathrm{Re}[\sigma](r,|t|)\mathrm{sign}(t) - |\mathrm{Im}[V](r)||t| + \mathrm{Im}[\sigma](r,|t|)\Big] \tag{1.31}$$

Under the assumption that the function $\sigma(t,r)$ asymptotes to a constant for times $t > t_{\mathrm{relax}}$, we may decompose the integral into two parts, one over times smaller then $|t| < t_{\mathrm{relax}}$ and one over the whole time range

$$\begin{aligned}\rho_\square(r,\omega) = \qquad & (1.32)\\ \frac{1}{2\pi} e^{\mathrm{Im}[\sigma_\infty](r)} & \int_{-\infty}^{\infty} dt\, \exp\Big[i\Big(\omega - \mathrm{Re}[V](r)\Big)t - |\mathrm{Im}[V](r)||t| - i\mathrm{Re}[\sigma_\infty](r)\mathrm{sign}(t)\Big]\\ + \frac{1}{2\pi}\int_{-t_{Q\bar{Q}}}^{t_{Q\bar{Q}}} & dt\, \exp\Big[i\Big(\omega - \mathrm{Re}[V](r)\Big)t - |\mathrm{Im}[V](r)||t|\Big]\times\\ & \left(e^{-i\mathrm{Re}[\sigma](r,|t|)\mathrm{sign}(t) + \mathrm{Im}[\sigma](r,|t|)} - e^{-i\mathrm{Re}[\sigma_\infty](r)\mathrm{sign}(t) + \mathrm{Im}[\sigma_\infty](r)}\right).\end{aligned}$$

This decomposition now reveals how the potential emerges in the spectral structure. The integral involving integration over the whole time regime can be carried out analytically and becomes a skewed Lorentzian peak located at the position of the real-part of the potential, its width being related to imaginary part. Around the maximum of that peak $(\omega - Re[V])t_{\text{relax}} \ll 1$ we can expand the remaining integral over the finite time regime in a Taylor series leading to a background for the potential peak

$$\rho^{\text{pot}}_{\square}(r,\omega) = \frac{1}{\pi} e^{\text{Im}\sigma_\infty](r)} \frac{|\text{Im}[V](r)|\cos[\text{Re}[\sigma_\infty](r)] - (\text{Re}[V](r) - \omega)\sin[\text{Re}[\sigma_\infty](r)]}{\text{Im}[V](r)^2 + (\text{Re}[V](r) - \omega)^2} + c_0(r) + c_1(r) t_{Q\bar{Q}}(\text{Re}[V](r) - \omega) + c_2(r) t^2_{Q\bar{Q}}(\text{Re}[V](r) - \omega)^2 + \cdots \tag{1.33}$$

If one reinserts $\rho^{\text{pot}}_{\square}$ into the relation eq. (1.27) one finds that only the pole in the skewed Lorentzian matters and indeed a time independent complex potential $V(r) = \text{Re}[V](r) - i\text{Im}[V]$ ensues.

In practice we attempt to extract a spectral function from lattice QCD simulations, inspect it for a dominant low lying structure and wish to understand, whether it leads to a well defined potential $V(r)$. This requires to reverse the above argumentative chain.

Let us start with shape of such a dominant spectral peak. The Lorentzian derived in eq. (1.33) contains extended tails in the high ω region. We can ask if the presence of tail structures have any relevance to the time-independentness of the potential. Instead taking e.g. a Gaussian $\rho_{\text{G}}(\omega, r) = A(r)\exp[-(\omega - m(r))^2/g^2(r)]$ and inserting into eq. (1.27) one finds that it does not lead to a well defined potential, as a time dependent and even divergent imaginary part ensues $V_G(r,t) = m(r) - ig(r)^2 t$. This result shows that tail structures play an important role in establishing a time independent potential.

Let us now consider the low ω region of the spectral function. If we naively insert the derived skewed Lorentzian in the Euclidean version

of the spectral decomposition eq. (1.26), we find that the integral does not converge due to the low ω tails present the the Lorentzian. Thus, in addition to the Lorentzian around the peak and at high ω, we also need a spectral function that is exponentially suppressed at very low ω to satisfy the spectral decomposition. Such a cut Lorentzian was used as an ansatz for the spectral function in [38]. The Gaussian does not suffer from this low ω convergence problem, but, still cannot be naively used as a model for spectral function due to reasons presented in the paragraph above. We will later present a new approach which allows us to consider a Gaussian spectral function.

In lattice simulations one extracts the potential using the temporal Wilson line correlator in coulomb gauge

$$W(r,\tau,T) = \frac{1}{3}\left\langle \mathrm{Tr}\left(L(0,\tau)L^{\dagger}(r,\tau)\right)\right\rangle_{T} \tag{1.34}$$

where $L(r,\tau) = \exp\left(i\int_0^{\tau} A_4\,(r,\tau')\,d\tau'\right)$ instead of the Wilson loop. It has been shown that considering the Wilson line instead of the Wilson loop does not change the static potential in hard thermal loop perturbation theory (see below) and has also been argued for non-perturbatively. Considering the Wilson line instead of the Wilson loop has technical advantages over the Wilson loop in reconstructing the spectral function that we discuss below. However, measuring the Wilson line correlator on the lattice requires gauge fixing to Coulomb-gauge which increases computational cost. For this purpose the SimulateQCD code was developed which performs these calculations very fast and efficiently on multiple GPU's [39].

In order to get insight onto the tail structures, we can use the hard thermal loop (HTL) spectral functions as a concrete and non-trivial example. While the real-time evolution of the Wilson loop does not place strict restrictions on the tail structure of the potential peak (i.e. the integral $W_{\square}(t,r) = \int_{-\infty}^{\infty} d\omega\ \ \rho_{\square}(\omega,r)\,e^{i\omega t}$ is well defined for a skewed Lorentzian), the Euclidean counterpart of the spectral decom-

position

$$W_{\square}(\tau, r) = \int_{-\infty}^{\infty} d\omega\, \rho_{\square}(\omega, r)\, e^{-\omega\tau} \tag{1.35}$$

requires the spectral function to be exponentially suppressed at negative frequencies, incompatible with a naive Lorentzian peak. As shown in fig. 2.2 the HTL Wilson loop spectral function computed from the real-time correlator, indeed shows exactly this exponential suppression, which cuts off the tails of the dominant skewed Lorentzian potential peak. Note that this cut-off spectrum is compatible with our non-perturbatively derived decomposition in eq. (1.32) and tells us that it is the non-potential effects which affect the low frequency spectral structure. It is important to note that this modification of the Lorentzian peak at negative frequencies *does not* introduce an additional pole at small frequencies that would interfere with the late time limit. I.e. in HTL the Lorentzian potential peak is exponentially cut off but remains the relevant structure for the asymptotically late-time evolution of the charge-anticharge pair.

The example of the HTL spectral function is encouraging. It supports the conclusion that if one finds a dominant lowest lying spectral peak in a lattice spectral function, with a skewed Lorentzian behavior around its maximum, this peak is likely to encode the asymptotic late real-time behavior of the real-time correlator, even if the spectral function is exponentially suppressed at negative frequencies.

Accurately determining the existence of a low lying, well defined spectral peak and reconstructing its shape with high fidelity from simulated Euclidean lattice data is therefore of importance to clarify the existence of a time-independent potential.

1.6 Organisation and goal of this thesis

The goal of this thesis is thus to clarify the existence of a time-independent static potential through determining the lowest lying peak

of the spectral function. For this end, the thesis is organised as follows:

- In chapter 2 we discuss different methods that we will use to extract the spectral function from Euclidean correlators obtained from lattice simulations at finite temperatures. We then proceed to benchmark these methods on analytically computed Wilson loop and Coulomb-gauge Wilson line correlators from computed hard-thermal loop (HTL) perturbation theory. These HTL Wilson loop and Wilson line spectral function serve as a non-trivial testing ground for the reliability and robustness of these methods. We also briefly review the recently developed subtraction procedure.
- In chapter 3 we show the extracted peak position and width (real imaginary part of the potential respectively) on state of the art, 2+1 flavours of dynamical light HISQ quark lattices using the methods showcased in the previous chapter. The results obtained were quite unusual. Unlike previous studies on quenched and full QCD lattices, we found that the real part of the potential was unscreened showing no temperature dependence.
- Following the unusual results of the study on HISQ lattices, motivated a second study showcased in chapter 4. In this study we re-investigated the potential on high resolution quenched lattices using the same methods deployed in the full QCD study. We found that the analysis techniques applied to the raw correlators confirms previous results, i.e. resulting in a complex potential with a screened real part. Applying the same analysis after performing a recently proposed subtraction procedure leads instead to an unscreened potential akin to the first study on HISQ lattices.
- Lastly in chapter 5 we will summarize our results and comment on some of the questions that arise which would be an avenue for future work.

2 Extracting spectral functions and the the static interquark potential from Lattice QCD

[1]As discussed in the previous chapter the reconstruction of the lowest lying peak of the spectral function from lattice QCD is the key challenge in estimating the static quark potential. At zero temperature, we expect the vacuum ground state is well separated from the excited states and the underlying spectral function is just a sum of well separated delta peaks. To this order we construct a function called the effective mass of the euclidean correlator

$$m_{eff}(\tau) = \frac{1}{a} \log \left[\frac{W(\tau)}{W(\tau + 1)} \right] \tag{2.1}$$

which will approach a plateau with the value of the ground state mass M_0 at some intermediate τ (see fig. 2.1). This plateau can easily be extracted by a constant fit to m_{eff} in the region where the plateau is observed. The effects from excited states are observed in the curvature present in the effective masses at small τ where the plateau has not yet been reached (see small τ region in fig. 2.1). The static potential is not affected by theses excited states so in our case we are not very interested in recovering the information about the excited states.

At finite temperatures these delta peaks can cluster together to form a broad peak with a finite width possibly with some skewedness. The effective masses will do not plateau at intermediate τ and instead continues to monotonically decrease. Some more sophisticated methods thus need to be developed for spectral reconstructions, which would amount to inverting the relation in eq. (1.35) whose discretised form can be written as

[1]Most of the contents of this chapter have been taken from a preprint [40] where the author has contributed substantially towards writing, generation of data, analysis of data and with figure creation.

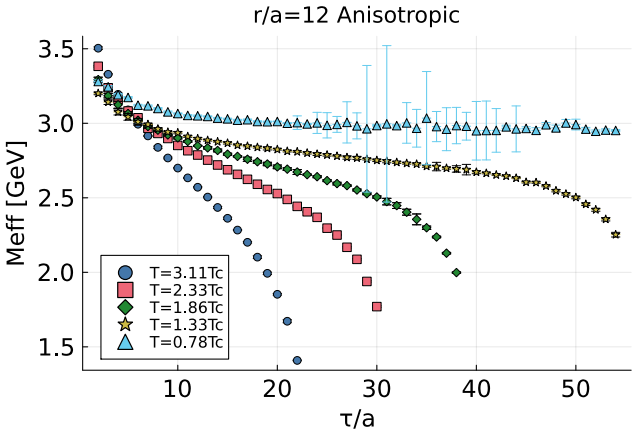

Figure 2.1: A representative selection of effective masses, obtained from the Coulomb-gauge Wilson line correlator computed on anisotropic ($\beta = 7, \xi = 4$) quenched lattices.

$$W_i = \sum_{l=1}^{N_\omega} \Delta\omega_l K_{jl} \rho_l, j \in [1, N_\tau] \tag{2.2}$$

A lattice simulation provides N_τ discrete values of the correlator $W(\tau_j) = W_j$ along the imaginary axis for each value of separation distance. Each of these discrete data points for the correlator has a finite statistical error ΔW_j. On the other hand we need to obtain a high enough resolution to $\rho(\omega)$ discretised to N_ω points to be able to reliably identify the relevant structures in the spectral function. Thus we require that $N_\omega \gg N_\tau$. In a realistic lattice simulation one usually has $N_\tau = 10 - 100$ while $N_\omega \sim O(1000)$ is required. The task of inverting eq. (2.2) in the presence of a limited number of noisy data-points makes the problem ill-posed since there are more parameters than the available data-points. In addition to this, in QCD the kernel K_{jl} function also contains an exponential decay making the problem ill conditioned i.e. an infinite number of solutions exists for the inversion.

In order to have any hope of reconstruction the right positive definite

$\rho(\omega)$ some additional prior information needs to be provided. This information must be incorporated by using some arguments motivated by physics and for this specific problem QCD. In this chapter, we present and benchmark four different approaches that we will deploy in the study of the in-medium static quark potential presented in this thesis: Bayesian inference [41], Padé interpolation [42], the HTL-inspired fit [43; 44] and generalized Gaussian fits on the subtracted correlator [45].

As non-trivial testing ground we deploy the analytically computed Wilson loop and Coulomb-gauge Wilson line correlators from hard-thermal-loop perturbation theory [46] at $T = 2.33T_C$, whose spectral functions are known. We evaluate the Euclidean data at the same number of discrete imaginary time steps accessible on the lattice and salt it with Gaussian noise with constant relative errors similar (or larger) than those encountered in actual simulations, providing us with a realistic mock input data set.

In the top panel of fig. 2.2 we show four spectral functions $\rho_{||}^{\mathrm{HTL}}(\omega, r)$ of the Coulomb-gauge Wilson line correlator at different spatial distance $r \in [0.065 \ldots 0.46]\mathrm{fm}$. A dominant skew-Lorentzian peak encoding the potential is located in a weak shoulder structure, which decays exponentially at small and algebraically at large frequencies. In case of the Wilson loop spectral function $\rho_{\square}^{\mathrm{HTL}}(\omega, r)$ shown in the bottom panel, we find peaks at the same position and with the same width as in $\rho_{||}^{\mathrm{HTL}}$ but with amplitudes significantly suppressed with increasing distance. In addition the peak is embedded into a substantial background, which extends far into the UV region at high frequencies at a significant fraction of the peak amplitude [46]. I.e. the different correlators encode the same potential but very different non-potential effects.

Their values from the HTL Wilson lines and Wilson loop at three spatial distances are given in the top and bottom plot of fig. 2.3 respectively. You can see that the dominant spectral peak in $\rho_{||}$ in the absence of a strong UV contibution leads to an m_{eff} that is almost linear around the middle of the imaginary time interval $\tau = 1/(2T)$ with some curvature

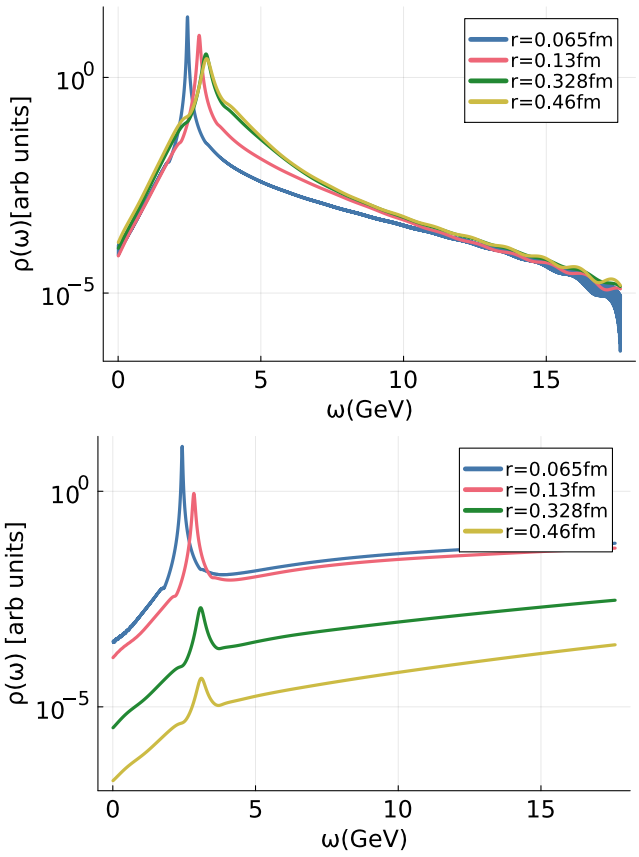

Figure 2.2: Semi-analytically computed spectral function of the (top) Coulomb-gauge Wilson line correlator and (bottom) Wilson loop in HTL perturbation theory at $T = 2.33T_C$. The four curves denote spectra at different spatial separation distances. The figure shows the HTL spectral functions for Wilson lines (top) and Wilson loop (bottom) for four different separation distances.

at early and late τ. Contrast this to the Wilson loops, where the substantial UV contribution leads to a strong curvature at small τ, which overshadows the linear behavior at intermediate imaginary times, before another region of strong curvature from the low frequency tail of the spectrum induces a downward trend at $\tau \approx 1/T$.

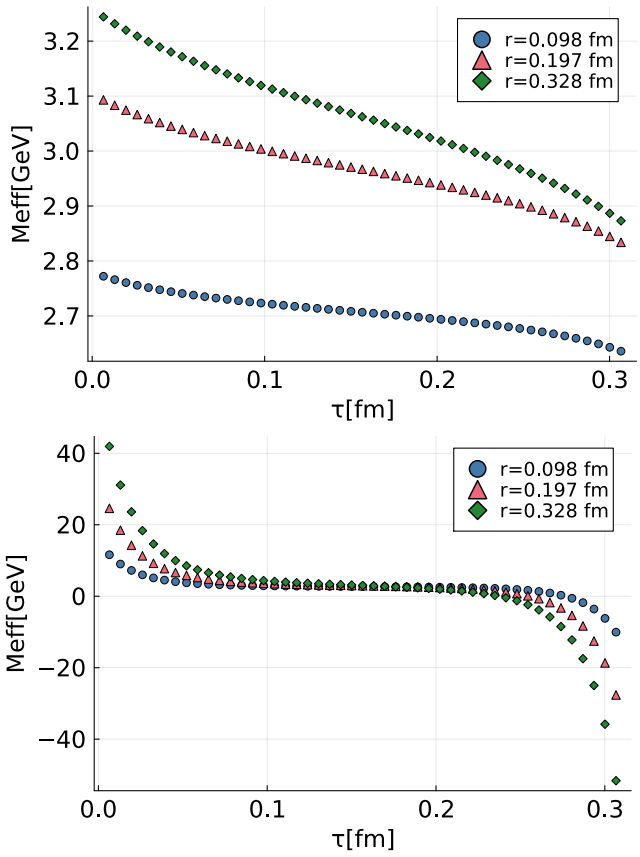

Figure 2.3: Effective masses from the (top) Coulomb-gauge Wilson line correlator and (bottom) Wilson loop at $T = 2.33T_C$ in HTL perturbation theory.

In fig. 2.4 we show a direct comparison of the effective masses of the Wilson loop and Coulomb-gauge Wilson lines at a single $r = 0.131$fm to illustrate that their behavior resembles limiting cases for the behavior of effective masses observed in actual lattice simulations.

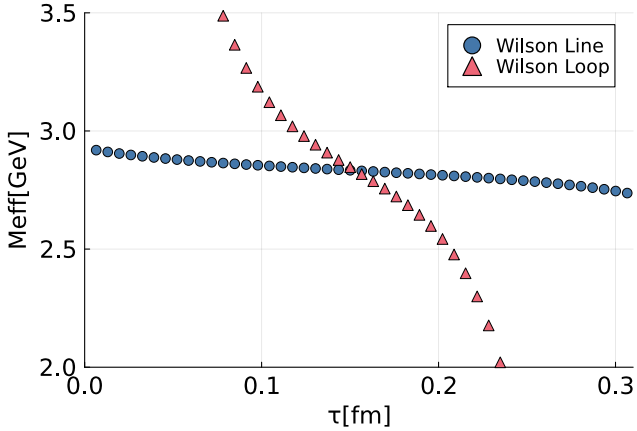

Figure 2.4: A comparison of HTL effective masses of the Wilson loop (triangle) and Coulomb-gauge Wilson lines correlator at $T = 2.33T_C$ evaluated at a separation distance of $r = 0.131$fm. Both encode the same spectral peak position and width related to the common value of the complex static quark potential. Their behaviors constitute limiting test cases for the effective masses observed in actual lattice QCD simulations.

2.1 Bayesian spectral reconstruction

Bayesian inference of spectral functions builds upon Bayes theorem

$$P[\rho|D,I] \propto P[D|\rho,I]P[\rho|I] = \exp[-L+\alpha S], \tag{2.3}$$

to introduce prior domain knowledge on the spectral function to regularize the inverse problem. The posterior $P[\rho|D,I]$ describes the probability of a test function ρ to be the correct spectral function given correlator data $D_i = W(\tau_i, r)$ and prior information I. It is expressed as product of the Gaussian likelihood $P[D|\rho,I]$, which describes the distribution of the sampled data and connects the estimated mean of the correlator to the spectral function via eq. (1.35)

$$L = \frac{1}{2}\sum_{i,j=1}^{N_d}(D_i - W[\rho]_i)C_{ij}^{-1}(D_j - W[\rho]_j). \tag{2.4}$$

where C_{ij} denotes the covariance matrix of the data with respect to the mean and in absence of autocorrelations given by

$$C_{jk} = \frac{1}{N_{\text{conf}}\ (N_{\text{conf}}\ -1)} \sum_{m=1}^{N_{\text{conf}}} \left(D_j^m - D_j\right) \left(D_k^m - D_m\right), \tag{2.5}$$

and $W[\rho]_i = \int_{-\infty}^{\infty} d\omega\, \rho(\omega, r)\, e^{-\omega\tau_i}$. It is the prior probability $P[\rho|I] = e^{\alpha S}$ that acts as the regulator. It is through this regulator that we introduce domain knowledge about our system. The maximum of the posterior $\frac{\delta P[\rho|D,I]}{\delta\rho} = 0$ provides the best estimate of ρ, which is known as the Bayesian solution to the inverse problem.

Historically, the Maximum entropy method (MEM) has been used for Bayesian spectral reconstruction on lattice QCD data. It is based on four underling assumptions, *locality, coordinate invariance, system independence* and *scaling*. For a more detailed discussion of these assumptions and MEM in general see [47]. After taking these assumptions into account, one can construct the Shannon-Jaynes entropy axiomatically which is plays the role of prior information.

$$S_{\text{SJ}} = \int_0^{\infty} \left[\rho(\omega) - m(\omega) - \rho(\omega) \log\left(\frac{\rho(\omega)}{m(\omega)}\right)\right] d\omega \tag{2.6}$$

Here $m(\omega)$ is known as the default model, which, is the correct spectral function in the absence of data. The hyperparameter α is treated in the Bayesian sense by first computing several different spectral functions ρ^{α} for different values of α and then averaging out, weighted by the evidence $P[D \mid I] = P[D \mid \alpha, m]$ giving us a best estimate of the spectral function.

The MEM has several key issues which affect its reliability and applicability on real-world lattice data: slow convergence of the underlying optimization task, high computational cost for extended search spaces, scale dependence in the prior functional and the Gaussian approximation required in the hyperparameter estimation.

To address these issues a new Bayesian approach was proposed by the authors of [41]. This approach is based on slightly different set of assumptions namely, *subset independence, scale invariance* (these two are the same as MEM), *smoothness of reconstructed spectra* and *maximum at the prior*. After taking these into consideration one can derive the BR prior, related to the gamma-distribution

$$S_{\mathrm{BR}} = \int d\omega \big(1 - \frac{\rho(\omega)}{m(\omega)} + \log\big[\frac{\rho(\omega)}{m(\omega)}\big]\big), \tag{2.7}$$

This regulator is 'weaker' than the Shannon-Jaynes entropy in MEM. It therefore allows information encoded in the data to manifest easily in the reconstructed ρ, but at the same time is more susceptible to ringing artifacts[2] compared to stronger regulators. The hyperparameter α is integrated out from the joint probability distribution $P[\rho, D, \alpha, m]$. I.e. we consider the influence of all possible prior distributions in the resulting posterior probability $P[\rho \mid D, m]$, on which we base the reconstruction. Starting from the multiplication law for probabilities:

$$\begin{aligned} P[\rho, D, \alpha, m] &= P[D \mid \rho, \alpha, m] P[\rho \mid \alpha, m] P[\alpha, m] \\ &= P[\alpha \mid \rho, D, m] P[\rho \mid D, m] P[D, m], \end{aligned} \tag{2.8}$$

we integrate both r.h.s with respect to α. We set out to find an expression for the α independent

$$P[\rho \mid D, m] = \frac{P[D \mid \rho, I]}{P[D \mid m]} \int d\alpha P[\rho \mid \alpha, m].$$

For large values of S, we approximate the integral over α through a next-to leading order resummation of logarithms, while for small S a numerical evaluation is possible. After integration all the alpha dependence is removed, we evaluate the maximum of the posterior using quasi-Newtonian LBFGS algorithm. This regulator does not have any asymptotically flat directions allowing us to always locate the extremum.

[2] See fig. 2.6 for an explicit demonstration of these ringing artifacts.

We have also explored a different approach in the handling of α akin to the Morozov criteria used in Tikhonov regularisation [48]. In this approach, we tune α such that the likelihood takes the value of $L = N_\tau/2$. The motivation for this approach is that we avoid using very large and very small values of α to contribute to the end result. We have noticed that this approaches diminishes some of the ringing artifacts from the BR method. However, we did not find any significant differences in the extracted potential for different handling of α where ringing artifacts were not observed, i.e. the data on HISQ lattices [49] and Quenched lattices.

The explicit dependence of the posterior on the data and prior assumptions allows to test the uncertainties in each of them by carrying out a resampling (Jackknife) analysis and by repeating the analysis for different choices of the default model $m(\omega)$. For a more detailed discussion of the BR method see [41].

We carry out the Bayesian spectral function reconstruction on the analytically computed raw correlator data discretized along $N_\tau = 24$ datapoints representative for the N_τ accessible on the lattice. We discard the first and last point, as those are also discarded in lattice data due to the presence of divergent contributions. We assign constant relative errors $\Delta D/D = \kappa$ with $\kappa = 10^{-2}$ or $\kappa = 10^{-3}$ and will show in the next section that $\kappa = 10^{-3}$ is actually achieved in our lattice data.

The reconstruction with $\Delta D/D = 10^{-2}$ from $W_{||}$ manages to locate the peak position already excellently (see section 2.1), since a single peak dominates the spectrum. For $W_\square$ the position of the peak is less accurately determined (see fig. 2.8). Note that the true position of the peak from the Bayesian reconstruction is found to *be approached from above*. It is the structures that exists above the Lorentzian peak which pull the reconstructed peak to higher frequencies. This is an important finding, as it tells us that even in the presence of large non-potential effects the true peak position is likely lying at or slightly below the reconstructed value.

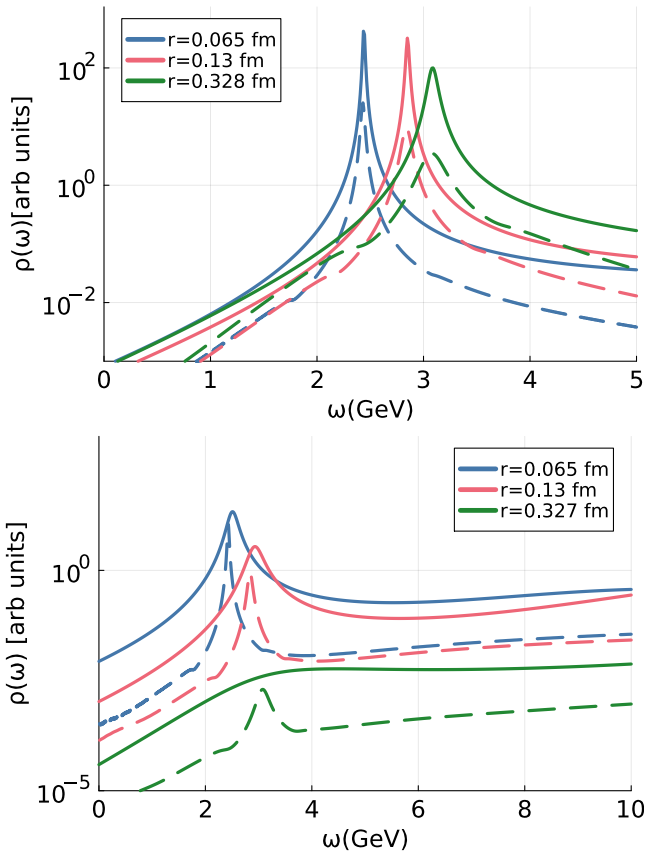

Figure 2.5: Bayesian inference reconstructed (solid line) and semi-analytical (dashed line) spectral functions of the (top) Coulomb-gauge Wilson line correlator $\rho_{||}$ and (bottom) Wilson loop $\rho_{\square}$ in HTL perturbation based on 22 datapoints with $\Delta D/D = 10^{-2}$. The three curves each denote spectra at different spatial separation distances.

Interestingly the width of the potential peak is underestimated when reconstructed from $W_{||}$ and overestimated when using $W_{\square}$. Thus the Wilson loop and line results bracket the correct imaginary part.

Let us take a look at the reconstruction results when the errors on the input data is reduced to $\Delta D/D = 10^{-3}$ in fig. 2.6. The Wilson loop reconstructions in the bottom panel show a significant improvement

compared to the $\Delta D/D = 10^{-2}$ case. In the top panel we can also see an improvement in the reconstruction from $W_{||}$ at small distances r but find the occurrence of ringing at $r = 0.327$fm. The true single peak structure is split up into two structures, one lying below, one above the true peak. Reducing the errors on the input data without at the same time increasing the number of datapoints thus may lead the reconstruction method to favor such a multipeak structure. If we were to take the position of the lowest structure as indicative of Re[V] it would induce a significant jump between $r = 0.13fm$ and $r = 0.327$fm.

We learn from the mock analysis that for the Bayesian reconstruction method when studying lattice data, we need to test for ringing artifacts. To this end we will repeat the reconstructions at different levels of $\Delta D/D$ and check whether at some point single peaks split into multiple structures. Let us note at this point that these crosschecks show that the lattice data analysis presented in the next chapters does not suffer from ringing. One may ask how susceptible the reconstruction is to adversarial attacks, such a by supplying false prior information in the form of peak structures in the default model. In fig. 2.7 we show the robustness of the Bayesian reconstruction against a set of artificial peaks located both above and below the true peak position. At $\Delta D/D = 10^{-3}$ and $N_\tau = 24$ the presence of adversarial peak located above the true position leaves the position of the reconstructed dominant peak relatively unaffected, however when the adversarial peak is located below the true position we see a shift in the reconstructed peak at a slightly higher value.

After a qualitative inspection of spectral reconstructions, let us plot the corresponding extracted values of Re[V] and $Im[V]$ from fitting the dominant peak with eq. (1.33) in fig. 2.8. It is reassuring that even in the presence of very strong non-potential effects in $\rho_\square$ the Bayesian reconstruction appears able to quantitatively accurately reproduce the real part of the potential with the number of datapoints and errorlevels accessible to us in our studies.

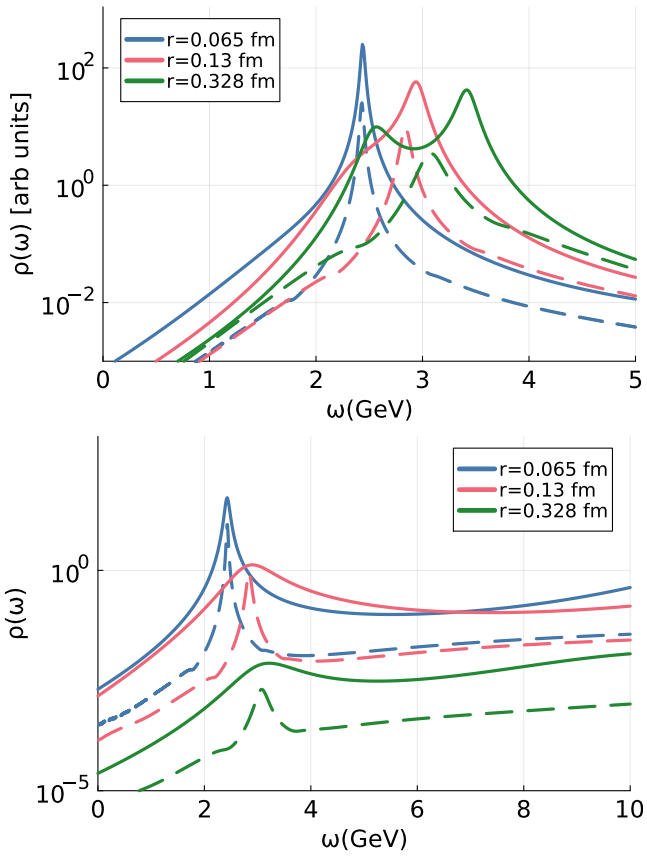

Figure 2.6: Bayesian inference reconstructed (solid line) and semi-analytical (dashed line) spectral functions of the (top) Coulomb-gauge Wilson line correlator $\rho_{||}$ and (bottom) Wilson loop $\rho_{\square}$ in HTL perturbation based on 22 datapoints with $\Delta D/D = 10^{-3}$. The three curves each denote spectra at different spatial separation distances.

2.2 Spectral reconstruction using Padé

The Padé approach approximates the Matsubara correlators by a rational function interpolation. These rational function approximation approaches have been known since the 1890s, but have traditionally not been used for spectral reconstruction as they require very precise data with low errors. It has only been possible to get enough statis-

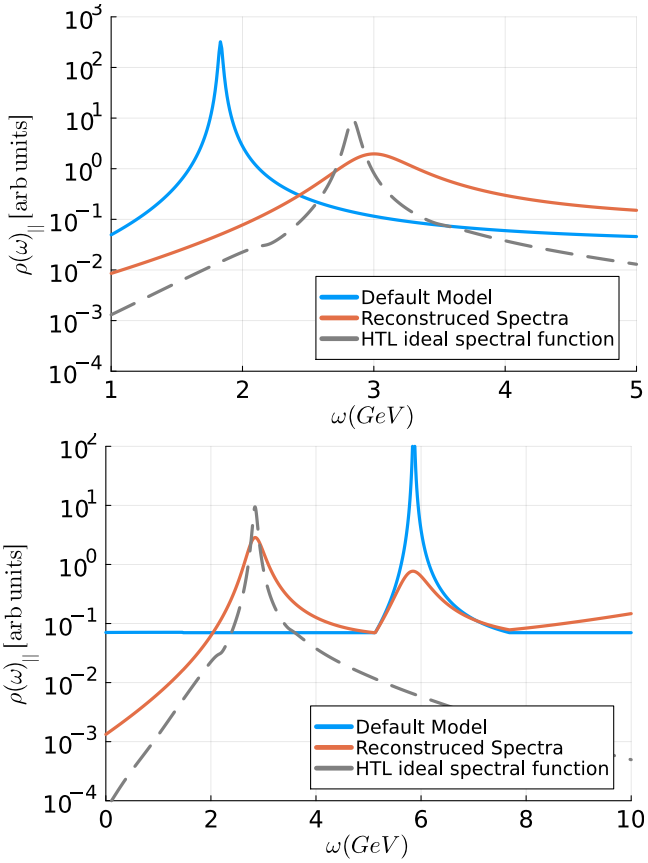

Figure 2.7: Bayesian inference reconstructed (solid line) and semi-analytical (dashed line) spectral functions of the (top) Coulomb-gauge Wilson line correlator $\rho_{||}$ in HTL perturbation theory based on 22 datapoints with $\Delta D/D = 10^{-2}$ at a separation distance of 0.13 fm. The reconstruction has been carried out with an artificial adversarial peak inserted in the default model (blue).

tics in the recent years. The Bayesian approaches which have been more standardly used for spectral reconstruction are only applicable when the underlying spectral functions are positive definite. The Padé approach can accommodate non-positive spectral functions. Since we have reasonably high statistics for our studies, Padé approach is applicable.

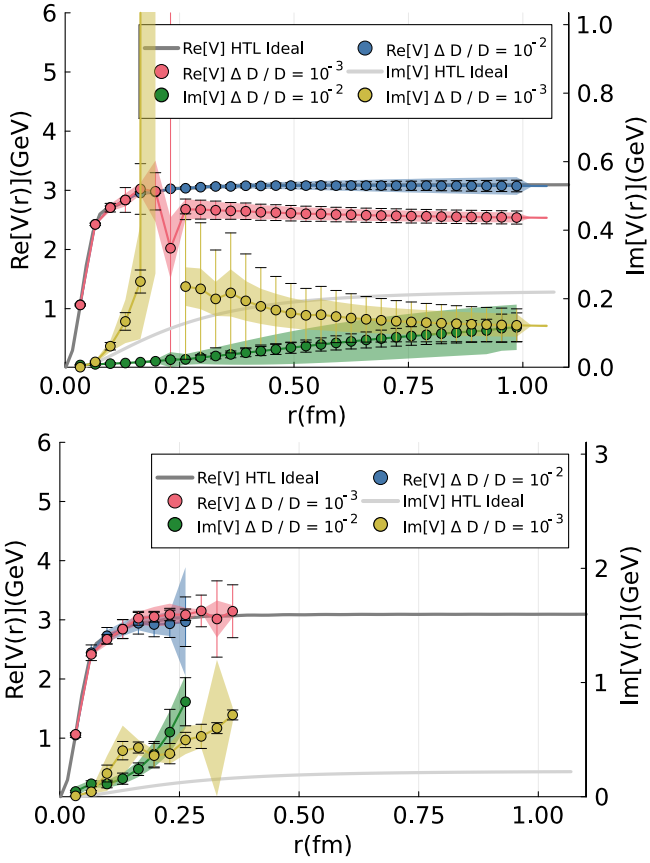

Figure 2.8: Bayesian inference reconstructed (colored symbols) and analytic (solid line) values for the real- and imaginary part of the complex static quark potential from the (top) Coulomb-gauge Wilson line correlator $V_{||}(r)$ and (bottom) Wilson loop $V_{\square}(r)$ in HTL perturbation based on 22 datapoints with $\Delta D/D = 10^{-2}$ and $\Delta D/D = 10^{-3}$.

In this approach, we first start but Fourier transforming the euclidean data to the Matsubara frequency space. We can now exploit the analyticity of the Lehmann kernel to carry out the continuation to real-time

$$W(r, \tilde{\omega}_n, T) = \int d\omega \frac{1}{\omega - i\tilde{\omega}_n} \rho_r(\omega, T). \tag{2.9}$$

where, the Fourier transformed data is given by the following expression

$$W(r, \tilde{\omega}_n, T) = \sum_{j=0}^{N_\tau - 1} e^{ia\tilde{\omega}_n j} W(r, ja, T), \;\; \tilde{\omega}_n = 2\pi n / aN_\tau. \tag{2.10}$$

We then project the data on a set of rational basis function according to the Schlessinger prescription [42]. This methods interpolates the data into a rational function where the order of the polynomial is higher in the denominator than the numerator by at least one. This ensures the right asymptotic behaviour of the correlator large frequencies. An added advantage of interpolation is that it amounts to solving a simple linear equation and avoids costly minimization. One big disadvantage is however, that since we do not add an explicit regulator as in Bayesian approaches, it is prone to over-fitting.

The naive discreet Fourier transform as defined in equation eq. (2.10) does not reproduce the Lehmann kernel eq. (2.9), but instead also contains effects due to finite lattice spacing and finite volume. To compensate for this issue, we used improved frequencies which correspond to the eigenvalues of the momentum operator.

$$\tilde{\omega}_n \rightarrow \omega_n = 2\sin\Big(\frac{\pi n}{N_\tau}\Big)/a \tag{2.11}$$

Now that we have the required frequencies and the Fourier transformed correlator we can represent the matsubara correlator as a rational function

$$W(r, \tilde{\omega}_n, T) = \frac{p_N(r, \tilde{\omega}_n, T)}{q_M(r, \tilde{\omega}_n, T)}, n = 1, \ldots N + M + 1. \tag{2.12}$$

Here $N + M + 1$ is the total number of points used for interpolation and

$$p_N(r,\tilde{\omega}_n,T) = \sum_{k=1}^{N} p_k \omega_n^k \tag{2.13}$$

$$q_M(r,\tilde{\omega}_n,T) = 1 + \sum_{k=0}^{M} q\omega_n^k. \tag{2.14}$$

Now, the interpolation problem reduces to solving a system of $N+M+1$ linear equations as shown in equation eq. (2.12). Instead of solving the linear equations we use a continued fraction prescription C_{N_τ} (both these approaches are equivalent) of the form used by Schlessinger

$$C_{N_\tau}(r,i\omega,T) = \frac{W(r,\omega_0,T)}{1+}\frac{a_0(r,T)[\omega-\omega_0]}{1+}\frac{a_1(r,T)[\omega-\omega_1]}{1+} \\ \ldots\frac{a_{N_\tau-2}(r,T)[\omega-\omega_{N_\tau-2}]}{1+}a_{N_\tau-1}(r,T)[\omega-\omega_{N_\tau-1}]. \tag{2.15}$$

This formula can be better understood in the following way:

$$\frac{A}{1+}\frac{B}{1+}C \equiv \frac{A}{1+\frac{B}{1+C}} \tag{2.16}$$

The complex coefficients of equation eq. (2.15) can be determined recursively by imposing the condition that each data point passes exactly through C_{N_τ}. The recursive formula is given by

$$a_n(r,T)(\omega_{n+1}-\omega_n) = -\Big\{1+ \\ \frac{a_{n-1}(r,T)[\omega_{n+1}-\omega_{n-1}]}{1+}\frac{a_{n-2}(r,T)[\omega_{n+1}-\omega_{n-2}]}{1+}\ldots \\ \ldots\frac{a_0(r,T)[\omega_{n+1}-\omega_0]}{1-[W(r,\omega_0,T)/W(r,\omega_{n+1},T)]}\Big\}. \tag{2.17}$$

Following this interpolation method in fig. 2.9 we plot the real (top panel) and imaginary part (bottom panel) of the HTL Coulomb gauge

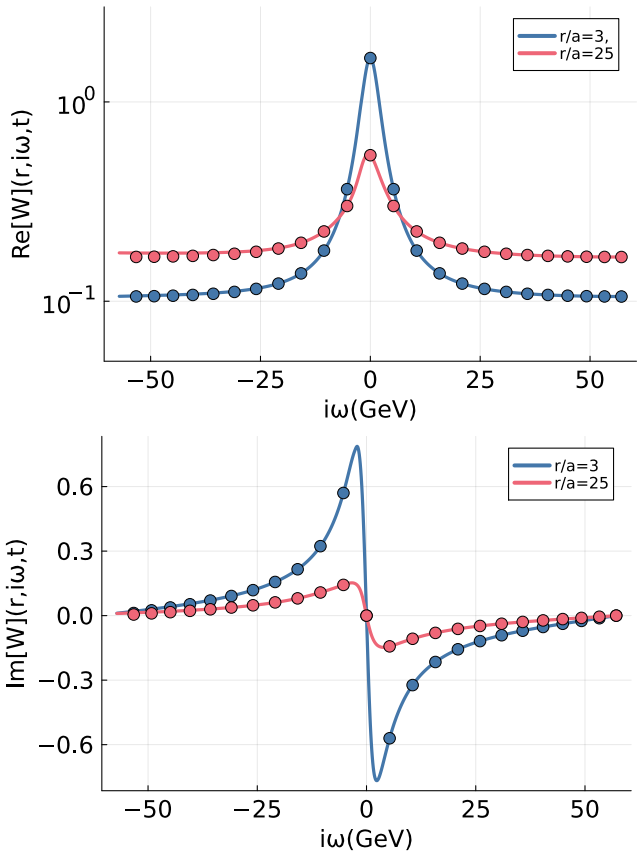

Figure 2.9: Matsubara frequency Wilson line correlators at two different separation distances for the $N_\tau = 24$ ($T = 3.11T_c$) anisotropic lattices. The top part shows the real part and the bottom part shows the imaginary parts. The dots show the Fourier transformed lattice data and the lines show the interpolated function.

Wilson line correlator along improved Matsubara frequecies (filled symbols) compared to the rational interpolation via eq. (2.15) (solid lines).

One can use eq. (2.15) to carry out an analytic continuation $\rho_r(\omega, T) = -\frac{1}{\pi}\mathrm{Im}[C_{N_\tau}(r, \omega, T)]$ and subsequently fit the lowest lying structure via eq. (1.33). Alternatively one can inspect the poles of the rational func-

tion eq. (2.15) directly and read off the dominant peak structure, as it belongs to the pole that is located most closely to the real frequency axis. If a well separated and pronounced pole emerges, its real- and imaginary part correspond to the real- and imaginary part of the potential. Having checked that the results obtained from both options agree within uncertainties, we choose to inspect poles, as it is computationally cheap.

In contrast to Bayesian spectral reconstruction, the result of the Padé method does not necessarily reproduce the Euclidean input data [50], i.e. it is known to violate the spectral decomposition. On the other hand, as we show below, it is able to reproduce relevant structures of the HTL spectral functions, in particular the position of the dominant peak. Since no regularization is present in the Padé interpolation formula, one also interpolates the error on the input data, making the reconstruction susceptible to statistical uncertainties. We therefore benchmark the reconstruction here only with $\Delta D/D = 10^{-3}$, which corresponds to the uncertainty level present in our lattice data.

As shown in the top panel of fig. 2.10, the Padé approach when applied to discrete HTL Wilson line data is able to locate the dominant peak structure and place the reconstructed peak accurately. However the peaks are too sharp, indicating that the the true width is underestimated. Note that the Padé reconstruction fails to describe the falloff of the spectral function both at frequencies below and above the peak in an accurate fashion. As expected, this entails that the resulting ρ, reinserted into the spectral decomposition does not reproduce the Euclidean input data.

In case of the Wilson loop, the performance of the Padé is more limited. With the available $N_\tau = 24$ datapoints at $\Delta D/D = 10^{-3}$, it manages to identify the peak up to intermediate distances $r < 0.327$fm after which no discernible structure (nor an individual pole close to the real frequency) can be found.

Turning to a quantitative assessment, we plot in the top panel of fig. 2.11

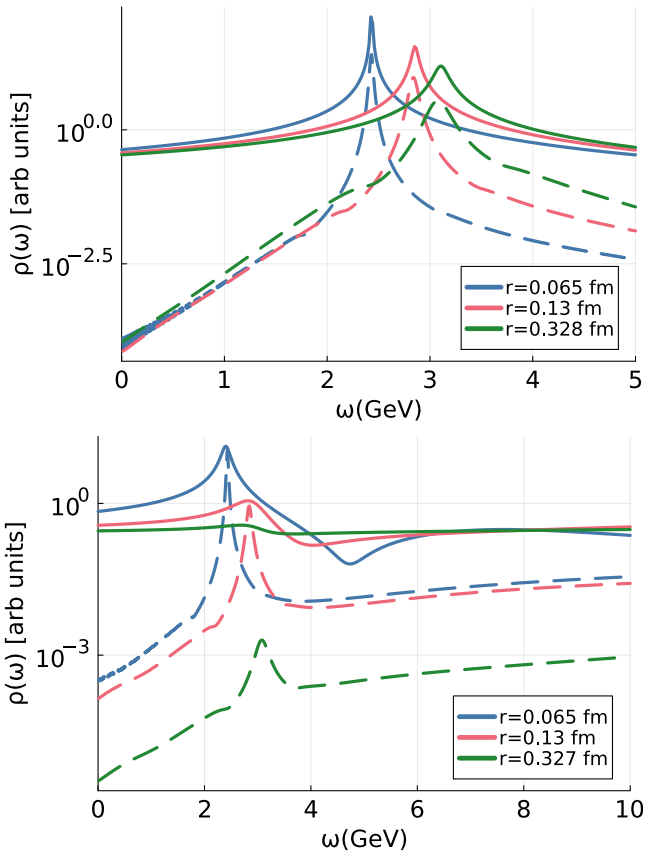

Figure 2.10: One realisation of Padé interpolation reconstructed (solid line) and semi-analytical (dashed line) spectral functions of the (top) Coulomb-gauge Wilson line correlator $\rho_{||}$ and (bottom) Wilson loop $\rho_{\square}$ in HTL perturbation based on $N_\tau = 24$ datapoints with $\Delta D/D = 10^{-3}$. The three curves each denote spectra at different spatial separation distances.

the real- and imaginary part of the static potential extracted from discrete HTL $W_{||}$ along $N_\tau = 24$ with $\Delta D/D = 10^{-3}$. Even though the reconstructed spectral function does not reproduce the input data, we find that a robust estimation of the position of the dominant pole, i.e. of $\mathrm{Re}[V]$ is possible with realistic data, up to large distances of $r = 1$fm. As expected from visual inspection of the reconstructed ρ the imaginary

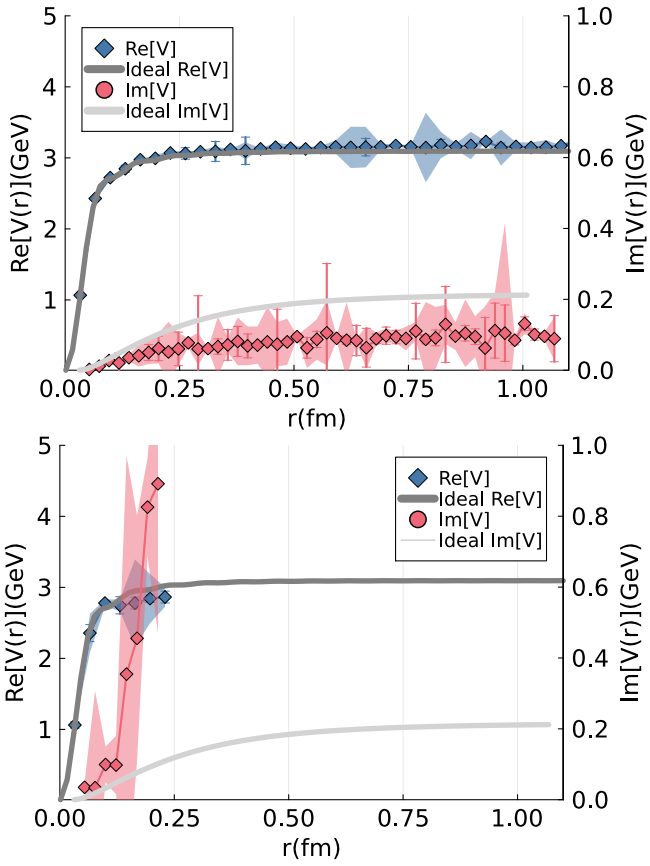

Figure 2.11: One realisation of Padé reconstructed (colored symbols) and analytic (solid line) values for the real- and imaginary part of the complex static quark potential from the (top) Coulomb-gauge Wilson line correlator $V_{||}(r)$ and (bottom) Wilson loop $V_{\square}(r)$ in HTL perturbation based on $N_\tau = 24$ datapoints with $\Delta D/D = 10^{-3}$.

part is systematically underestimated by around a factor of two.

In case of the more challenging Wilson loop data $W_{\square}$, the Padé manages to locate the dominant peak up to $r \approx 0.225$fm. Within this region, its position is correctly reproduced within the statistical uncertainties, which are larger than for $W_{||}$. The imaginary part is overestimated but suffers from strong variance even with the favorable $\Delta D/D = 10^{-3}$,

a testament for the missing regularization of such a direct projection approach.

2.3 Extraction of potential using HTL inspired fits

In this approach (see [43] and [44] for more details), one constructs a set of observables, which, by taking inspiration from HTL perturbation theory, are designed to reveal more clearly the physics of the real- and imaginary part of the potential, as is possible from effective masses alone, which were designed for the study of a purely real potential at $T = 0$.

The basic idea is to consider an expansion of the correlator around $\tau = \beta/2$, instead of the $\tau = 0$ expansion underlying m_{eff}. This is achieved by combining the correlator into an antisymmetric and a symmetric quantity

$$A(\tau) = \log\left[\sqrt{\frac{W(\tau, r)}{W(\beta - \tau, r)}}\right] \tag{2.18}$$

$$P(\tau) = \log\left[\sqrt{W(\tau, r)W(\beta - \tau, r)}\right]. \tag{2.19}$$

In leading order HTL perturbation theory, the quantity $A^{\text{HTL}}(\tau) = (\beta/2 - \tau)\text{Re}[V]$ is directly related to the real-part of the potential, while in case that the spectral peak is shaped as a Gaussian, one would obtain $A^{\text{Gaussian}}(\tau) = (\beta/2 - \tau)(\text{Re}[V] + \text{Im}^2[V])$, where both $\text{Re}[V]$ and $\text{Im}[V]$ contribute to the value of A. In any case, a behavior proportional to $(\beta/2 - \tau)$ is indicative of the presence of a dominant peak structure. It is interesting to note that a exponentially cut-off skewed Lorentzian and the Gaussian both lead to an exactly linear behavior in this quantity.

The symmetric component $P(\tau)$ in HTL perturbation theory can be shown to encode both the physics of the imaginary part of the potential,

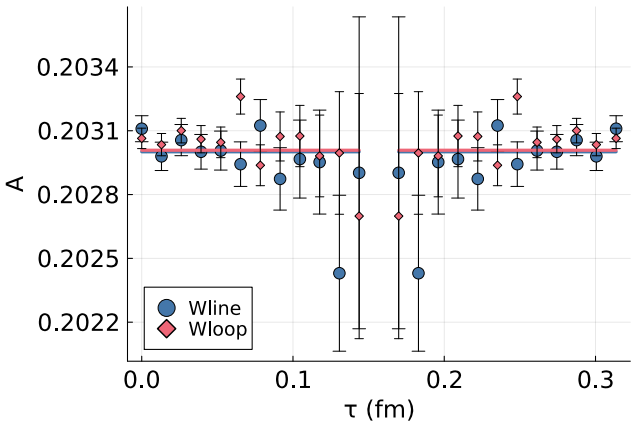

Figure 2.12: Comparison of the quantity A from HTL Coulomb-gauge Wilson lines (blue) and Wilson loops (red) for $N_\tau = 24$ and $\Delta D/D = 10^{-3}$ at a separation distance of $r = 0.0329$ fm. The HTL-inspired fit with $(\beta/2 - \tau)$ is shown as solid line.

as well as non-potential effects. Its derivative to first order gives

$$\frac{d}{d\tau}P^{\mathrm{HTL}}(\tau) = \frac{1}{\pi}\mathrm{Im}[V](r)\log\Big[\frac{\tau}{\beta-\tau}\Big] + \dots \tag{2.20}$$

where the symbols ... indicates a series of terms that includes non-potential effects.

One of the benefits of the way these observables are constructed is that they appear to lessen the influence of the UV continuum and are dominated by the low-lying peak structures. Let us plot the quantity A for both the HTL Coulomb-gauge Wilson line (red) and Wilson loops (green) in fig. 2.12. Note that while the effective masses for the Wilson loop in fig. 2.4 show a significantly different slope around $\tau = \beta/2$, which overshadows the contribution from the potential peak visible in the Wilson line effective masses, here the quantity A shows very similar slopes and only close to the fringes of the imaginary time interval exhibits curvature.

Benchmarking the extraction of the imaginary part from the derivative of P in HTL with realistic data turns out to be more difficult. Since

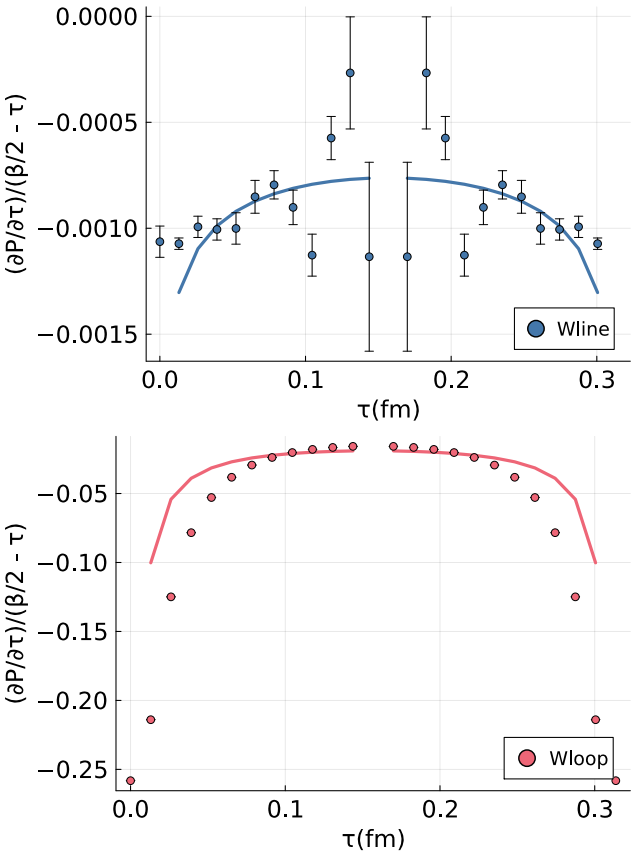

Figure 2.13: Comparison of the quantity $dP/d\tau$ from HTL Coulomb-gauge Wilson lines (blue, top) and Wilson loops (red, bottom) for $N_\tau = 24$ and $\Delta D/D = 10^{-3}$ at a separation distance of $r = 0.329$ fm. The HTL-inspired fit with $\cot[\pi\tau/(\beta)]$ is shown as solid line.

in HTL the imaginary part is relatively small, the signal to noise for $\Delta D/D = 10^{-3}$ is bad. As shown in the next section, when we investigate actual lattice data, we find a much larger curvature of $dP/d\tau$, so that even with a $\Delta D/D = 10^{-3}$ an estimate for the imaginary part can be obtained. For demonstration purposes we thus show in fig. 2.13 the values from HTL for $\Delta D/D = 10^{-3}$, together with the lowest order HTL-inspired fit around $\tau = \beta/2$ proportional to $\log[\tau/(\beta - \tau)]$. We

can see that the fit Ansatz now is only compatible with the data around $\tau = \beta/2$. As fig. 2.13 suggests, we would need to consider higher order non-potential terms to fit the data to a larger τ range. To fit the data over a considerably larger τ range we instead use a fit form:

$$W(\tau, r) = e^{-\mathrm{Re[V](r)}(\tau-\beta/2)-\frac{\beta}{\pi}\mathrm{Im[V](r)}\log\sin\frac{\pi\tau}{\beta}+\mathrm{G_{NP}}(\tau,\mathrm{r},\beta)} W(\beta, r) \quad (2.21)$$

With the higher order terms representing non-potential effects being,

$$G_{NP}(\tau, r, \beta) = \sum_l c_l \int_{\beta/2}^{\tau} \tilde{G}_l(\tau) \quad (2.22)$$

$$\tilde{G}_l(\tau) = \frac{(2l!)}{\beta^{2l+1}}\Big(\zeta(2l+1, 1-\frac{\tau}{\beta}) - (\zeta(2l+1, \frac{\tau}{\beta})\Big)$$

Here ζ is the generalized zeta function $\zeta(s, x) = \sum_{n=1}^{\infty} \frac{1}{(x+n)^s}$. Instead of fitting to the correlator we fit to effective masses (as suggested in [49]) which is done by taking the log of derivative on both sides.

$$\begin{aligned} m_{\mathrm{eff}}(r,\tau)a &= \log\left(\frac{W(r, n_\tau, N_\tau)}{W(r, n_\tau+1, N_\tau)}\right) \\ &= \mathrm{Re[V]}(r,T)\, a - \frac{\mathrm{Im[V]}(r,T)aN_\tau}{\pi}\, \log\left[\frac{\sin(\pi n_\tau/N_\tau)}{\sin(\pi(n_\tau+1)/N_\tau)}\right] + \sum_l c_l \tilde{G}_l(\tau) \end{aligned} \quad (2.23)$$

In our fits we found that the first two terms with parameters $c_1$and c_2 were sufficient to fit the data to a large τ region (see section 4.4) with the exceptions being a few small τ and a few points around $\tau = \beta$ (1-3 depending on the separation distance). We will discuss the quality of the fits on lattice data in section 4.2. Using the fit form as described in eq. (2.23), we extract $\mathrm{Re}[V]$ and $\mathrm{Im}[V]$ from the mock data with results given in fig. 2.14.

We find that for the Wilson line correlators we are able to recover both the correct real and imaginary parts using data with errors $\Delta D/D = 10^{-3}$ up to a high separation distance of 1 fm. For the Wilson loop data we were able to extract the correct real part, but however we were only able to recover the correct imaginary part up to $r \sim 0.15$fm.

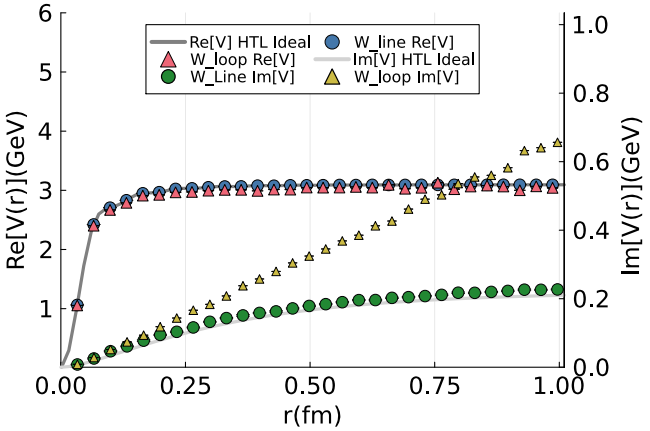

Figure 2.14: HTL-inspired fit reconstructed (colored symbols) and analytic (solid line) values for the real- and imaginary part of the complex static quark potential from the Coulomb-gauge Wilson line correlator $V_{||}(r)$ and Wilson loop $V(r)$ in HTL perturbation based on $N_\tau = 24$ datapoints with $\Delta D/D = 10^{-3}$.

2.4 Zero temperature subtraction and spectral function model fits

In this section we consider a different approach which allows for different ansatz for the spectral functions besides from the skewed lorentzian that we derived in eq. (1.33); We observed that the high frequency tails in the spectral function play an important role in establishing a time independent potential. To isolate the high frequency tails of the spectral functions, the authors of [51; 45] proposed to split the spectral function as

$$\rho(\omega, T) = \rho(\omega, T)^{med} + \rho(\omega)^{high}. \tag{2.24}$$

Here the $\rho(\omega, T)^{med}$ contains only the spectral structures of interest and the $\rho(\omega)^{high}$ describes the UV behaviour of the spectral functions which is assumed to be temperature independent. At zero temperature $\rho(\omega, T)^{med}$ is a single delta function describing the ground state of static $Q\bar{Q}$ pair for our choice of the static meson operator. If we now

assume that the higher peaks are well separated from the ground state we can isolate it and subtract it from $W_{\square}(r, \tau, T = 0)$. This can give us an estimate for the high frequency part of the spectral function. Once evaluated at zero temperature it can be used to subtract off an estimate for the high omega contribution at $T > 0$ at the same value of β. The absence of high ω structures in the spectral functions would allow for a different ansatz i.e Gaussian ansatz for the spectral function. We also expect that the removal of the high frequency parts in the spectral function would make it easier for model independent approaches of BR and Padé interpolation in reconstructing the spectral function to be more reliable as we are getting rid of information that is not relevant to the position of the dominant peak and the width.

This approach relies on the assumptions that the high frequency part of the spectral function is only a lattice artifact and is independent of temperature. We cannot test this approach directly with HTL perturbation theory, as no zero temperature subtraction can be carried out. In subsequent chapters we will try to establish whether this assumption is indeed satisfied by the lattice data and present some other model (gaussian) ansatz for the spectral function which otherwise would not be valid for a time independent potential.

2.5 Mock test summary and outlook

We find from extensive testing, based on non-trivial mock data that for the realistic scenario of $N_\tau = 24$ and $\Delta D/D = 10^{-2}$ the approaches based on Bayesian inference and Padé approximation are able to extract reliably the position of the dominant peak encoded in the HTL spectrum. The width of the peak, when extracted from Coulomb-gauge Wilson lines is systematically underestimated, while from Wilson loops tends to be overestimated. A reliable reconstruction of the position of the peak thus would require that the uncertainties in our data $\Delta D/D = 10^{-2}$.

The HTL inspired method we find is able to distinguish between be-

tween the HTL and single dominant Gaussian peak hypothesis. Under the (in this case correct) assumption that the data encodes an HTL-like spectral function we can reliably extract both $\mathrm{Re}[V]$ and $\mathrm{Im}[V]$ using either Wilson lines or loops. We present the extraction of spectral functions and potential using these methods in chapter 3 and chapter 4.

We would like to mention here that there are other methods for spectral reconstruction that have been applied in the literature with varying levels of success.

The first being extracting spectral functions from Gaussian process regression (GPR). Gaussian processes are based on the fact that any function can be interpolated using multivariate Gaussian distribution. In recent years, this idea was shown to be applicable in solving inverse problems [52]. The idea was then applied in the QCD settings by the authors of [53] to reconstruct ghost and gluon spectral functions. This method looks promising in extracting spectral functions of the Wilson line but suffers from two major issues. The first being that one has to find the right kernel function for the gaussian process using some mock data. However, no such mock data is available in a fully non-perturbative setting where both the data and the spectral function are known. Nevertheless, one can still use the HTL mock data as a training set to optimize for the right kernel. The second difficulty is that GPR reconstructed spectral functions suffer from oscillatory artifacts at small frequencies. The authors of [53] got around this problem by fixing the low frequency behaviour of the spectral functions using results obtained from analytically solving the momentum integrals of Dyson-Schwinger equations. It is yet unclear about how to get around this issue for Wilson line spectral functions, but one could possibly try to get some insights from function renormalization group methods and Dyson-Schwinger equations [54; 55; 56].

Another method that was recently developed which directly exploits the analytic structure of Green's functions known as Nevanlinna Analytical Continuation [57]. This method takes inspiration from the Padé

interpolation and also attempts to interpolate the data in Matsubara frequency space rather than fit it. It attempts to resolve some of the issues associated with the Padé spectral functions i.e the Padé obtained spectral functions do not recover the Euclidean correlator data and, they also tend to violate positivity. Instead of a generic continued fraction one instead considers a class of Nevalinna functions which, by construction are always positive definite. This method has been used to reconstruct spectral functions in condensed matter systems like Orbital-resolved realistic band structure of $SrVO_3$ where the spectral functions are fermionic in nature. Applying this approach to reconstruct Wilson line functions would require a re-derivation of the interpolation formula for bosonic degrees of freedom and would be an interesting project for future works.

In addition to these methods, like Tikhonov regularisation [48], neural network reconstruction [58] and Backus-Gilbert method [59; 60] have also been used in the literature. However, these methods have not been explored deeply during the course of the PhD and are thus orthogonal to this thesis.

3 Study on 2+1 Flavour HISQ lattices

[1]The static in-medium potential has been studied non-perturbatively on the lattice via spectral function reconstruction and model spectral function fits. Based on the Bayesian BR method [41] for spectral reconstruction the static potential has so far been investigated in quenched QCD [36; 37] and in full QCD simulations based on the legacy asqtad action [61; 62]. Recently HTL motivated decomposition of APE smeared Wilson loop in symmetric and anti-symmetric parts has also been used to extract the thermal potential in the quenched approximation [43]. These studies concluded that the real-part of the potential eventually becomes screened in the deconfined phase and have identified hints for the existence of an imaginary part once one simulates above the crossover temperature. Concurrently the potential has been extracted by fitting modified HTL spectral functions to Euclidean correlators in [63] and deploying a skewed or non-skewed Lorentzian fit in [64]. In both cases values for the real-part were obtained that are significantly larger than those extracted via the direct spectral function reconstruction lying closer to the $T = 0$ results.

In this study we set out to investigate the interactions of static quark-antiquark pairs at $T > 0$ using realistic state-of-the-art lattice QCD calculations. Wilson loops and correlators of Wilson lines in Coulomb gauge at non-zero temperature in (2+1) flavor QCD with physical strange quark mass using gauge configurations generated by HotQCD and TUMQCD collaborations with Lüscher-Weisz gauge action as described by eq. (1.21) and highly improved staggered quark action [65; 66; 67; 68; 5; 69; 70]. $N_\sigma^3 \times N_\tau$ lattices with $N_\tau = 10$, 12 and 16 lattices were used to compensate for lattice spacing effects and $N_\sigma/N_\tau = 4$ to make sure that the aspect ratio was large enough to make sure that finite volume effects do not play a role. The light (u and d)

[1]The contents of this chapter have been published in [49]. The author of this thesis has contributed towards the Bayesian and Padé extraction of the potential along with the concluding plots which compare all the different methods.

quark mass was set to $m_s/20$, which in the continuum limit corresponds to pion mass of 161 MeV. At high temperatures, $T > 300$ MeV we also performed calculations with light quark mass equal to $m_s/5$, as quark mass effects are expected to be small in this region. The lattice spacing has been fixed using the r_1 scale defined in terms of the static $Q\bar{Q}$ energy at zero temperature $V(r)$

$$r^2 \frac{dV}{dr}\bigg|_{r=r_1} = 1. \tag{3.1}$$

The values of r_1/a as well as the zero temperature Wilson loops and Wilson line correlators for (2+1)-flavor HISQ configurations have been determined in Refs. [65; 67; 5]. Using the parametrization given in Ref. [5] we obtain a/r_1 and the value $r_1 = 0.3106$ fm [71]. Thus allows us to cover a large temperature range from 120 MeV to about 2 GeV. The parameters of the simulations are show in tables 3.1 to 3.4.

3.1 Cumulant analysis of the correlation function

To understand the main features of our lattice results and to what extent these can constrain the spectral function of a static meson it is useful to consider the n-th cumulants of the correlation functions defined as

$$m_1(r,\tau,T) = -\partial_\tau \ln W(r,\tau,T), \tag{3.2}$$

$$m_n = \partial_\tau m_{n-1}(r,\tau,T), n > 1. \tag{3.3}$$

The first cumulant is just the effective mass which for lattice spacing a is given by

$$m_1(r,\tau,T) = m_{\text{eff}}(r,\tau,T) = \frac{1}{a} \ln \frac{W(r,\tau,T)}{W(r,\tau+a,T)}. \tag{3.4}$$

$m_l = m_s/20$:						
β	a (fm)	N_σ, N_τ	am_s	$m_\pi L$	#TUs	Ref.
6.740	0.109	48^4	0.0476	4.2	1350	[65]
6.800	0.103	32^4	0.0448	2.7	5650	[65]
6.880	0.095	48^4	0.0412	3.7	1400	[65]
6.950	0.089	32^4	0.0386	2.3	10830	[65]
7.030	0.083	48^4	0.0356	3.2	1355	[65]
7.150	0.074	$64^3 \times 48$	0.0320	2.9	1458	[65]
7.280	0.066	$64^3 \times 48$	0.0284	2.5	1734	[65]
7.373	0.060	$64^3 \times 48$	0.0250	2.3	4623	[67]
7.596	0.049	64^4	0.0202	2.6	4757	[67]
7.825	0.040	64^4	0.0164	2.0	4768	[67]
$m_l = m_s/5$:						
β	a [fm]	N_σ, N_τ	am_s	$m_\pi L$	#TUs	Ref.
8.000	0.035	64^4	0.01299	3.6	4616	[5]
8.200	0.029	64^4	0.01071	3.1	4616	[5]
8.400	0.025	64^4	0.00887	2.6	4616	[5]

Table 3.1: Parameters of the calculations on zero temperature lattices for $m_l = m_s/20$ (upper part) and $m_l = m_s/5$ (lower part).

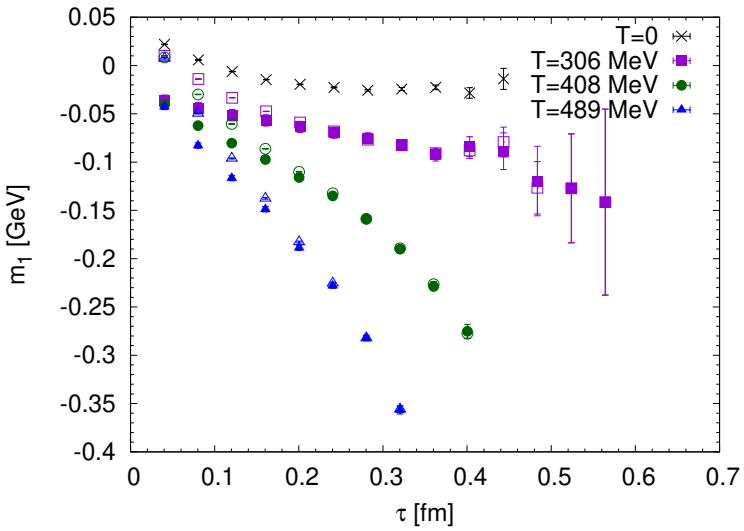

Figure 3.1: The first cumulant calculated at $r = 0.24$fm for $\beta = 7.825$ and $N_\tau = 64,\ 16,\ 12$ and 10, corresponding to $T \simeq 0,\ 306,\ 408$ and 489 MeV, respectively. The filled symbols correspond to the subtracted correlator, while the open symbols to unsubtracted correlator, see text.

$m_l = m_s/20$:			
β	am_s	T (MeV)	#TUs
7.825	0.00164	306	67960
8.570	0.008376	577	10400
8.710	0.007394	650	10190
8.850	0.006528	731	4480
9.060	0.004834	872	41870
9.230	0.004148	1005	3610
9.360	0.003691	1121	3530
9.490	0.003285	1250	6790
9.670	0.002798	1454	42060
$m_l = m_s/5$:			
β	am_s	T (MeV)	#TUs
8.000	0.001299	356	11460
8.200	0.001071	422	10660
8.400	0.000887	500	64370

Table 3.2: Parameters of the $64^3 \times 16$ calculations for the two different light quark masses. The lower part of the table corresponds to $m_l = m_s/5$, while the upper part corresponds to $m_l = m_s/20$.

In Fig. 3.1 we show the first cumulant from Wilson line correlators at $r = 0.24$ fm for $\beta = 7.825$ and $N_\tau = 16, 12$ and 10 corresponding to temperatures for $T = 306$, 408 and $T = 489$ MeV, respectively and compared to the zero temperature first cumulant. At $T = 0$ the first cumulant approaches a plateau for $\tau > 0.2$ fm. On the other hand the non-zero temperature cumulant decreases monotonically. At small τ the difference between the zero temperature and the unsubtracted finite temperature first cumulant is very small and increases monotonically as τ increases. The slope of the first cumulant increases with increasing the temperature. This means that the in-medium modifications of the spectral function are larger at larger temperature, as expected.

We also observe that the small τ and in turn high ω behaviour in the spectral function of the unsubtracted correlator is largely temperature independent. Thus, we followed the footsteps outlined in section

$m_l = m_s/20$			
β	am_s	T (MeV)	#TUs
6.515	0.0604	122	32500
6.608	0.0542	133	19990
6.664	0.0514	141	45120
6.700	0.0496	146	15900
6.740	0.0476	151	29410
6.770	0.0460	156	15530
6.800	0.0448	160	36060
6.840	0.0430	166	17370
6.880	0.0412	173	46350
6.950	0.0386	185	50550
7.030	0.0378	199	65940
7.100	0.0332	213	9640
7.150	0.0320	223	9600
7.200	0.0296	233	4010
7.280	0.0284	251	58210
7.373	0.0250	273	85120
7.596	0.0202	334	98010
7.650	0.0202	350	3230
7.825	0.0164	408	134600
8.000	0.0140	474	3110
8.200	0.01167	562	30090
8.400	0.00975	667	29190
8.570	0.008376	770	6320
8.710	0.007394	866	6490
8.850	0.006528	974	6340
9.060	0.004834	1162	7430
9.230	0.004148	1340	7280
9.360	0.003691	1495	7910
9.490	0.003285	1667	9780
9.670	0.002798	1938	7650
$m_l = m_s/5$			
β	am_s	T (MeV)	#TUs
8.000	0.01299	474	71670
8.200	0.01071	563	71390
8.400	0.00887	667	71170

Table 3.3: Parameters of the calculations on $48^3 \times 12$ lattices for $m_l = m_s/20$ (upper part) and $m_l = m_s/5$ (lower part).

$m_l = m_s/20$			
β	am_s	T (MeV)	#TUs
6.285	0.0790	116	9260
6.341	0.0740	123	39190
6.423	0.0670	133	10360
6.488	0.0620	142	102690
6.515	0.0604	146	107530
6.575	0.0564	155	106020
6.608	0.0542	160	112890
6.664	0.0514	169	155440
6.740	0.0476	181	200250
6.800	0.0448	192	279830
6.880	0.0412	208	341490
6.950	0.0386	222	243480
7.030	0.0378	239	137730
7.150	0.0320	267	145440
7.280	0.0284	301	105990
7.373	0.0250	328	50840
7.596	0.0202	400	51710
7.825	0.0164	489	54000
8.000	0.0140	569	6780
8.200	0.01167	675	27500
8.400	0.00975	800	7540
8.570	0.008376	924	3000
8.710	0.007394	1039	15320
8.850	0.006528	1169	7690
9.060	0.004834	1395	15490
9.230	0.004148	1608	7630
9.360	0.003691	1794	15800
9.490	0.003285	2000	7990
9.670	0.002798	2326	15760
$m_l = m_s/5$			
β	am_s	T (MeV)	#TUs
8.000	0.01299	569	82770
8.200	0.01071	675	72180
8.400	0.00887	800	72770

Table 3.4: Parameters of the calculations on $40^3 \times 10$ lattices for $m_l = m_s/20$ (upper part) and $m_l = m_s/5$ (lower part).

section 2.4 and obtain an estimate for the subtracted correlator. We calculated the first cumulant from the subtracted correlator and the results are also shown in Fig. 3.1. At large τ the subtraction has no effect, however, at small τ the subtracted first cumulant at $T > 0$ shows a weaker τ-dependence. At the same time it shows visible temperature dependence already for small τ's. At these small τ values we see an approximately linear τ-dependence of m_1 at non-zero temperature with a slope similar to the $\tau \sim 1/(2T)$ region. For the lowest temperature, $T = 306$ MeV the decrease in the first cumulants is approximately linear in τ around $\tau \sim 1/(2T)$, while for the higher temperatures this linear trend is only seen for smaller τ, corresponding to the reduction in $1/(2T)$.

In order to better understand our numerical results on the first cumulants and see to what extent these can constrain the spectral function of a static meson it is helpful to calculate higher cumulants of the correlator. In the following we consider the cumulants of the subtracted correlator as we are interested in exploring the τ-dependence caused by thermal broadening of the dominant peak. To evaluate higher cumulants we performed fits of the first cumulants of the subtracted correlator using fourth order polynomials, and estimated the higher cumulants by taking the derivatives of the resulting polynomial. The results for the second cumulants for three distances, $rT = 1/4,\ 1/2$ and 1 at several temperatures are shown in Fig. 3.2 for $N_\tau = 12$. The errors on the cumulants have been estimated using the jackknife procedure. Since the second cumulant is negative, and the square root of the negative second cumulant may be related to the width, as discussed later, in the figure we show $\sqrt{-m_2}$ in temperature units. We see that the errors on the second cumulants increase with decreasing temperatures. At short distances, the second cumulant is approximately constant for small τ and then starts to increase rapidly with increasing τ. For $rT = 1$ the almost constant behavior of m_2 is only seen for the highest two temperatures. The results for $T < 251$ MeV are not shown as these have much larger errors. However, within these large errors the second cumulant is compatible with a constant at these temperatures.

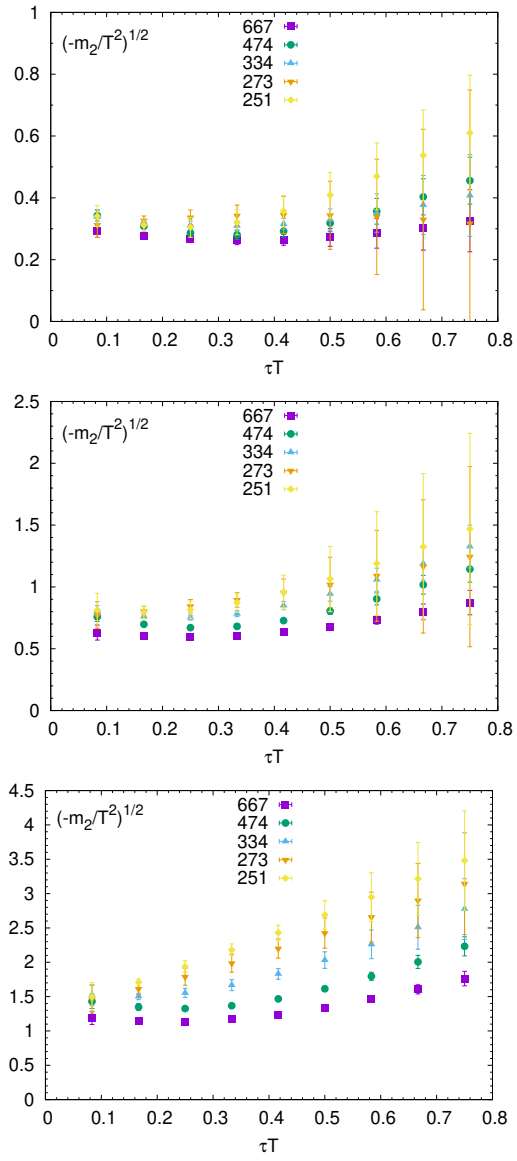

Figure 3.2: The second cumulants m_2, obtained from a fourth order polynomial fit to the first culumant m_1, of the subtracted static meson correlator on $N_\tau = 12$ lattices for $rT = 1/4$ (left), $rT = 1/2$ (middle) and $rT = 1$ (right) for several temperatures. The different symbols correspond to different temperatures given in MeV.

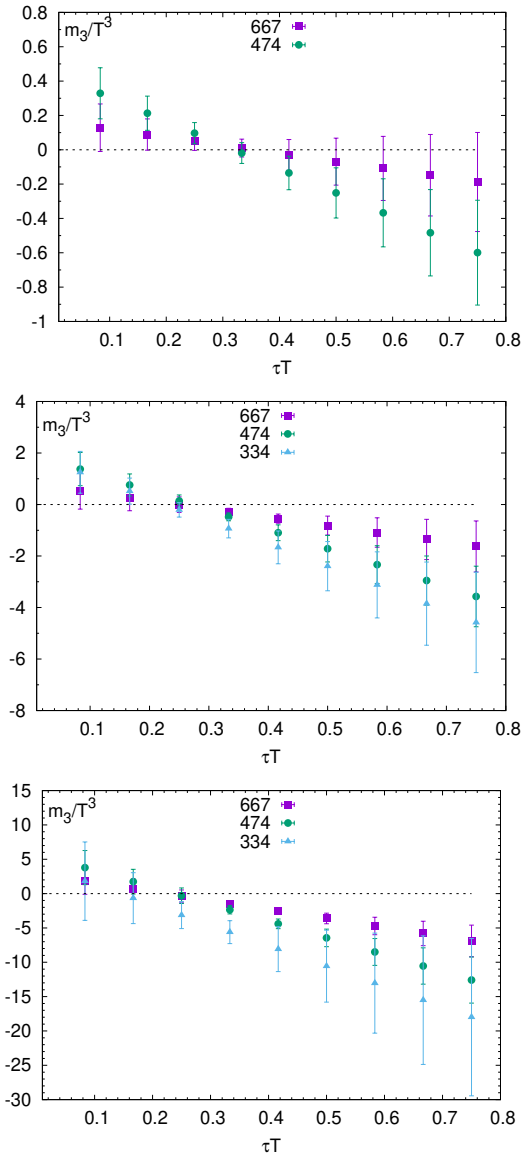

Figure 3.3: The third cumulants m_3, obtained from a fourth order polynomial fit to the first culumant m_1, of the subtracted static meson correlator on $N_\tau = 12$ lattices for $rT = 1/4$ (left), $rT = 1/2$ (middle) and $rT = 1$ (right) for several temperatures. The different symbols correspond to different temperatures given in MeV.

In Fig. 3.3 we show the third cumulant of the Wilson line correlator, obtained from a fourth order polynomial fit to the first culumant m_1, as function of τT in temperature units. The results are shown for three representative distances, $rT = 1/4$, $rT = 1/2$ and $rT = 1$. We only show our findings for the third cumulant for $T \geq 334$ MeV as at lower temperatures the errors are too large to extract meaningful information from them. Furthermore, for $rT = 1/4$ the errors are already very large for $T = 334$ MeV. The absolute value of the third cumulant increases rapidly with increasing rT and decreases with increasing temperature. These features can be already deduced by looking at the result for the second cumulant. For $\tau T > 0.35$ the third cumulant is negative, while for $\tau < 0.3$ it is positive but small given the errors. The small positive third cumulant at small τ is equivalent to having a nearly constant second cumulant.

From Fig. 3.3 it is clear that estimating the fourth and higher order cumulants from the present lattice results is very challenging. This will be important when considering parametrization of the spectral function of a static meson, as the data can only constrain such a limited amount of parameters. Hence any such parametrization should not contain more than three or four parameters.

3.2 Determination of the ground state peak from spectral function model fits

In order to constrain the spectral function $\rho_r(\omega, T)$ from limited data on Euclidean time correlation functions we need to assume some functional form for it. As for the analysis of the cumulants we assume that the spectral function can be written $\rho_r(\omega, T) = \rho_r^{tail}(\omega, T) + \rho_r^{med}(\omega, T) + \rho_r^{high}(\omega)$, with $\rho_r^{high}(\omega)$ assumed to be temperature independent high frequency part of the spectral function and $\rho_r^{med}(\omega, T)$ containing the dominant peak structure. Based on general grounds and EFT arguments it is natural to assume that $\rho_r^{med}(\omega, T)$ has a Lorentzian form. However, for a Lorentzian form the integral in Equation (1.35) will not converge at the lower integration limit. In the case of HTL spectral function

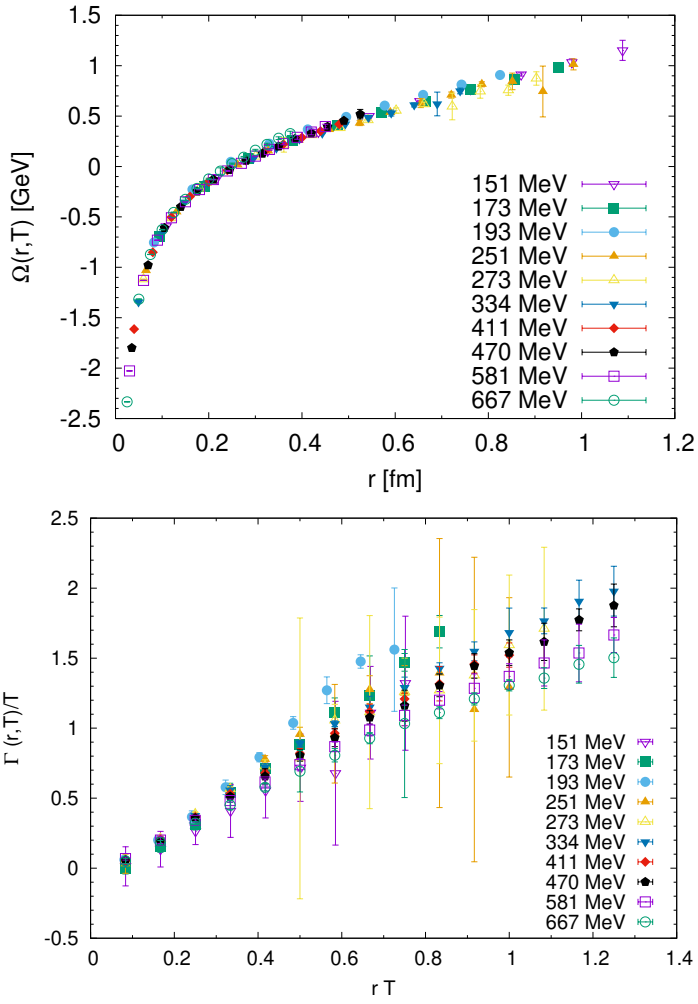

Figure 3.4: The peak position of the spectral function (left figure) and the width (right figure) as function of the separation r obtained from Gaussian fits of the $N_\tau = 12$ data.

we have seen that while around the peak the spectral function appears to be Lorentzian, different structures dominate the spectral function far away from the peak, in particular at very low frequency, see fig. 2.2. Thus in addition to the parametrization of the peak of the spectral function, we also need to parametrize the behavior of the spectral function at very low frequency, i.e. the low energy tail. This part of the spectral function will affect the correlation function at large values of τ. Unfortunately, we do not have a well motivated form for this part of the spectral function. Furthermore, for calculations in finite volume the spectral function is not a continuous function but a discrete sum of delta functions with an envelope function of certain shape. For small volumes as used in the present calculations there could be significant distortion of the envelope function, since the number of low lying energy levels and the corresponding number of δ peaks is quite limited. This is especially the case for the low ω tail as it extends over a large ω-range below the dominant peak position, including negative ω values.

The information we have on the different structures in the spectral function is also quite limited. At small τ values only the first two cumulants can be determined with the third cumulant being zero within the estimated errors. Therefore, at small τ the lattice data are only sensitive to the position and the effective width of the dominant peak, and a Gaussian form provides a simple parametrization for this that avoids convergence problem in eq. (1.35). At larger τ the correlation function is sensitive to the low energy tail, i.e. the region $\omega \ll \Omega(r,T)$. In the previous section we have seen that in this region also the third cumulant is non-zero, but cumulants beyond the third one cannot be constrained by our lattice data. While it would be tempting to parametrize the low ω tail of the spectral function by a series of delta functions avoiding any bias, in practice it is impossible to constrain all the corresponding parameters. We need to approximate this part of the spectral function by a single delta function

Thus a simple parametrization of the Wilson line correlator function

consistent with the above observations is the following:

$$W(r,\tau,T) = A_P(r,T)\exp\Big(-\Omega(r,T)\tau + \Gamma_G(r,T)^2\tau^2/2\Big) + A_{cut}(r,T)\exp(-\omega_{cut}(r,T)\tau), \tag{3.5}$$

with $A_{cut} \ll A_P$ and $\omega_{cut} \ll \Omega$ The first cumulant corresponding to this form will decrease linearly at small τ, while exhibiting a non-linear behavior for large τ as observed in our lattice results. We performed correlated fits of our lattice data using eq. (3.5) and determined the parameters A_P, Ω, Γ_G, A_{cut} and ω_{cut}. The fits describe the lattice data very well, with possible exception of the data at the smallest τ value. The details of these fits are shown in fig. 3.5.

The peak position, $\Omega(r,T)$ is shown in fig. 3.4 as function of the distance r for different temperatures. It shows no temperature dependence and agrees with the zero temperature static energy. The fact that Ω is close to the zero temperature static energy can be easily understood from fig. 3.1. The subtracted first cumulant at smallest τ is already close to the zero temperature plateau and shows and linear behavior at small τ. A linear extrapolation naturally gives the zero temperature static energy. The width of the dominant peak depends on the specific parametrization of the spectral function and the Gaussian form has no physical motivation. A parametrization independent definition of the effective width could be the width at the half maximum. For a Gaussian form this means $\Gamma = \Gamma_G\sqrt{2\ln 2}$. In fig. 3.4 we also show the effective width Γ as function of the distance, r at different temperatures. We see that Γ increases with increasing r. We also see that when plotted as function of rT the effective width in temperature units shows very little temperature dependence. This is expected at very high temperature, but not in the temperature range studied by us. For the other two fit parameters we find that $\omega_{cut} \ll \Omega$ and $A_{cut} \ll A_P$ in accordance with our expectations. The same parametrization of the spectral function has been used in the analysis of NRQCD bottomonium correlators at non-zero temperature [45; 51]. It has been observed that different bottomonium states have thermal width, but no significant mass shift has

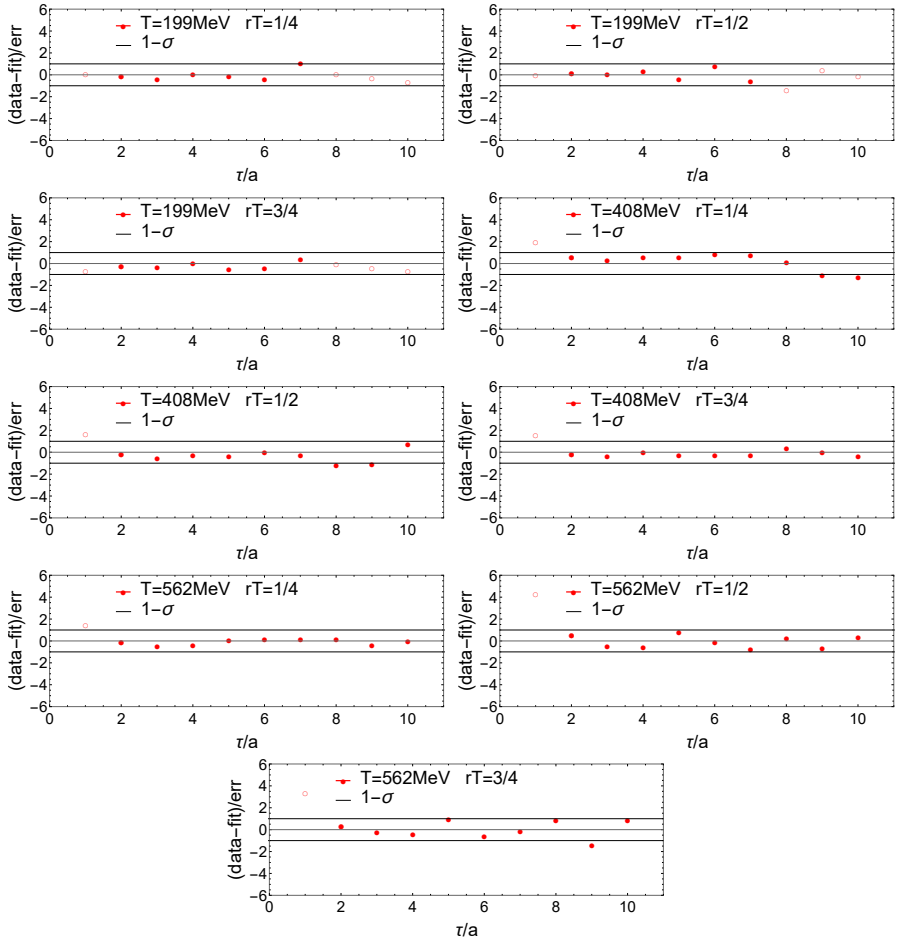

Figure 3.5: The difference between the Gaussian fit and the lattice data on the first cumulant for $N_\tau = 12$ as function of τ normalized by the statistical errors for $rT = 1/4$, $rT = 1/2$ and $rT = 3/4$. The open symbols correspond to the data points not included in the fit.

been observed. Furthermore, the thermal width turned out to be larger for higher lying bottomonium states that have larger size [45; 51]. Thus the thermal modification of static $Q\bar{Q}$ states and bottomonium is quite similar. Futhermore, the bottomonium Bethe-Salpeter amplitudes also do not show large temperature modifications [72]. Using this result a potential model analysis resulted in a potential that has a real part which is identical to the zero temperature static energy [73].

3.3 Determination of the ground state peak via the HTL-motivated method

In this section we follow the steps outlined in section 2.3 to extract the ground state peak. We focus on the narrow region around $\tau = 1/(2T)$ such that higher order terms in eq. (2.23) can be neglected and we can fit the lattice results on the first cumulant with the simple form

$$\begin{aligned} m_{\text{eff}}(r,\tau)a &= \log\left(\frac{W(r,n_\tau,N_\tau)}{W(r,n_\tau+1,N_\tau)}\right) \\ &= \text{Re}[\text{V}](r,T)\,a - \frac{\text{Im}[\text{V}](r,T)aN_\tau}{\pi}\,\log\left[\frac{\sin(\pi n_\tau/N_\tau)}{\sin(\pi(n_\tau+1)/N_\tau)}\right] \end{aligned} \quad (3.6)$$

We performed fits of our $N_\tau = 12$ lattice data for m_1 for $\tau/a = 5, 6, 7$ using Eq. (3.6) to determine $\Omega(r,T)$ and $\Gamma(r,T)$. The details of these fits can be found in fig. 3.6. A sample fit for both unsubtracted and subtracted data has been shown in Fig. 3.7. The ansatz also describes some data points outside the fitting range. The smaller τ and larger τ behavior are not expected to be described by the above Ansatz, as it only describes the dominant peak of the spectral function. In Fig. 3.8 we show $\Omega(r,T)$ and $\Gamma(r,T)$ from these fits as function of r at different temperatures. The peak position $\Omega(r,T)$ and width $\Gamma(r,T)$ for subtracted and unsubtracted correlators are very close to each other. This is expected because we only consider τ values around $1/(2T)$, where the contribution of the high ω part of the spectral function is small. The peak position, $\Omega(r,T)$ shows significant temperature dependence and differs from the zero temperature potential. The width

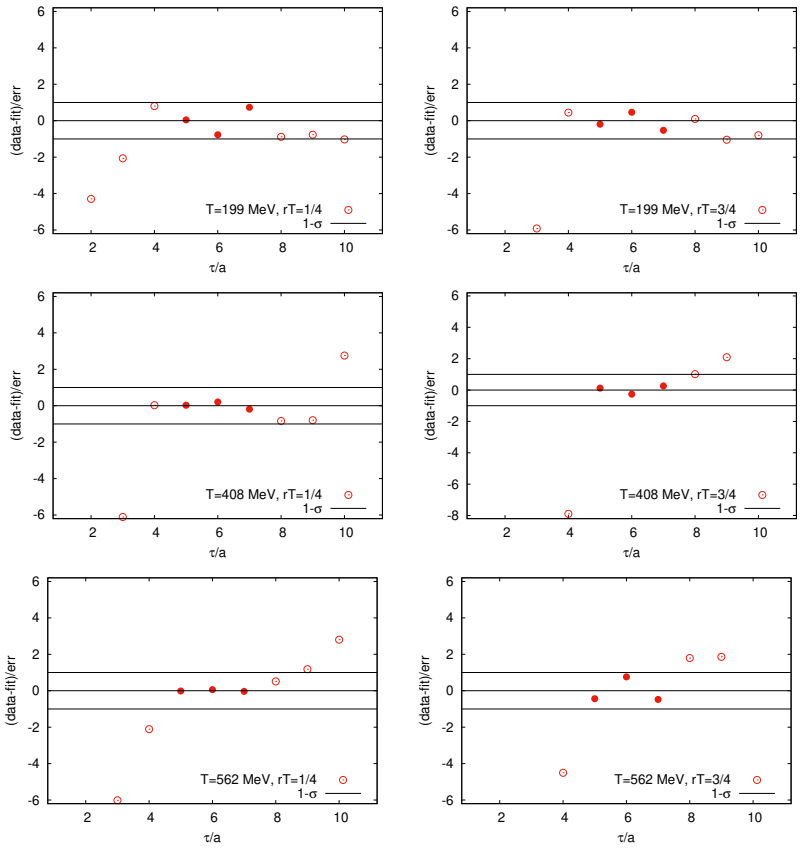

Figure 3.6: The difference between the Bala-Datta fit and the lattice data on the first cumulant for $N_\tau = 12$ as function of τ normalized by the statistical errors for $rT = 1/4$ and $rT = 3/4$. The open symbols correspond to the data points not included in the fit.

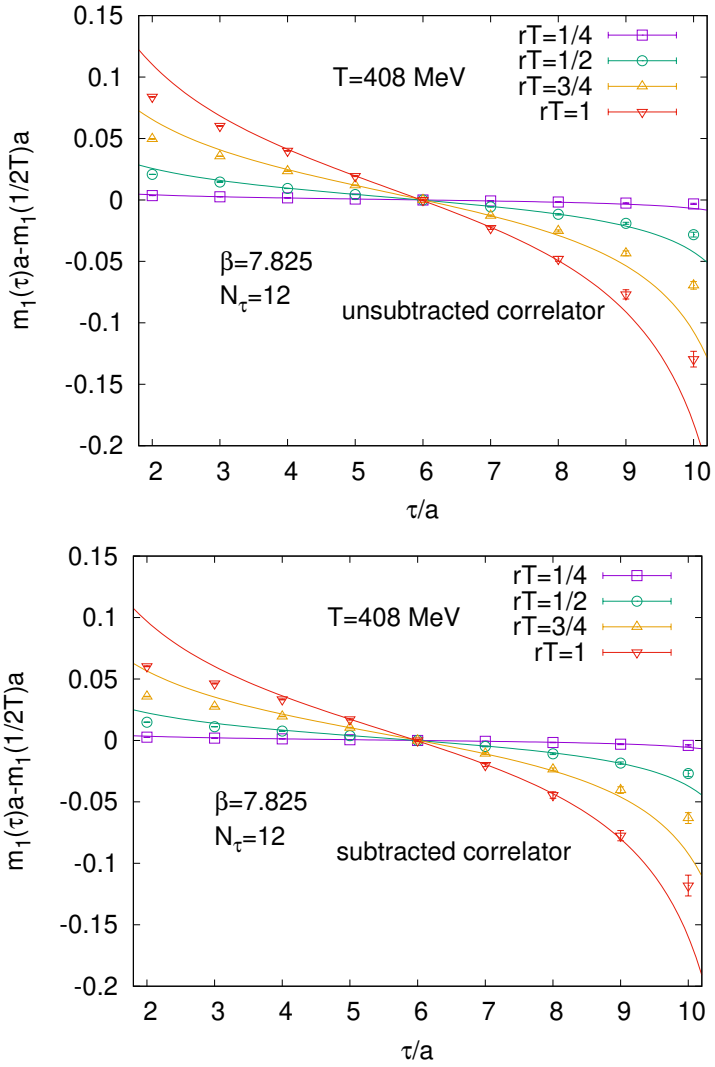

Figure 3.7: Sample fit of the lattice result (Top) unsubtracted correlator and (Bottom) subtracted correlator to Eq. (3.6), see text.

of the peak, $\Gamma(r,T)$ increases with increasing r. Furthermore, $\Gamma(r,T)$ does not scale with the temperature unlike in the case of Gaussian fits in the temperature range explored by us. We also find that in the temperature region studied by us $\Gamma(r,T)$ is larger than the HTL result.

Another widely studied quantity at finite temperature is the singlet free energy $F_S(r,T)$, see e.g. [69]. As mentioned above in leading-order HTL perturbation theory, the singlet free energy and the real part of the static energy are the same. From Fig. 3.9 we see that even non-perturbatively the difference between $\Omega(r,T)$ and $F_S(r,T)$ is very small, while the difference between the zero temperature static energy and $F_S(r,T)$ is even smaller for $rT < 0.4$ [69]. This is very similar to the findings of the calculations in quenched QCD, where smeared Wilson loops have been used [43].

It is straightforward to continue the parametrization of the Wilson line correlator given to Minkowski time and then calculate the dominant peak of the spectral function $\rho_r^{med}(\omega,T)$,

$$\rho_r^{med}(\omega,T) = \int_{-\infty}^{\infty} W(r,t,T)\exp(i\omega t)\,dt, \tag{3.7}$$

which has been plotted in Fig. 3.10.

We would like to again mention that the spectral feature $\rho_r^{med}(\omega,T)$ plotted in the figure is not the full spectral function $\rho_r(\omega,T)$, but rather the dominant peak of $\rho_r^{med}(\omega,T)$ due to the thermal static energy. $\rho_r^{med}(\omega,T)$ is quite different from the full spectral function $\rho_r(\omega,T)$ for ω far away from its peak at $\Omega(r,T)$. A similar situation arises also while calculating the $Q\bar{Q}$ potential in hadronic phase. In this case it is well known that the dominant peak of the spectral function is the Dirac delta function, and this describe only the plateau region of m_1.

The integration in Eq.(3.7) can be performed exactly [74] and near the peak, where $\rho_r^{med}(\omega,T)$ describes the spectral function reliably, it can

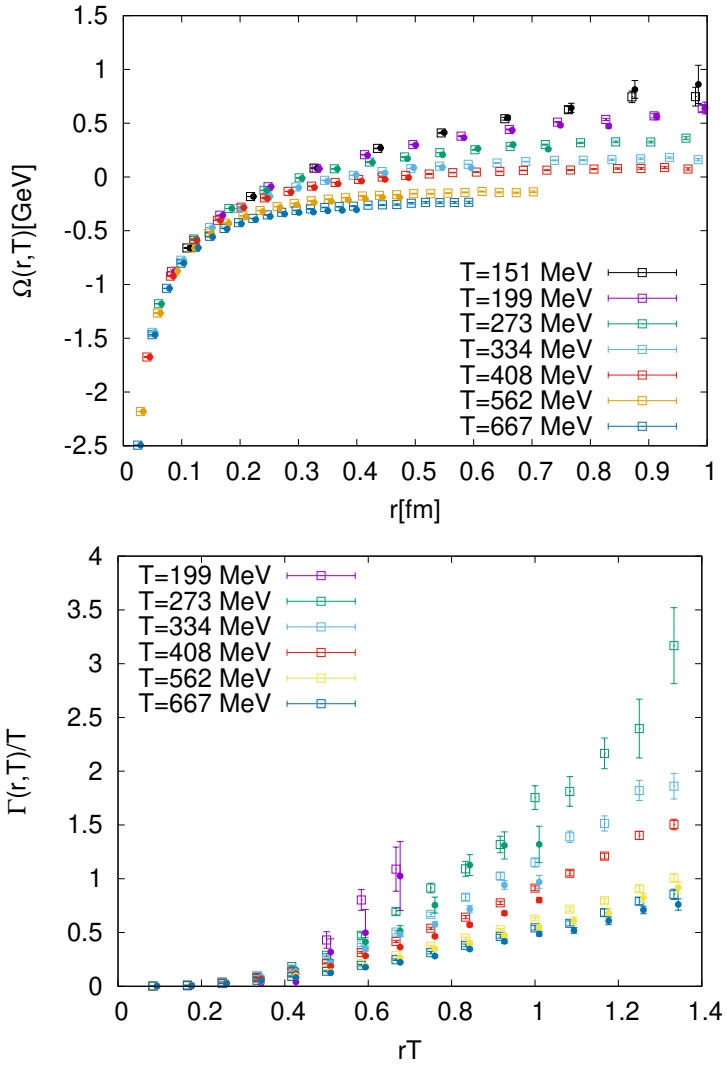

Figure 3.8: The peak position (left) and the width (right) from the HTL motivated method as function of r at different temperatures. The open(closed) symbols corresponds to real and imaginary part from unsubtracted(subtracted) correlator.

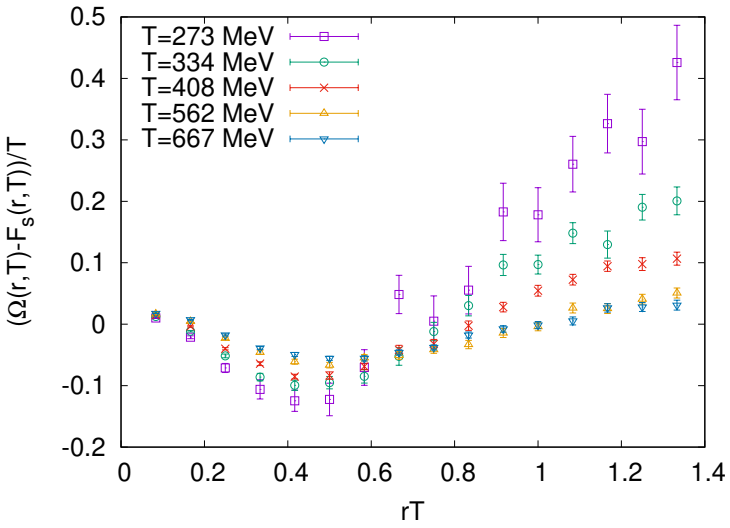

Figure 3.9: The difference between the peak position $\Omega(r,T)$ and singlet free energy $F_s(r,T)$ at different temperatures.

be approximated by

$$\rho_r^{med}(\omega,T) \approx \sqrt{\frac{2}{\pi}}\,\frac{\Gamma(r,T)}{(\Omega(r,T)-\omega)^2 \;+\; \Gamma(r,T)^2} \qquad |\Omega(r,T)-\omega|,\ \Gamma(r,T) \ll T. \tag{3.8}$$

3.4 Determination of the Peak using Padé interpolation

In this section we will determine the ground state peak position using the Padé rational approximation as outlined in section 2.2. Even though the Padé has it's limitations and does not reproduce the lattice euclidean data, our results on a non-trivial realistic test case are very promising, thus we proceed to apply it to our HISQ lattice data. We first start by showing a representative example is shown in fig. 3.11, where we plot as discrete data points in the top panel the real and in the bottom

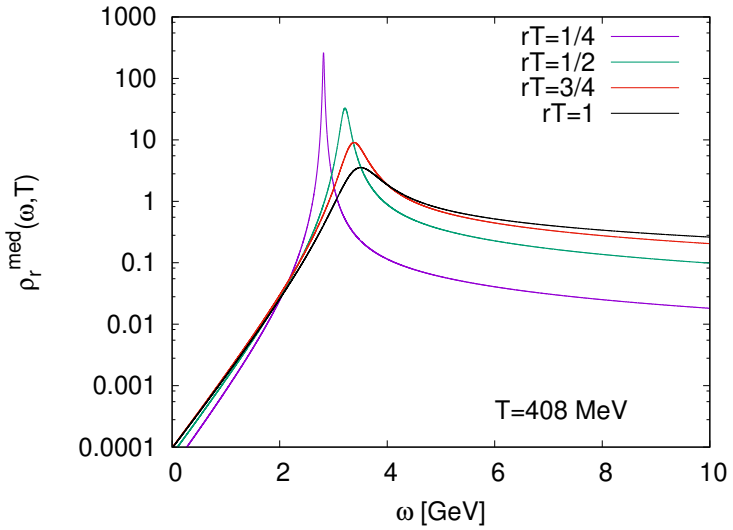

Figure 3.10: Dominant peak of spectral function for T=408 MeV at various distances from HTL-motivated method.

panel the imaginary part of the correlator at $T = 408$ MeV ($\beta = 7.825$ $N_\tau = 12$) at three spatial distances $r = 0.0387$ fm,$r = 0.176$ fm and $r = 0.296$ fm (dark blue to light blue), and then compare them to the interpolated function.

We then carried out the pole analysis for Pad´e interpolations based on different number of input datapoints. On $N_\tau = 12$ lattices the results are unaffected by changing between seven to eleven input points and we arbitrarily decide to show the results based on eight. The uncertainty budget represented by the error bars includes the Jackknife errors, as well as variation due to change in the ordering when composing the continued fraction. For the $N_\tau = 12$ lattices we investigated, the Padé interpolation yields one dominant pole close to the real axis manifesting itself as a well-defined skewed Lorentzian peak in the spectral function, as shown in fig. 3.12.

Reading off the values of the real-part of the pole as estimate for Ω we obtain the values plotted in fig. 3.13. The corresponding values for the

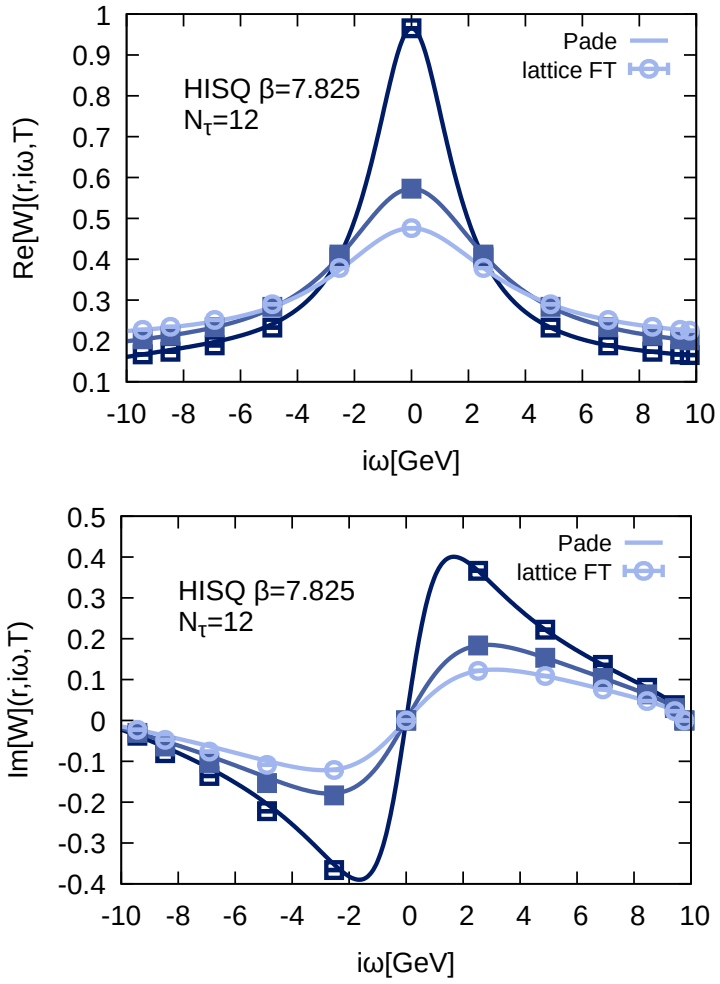

Figure 3.11: Discrete Fourier transform of the $T > 0$ Wilson line correlators at $T = 407$MeV ($\beta = 7.825$, $N_\tau = 12$) at three spatial separation distances $r = 0.03872$ fm, $r = 0.1758$ fm and $r = 0.2964$ fm. The top panel shows its real part, while the lower panel its imaginary part as colored symbols. The solid lines denote the Padé approximation based on eight data points, which is subsequently used in the analytic continuation.

imaginary part as estimate of Γ are shown in fig. 3.14.

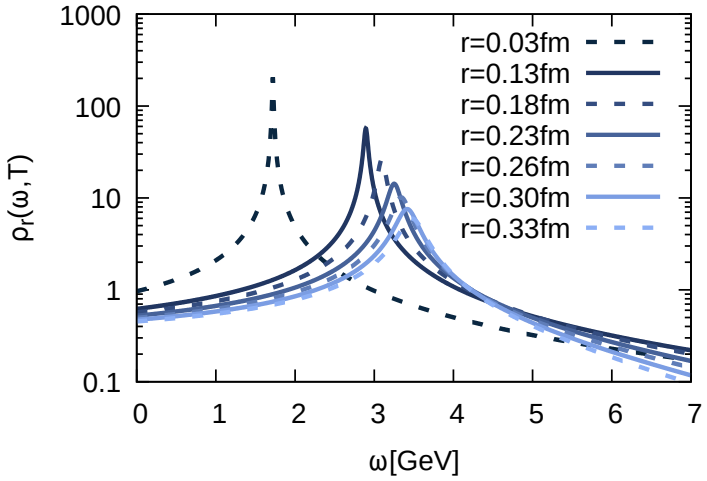

Figure 3.12: Representative spectral functions obtained from the Padé interpolation at $T = 407$ MeV ($\beta = 7.825$ $N_\tau = 12$) for different separation distances. A single well defined peak structure of skewed Lorentzian form emerges from the analysis.

As we are cautioned about the quantitative reliability of the extraction of Γ from the mock data analysis, we here present its values simply for completeness. We have carried out the analysis on both the subtracted and unsubtracted correlators and found that the subtracted correlators are computed to a statistical precision which unfortunately is not high enough for the Padé to extract the value of Γ with even statistical reliability.

The values the Padé analysis yields for Ω on the HISQ Wilson line correlators are similar to the results obtained from the model spectral function fits deployed in section 3.2. We find that the values do not show any significant changes over a large temperature range.

In fig. 3.15 we pick out the results at $T = 407$ MeV for a closer inspection. We plot Ω, based on the subtracted and unsubtracted Euclidean correlator Padé analysis at $T > 0$ (orange and dark blue data points), along with the $T = 0$ static energy (light blue datapoints) and the colour

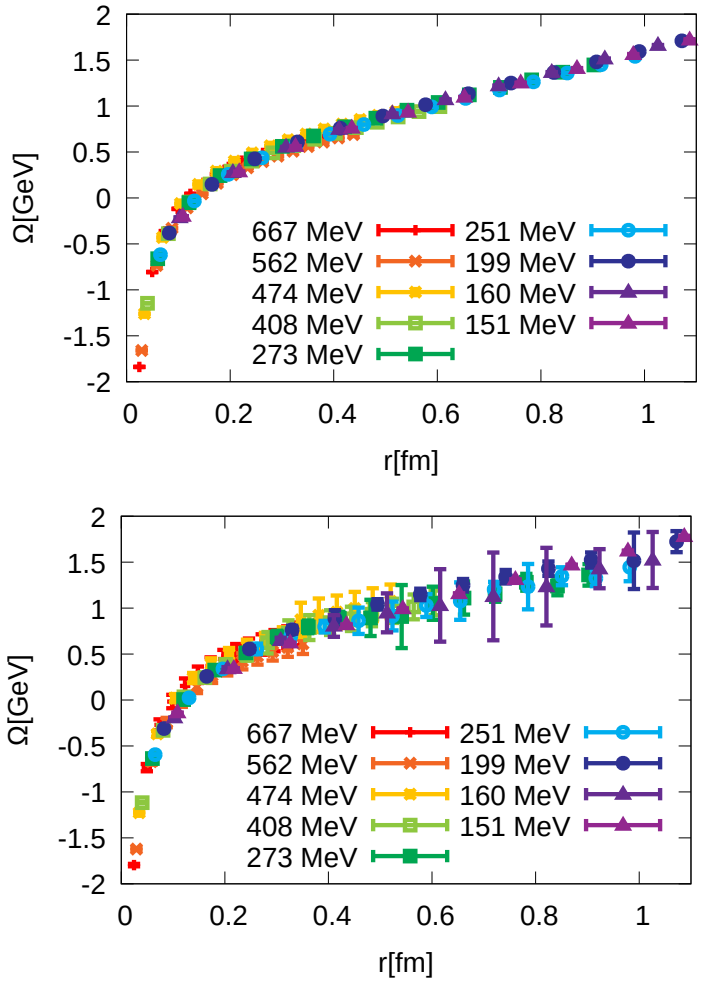

Figure 3.13: Ω as a function of separation distance for different temperatures obtained from a Padé pole analysis on $N_\tau = 12$. The figure on the top is obtained by using the unsubtracted correlator and the figure on the bottom is obtained using the subtracted correlator.

singlet free energy. The results obtained are in stark contrast to those of the method by Bala and Datta, in which at temperatures inside the QGP phase one does observe a deviation from the linear rise present in the hadronic phase. Our Pade results appear also in stark con-

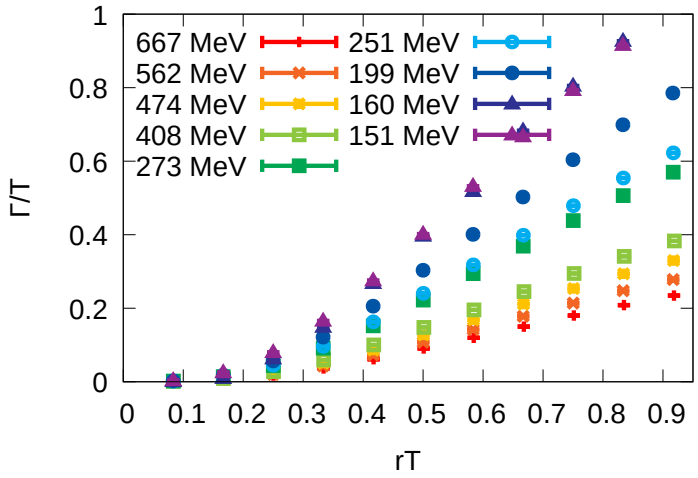

Figure 3.14: Width Γ as a function of separation distance for different temperatures obtained from Padé pole analysis for $N_\tau = 12$. The analysis is done using unsubtracted correlators.

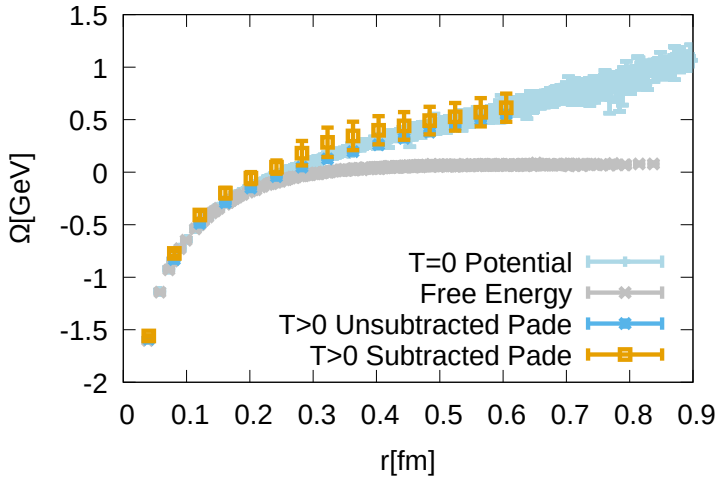

Figure 3.15: Comparison of extracted Ω using subtracted and unsubtracted correlators using Padé pole analysis with the T=0 effective mass and colour singlet free energy at $T = 408$ MeV ($\beta = 7.825$, $N_\tau = 12$).

trast to previous analyses of the spectral functions of Wilson lines from both quenched [41; 37] and dynamical QCD [61; 62] based on Bayesian methods. There a discernable change of Ω with temperature was found, more similar to the results of HTL-motivated method in this study. A previous Pade analysis of a subset of the HISQ data was discussed in Ref. [75]. That analysis showed relatively large uncertainties, arising from the fact that less statistics was available and that the improved frequencies were not deployed. Within its sizable uncertainties, these results were consistent with the Bayesian studies but within 2σ would also encompass the result obtained here.

3.5 Determining the ground state peak via Bayesian reconstruction

We then proceeded with the next method of analysis the Bayesian spectral reconstruction as outlined in section 2.1. The Bayesian analysis relies on the presence of positive definite spectral functions in the euclidean correlator data. In our analysis of effective masses, we observed that at high temperatures the effective masses of euclidean correlators show non-monotonic behaviour at small euclidean time, which, in the language of spectral functions represents a non-positive definite spectral function.

At low temperatures, e.g. at $T = 151$ MeV, the Euclidean correlators do not yet show signs of positivity violation (i.e. we obtain effective masses that are monotonic in Euclidean time) and the BR method succeeds in reconstructing their spectral function. By construction, the result reproduces the input Euclidean data points within their statistical errors. A selection of these spectra for $r = 0.32, 0.64, 0.96$ and 1.28 fm is shown in fig. 3.16 (solid dark blue to lighter blue) compared to the outcome of the Padé reconstruction (gray solid).

We find important differences between the two approaches. The BR method reconstructions, as expected from the effective mass analysis, shows a single well defined lowest lying peak. Towards the origin that

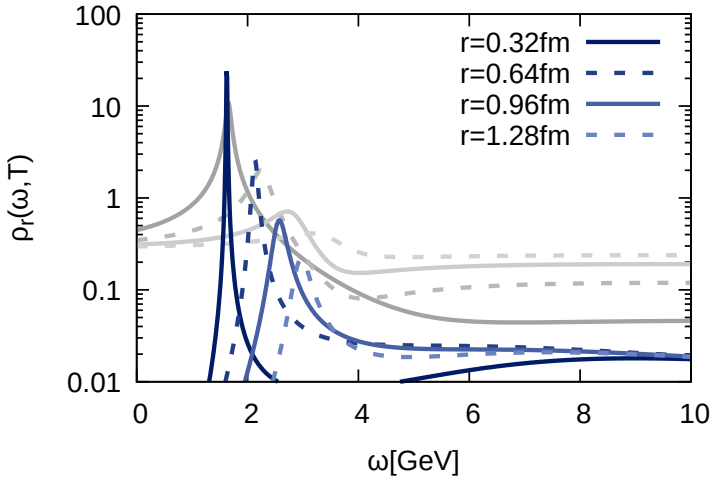

Figure 3.16: Comparison of reconstructed spectra using Pade (grey) and BR (blues) method at $T = 151$ MeV ($\beta = 6.740$, $N_\tau = 12$) at different separation distances $r = 0.32, 0.64, 0.96$ and 1.28 fm.

peak rapidly decays in an exponential fashion, qualitatively similar to the behavior observed in HTL spectral functions. In contrast the Padé reconstruction assigns significant weight to the low frequency region. This difference is among the reasons, why the spectral function of the Padé reconstruction does not fulfill the spectral decomposition of the original Euclidean data, a known drawback of the Padé reconstruction method.

At larger frequencies than its maximum, the BR spectral function shows a tail, which eventually behaves as $\propto 1/\omega$ per choice of the default model. We have checked that changing the default model to different powers α as $m \propto \omega^\alpha$ does not change the peak structure significantly. The central peak obtained by the BR method agrees in position with the Padé result at small separation distances but the Padé eventually seems to smear out significantly with the center of the bump lying at a higher frequency than the BR spectra peak.

The success of the BR reconstruction at $T = 151$ MeV tells us that the data is compatible with a dominant skewed Breit-Wigner peak struc-

ture in the spectral function. At higher temperatures the BR method cannot be reliably applied to the extraction of spectral functions from the raw correlators, due to the presence of non-positivity in the underlying spectral functions. At $T = 407$ MeV, for example, the effective masses at small distances show explicitly non-monotonic behavior [69]. However, the spectral density may not be positive definite even if the effective masses decrease monotonically. We see that also at intermediate distances, the BR method fails to converge successfully.

While in principle we could proceed by investigating the UV-subtracted finite temperature correlators, we have found that the statistical uncertainties introduced by the $T = 0$ subtraction dominate over those inherent in the $T > 0$ data, thus preventing us from a precision analysis of the spectral function at higher temperatures.

3.6 Conclusions

The main goal of this study was extracting the position Ω and width Γ of the dominant spectral peak structure encoded in the Wilson line correlators. We deployed four different approaches: spectral function model fits where the dominant peak is described by a Gaussian, the HTL-inspired fit of Bala and Datta, the Pade approximation and, where positivity allowed, the Bayesian BR method.

In essence each of the four methods introduces certain prior information in order to regularize the ill-posed inversion problem to gain access to the spectral function. It turns out that the Euclidean data scrutinized in the first part of our study is amenable to different possible hypotheses, which in turn lead to different outcomes for Ω and Γ.

The spectral function fits assume that the high energy part of the spectral function has negligible temperature dependence, and that the observed temperature dependence of the Wilson line correlators is determined by the dominant peak structure. Since the correlator is found to have a second cumulant much larger than its higher cumulants, a Gaussian for the dominant peak, and a single delta function for the low energy tail

are the simplest, permissible choices for parametrizing the data. The Gaussian spectral function model shows a value of Ω, which is virtually independent of temperature and a width, which scales trivially with the temperature.

In order to extract the values of Ω via the HTL-inspired fit, one assumes that the correlation functions are amenable to a certain non-standard spectral decomposition, similar to the one encountered in leading-order HTL perturbation theory. This spectral decomposition leads to a first cumulant that is anti-symmetric around $\tau = 1/(2T)$. Because of small N_τ, the fits can be performed only in a small region around $\tau = 1/(2T)$. This fit yields an Ω, which shows clear temperature dependence and signs of asymptotic flattening in the QGP phase. The width that the method computes shows a non-trivial scaling with the temperature, which is weaker than linear in the temperature.

The third method we deployed is the Padé rational approximation. The only assumption it makes is that the correlation function represents an analytic function. However it suffers from the drawback that its outcome is known to violate the spectral decomposition of the input data. I.e. the Padé spectrum, when reinserted into the Lehmann representation, does not reproduce the original correlator. We have however tested the Pade method under non-trivial settings in HTL perturbation theory and found that for the temperature and spatial separation distances probed, the position of the lowest lying peak structure was well reproduced. Applied to genuine lattice data we obtained results that were robust under changes in the number of input points and a reordering when constructing the Pade approximation of the Matsubara domain input data. The outcome of the extraction of Ω based on the Pade method yields values, which similarly to the Gaussian model fit, shows virtually no temperature dependence. While the mock data tests tell us to take the outcome of the width with a significant grain of salt, we find small statistical errorbars and a behavior that qualitatively agrees with that of the Bala-Datta method, i.e. Γ scales weaker than linear with the temperature.

Last but not least we also deployed the Bayesian BR method, where positivity allowed. The BR method has been extensively tested on HTL mock data and has been shown to outperform other Bayesian methods, such as the MEM in the accurate reconstruction of the lowest lying peak from Wilson line correlators, a finding reproduced in this study. As the BR method is designed to reproduce the Euclidean input data within their uncertainty, its reconstructed spectra denote a valid hypothesis for the actual underlying spectrum. The BR method possesses an explicit default model dependence, which however can and is assessed by repeating reconstructions for different functional forms of the default model. And while the BR method is known to be susceptible to ringing artifacts, as its regulator is weakest among the reconstruction methods on the market, no signs of ringing have been observed in this study, neither in the HTL mock test nor in the reconstruction of genuine lattice data.

As a crucial limitation in the context of the current study, the BR method is only applicable to positive definite spectral functions. If effective masses show non-monotonicity it indicates that the BR method cannot be deployed. However even if the effective masses are monotonous, positivity violation may persist, which explains that the BR method fails to converge successfully for higher temperatures on the raw Euclidean correlators. The outcome of the extraction of Ω, based on the BR method at low temperatures such as $T = 151$ MeV yields a real-part which agrees well with the static energy from (multi-state) exponential fits, also applicable on those lattices. We find that the spectral functions show well defined Breit-Wigner like peaks, which get exponentially cut off close to the origin, similar to what is seen in HTL perturbation theory at much higher temperatures. Comparing the BR result to the Padé we find that the Padé incorrectly assigns too much weight to the low frequency regime and at the same time produces a less and less well-defined peak, which is consistently located at a higher position than the BR peak. Agreement between the BR and the effective masses and the tension with the Pade method starting around $r = 0.5$fm seem to indicate that the Pade tends to overestimate the values of Ω when

applied to our lattice data.

The comparison of different methods of the spectral reconstruction in terms of the peak position, Ω of the dominant peak and its width, Γ is summarized in Fig. 3.17 and Fig. 3.18, respectively for three temperatures, $T = 151$ MeV (just below the chiral crossover), $T = 199$ MeV (the typical temperature most relevant for RHIC), and $T = 408$ MeV deep in QGP. The present study sheds new light onto the extraction of Ω and Γ. While different methods often lead to quantitatively different results some general features are the same. The width Γ is significant compared to the temperature scale and increases with distance r for all temperatures. In fact, for the lowest temperature all method give consistent results for Γ. For temperatures 150 MeV $< T <$ 200 MeV, the Gaussian fits and HTL fits lead to similar width for large r, while at small r the HTL fit gives a smaller width. The Pade method always gives a smaller Γ than Gaussian and HTL fits at large r, but agrees with the HTL result at small r, c.f. Fig. 3.18. The r dependence of the peak position turns out to be similar for the Gaussian fits and the Pade method, indicating an apparent absence of the screening effects. Furthermore in the temperature range 150 MeV $< T <$ 200 MeV and at intermediate distances, all the explored methods give a peak position that is slightly larger than the singlet free energy, see Fig. 3.17. For these temperatures, which are the most relevant ones for RHIC, the spread of the results is not too large in order to have an impact on the phenomenological studies. At higher temperatures, which are of interest for quarkonium phenomenology in heavy ion collisions at LHC our results are inconclusive at present, and lattice calculations with larger N_τ and smaller statistical errors are needed. Increasing the temporal extent of the lattice will be possible in the coming years. At the same time accumulation of statistics at $T = 0$ will also enable a high precision subtraction, which in turn will enable us to use the BR method above the crossover temperature.

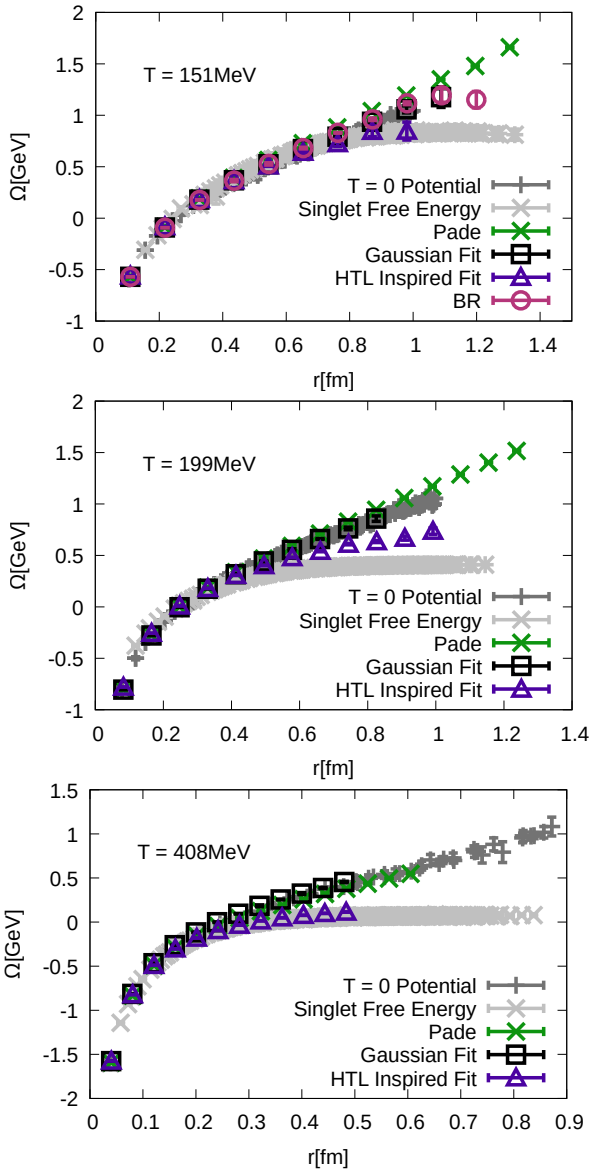

Figure 3.17: Comparison of Ω as a function of separation distances for three different temperatures 151,199 and 408 MeV obtained from different methods discussed in the text. We have also shown the T=0 potential (dark grey) for all temperatures and the free energy (light grey) for high temperature (408 MeV).

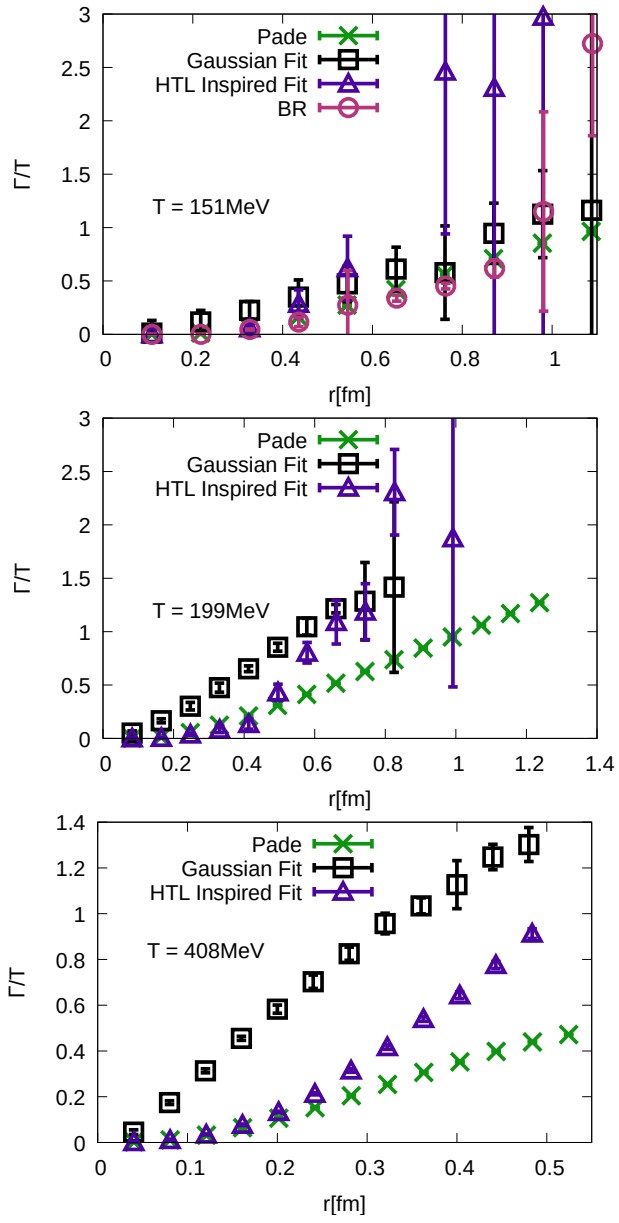

Figure 3.18: Comparison of Γ/T as a function of separation distances for three different temperatures 151, 199 and 408 MeV obtained from different methods discussed in the text.

4 Results from high resolution quenched lattices

[1]The real part of the potential obtained from the study on 2+1 Flavour QCD HISQ lattices showed no temperature dependence even when the temperature was increased to more than 650 MeV. These results were rather astonishing as they were completely different from the screened potential picture that was observed in previous studies on Quenched QCD[36; 37] and in full QCD simulations based on the legacy asqtad action [61; 62]. The potential in these studies was extracted using the Bayesian spectral reconstruction which was inapplicable for the study on HISQ lattices due to positivity violation of the spectral function which was manifested in non-monotonicity of the effective masses at small τ. Thus, it was essential to compare the new methods to the Bayesian reconstruction in the regime where all the approaches were applicable. The Quenched lattices do not show this non-monotonous behaviour in the effective masses. Thus it is a good testing ground for comparison between the methods. This might also give us some more insights into the differences between legacy studies and the recent study on HISQ lattices.

4.1 Lattice setup

The Coulomb-gauge Wilson line correlators are computed on high-resolution isotropic and anisotropic quenched lattices. Both sets of ensembles are based on the naive Wilson action, the former utilizes a parameter set ($\beta = 7.196$), which has been used in the study of relativistic bottomonium physics at finite temperature in [76] with a transition temperature of 313 MeV and lattice spacing $a = 0.0176$ fm with total volume of $96^3 \times N_\tau$ with $N_\tau = 16, 24, 48$, the latter ($\beta = 7, \xi = 3.5$) in previous studies of quarkonium melting in [37] with transition tem-

[1]The contents of this chapter have been taken from a preprint [40] where the author has contributed substantially towards writing, generation of data, analysis of data and figure creation.

N_τ	16	24	48
T[MeV]	698	466	232
T/T_C	2.23	1.49	0.74
N_{meas}	8700	4500	1600

Table 4.1: A table of isotropic quenched lattice ensembles at $\beta = 7.196$, lattice spacing $a_s = 0.0176$ fm with $N_s = 96$.

N_τ	24	32	40	56	96
T[MeV]	839	629	503	359	210
T/T_C	3.11	2.33	1.86	1.33	0.78
N_{meas}	2500	1014	735	708	172

Table 4.2: A table of quenched anisotropic lattice ensembles at $\beta = 7$ and $\xi = 3.5$, lattice spacing $a_s = 0.039$ fm with $a_\tau = a_s/4$ and $N_s = 64$.

perature $T_c = 270$ MeV, spacial lattice spacing $a_s = 0.039$ fm and temporal lattice spacing $a_\tau = a_s/4$ with total volume of $64^3 \times N_\tau$ with $N_\tau = 24, 32, 40, 56, 96$. The anisotropic lattices were generated using the openQCD code by the fastsum collaboration which has been extended to anisotropic lattices [77] by utilizing the Fram supercomputer maintained by Sigma2 in Norway. The configurations were gauge-fixed to Coloumb gauge with a tolerance of $\Delta_{GF} = 10^{-12}$ and the Wilson line correlators were measured using the SIMULATeQCD code [78] on the MARCONI100 computing cluster in Italy. The isotropic lattices were generated at the university of Bielefeld and some of the measurements were also performed there. A summary of measurements at various temperatures for isotropic lattices are shown in table 4.1 and for anisotropic lattices are shown in table 4.2.

4.2 Effective Masses

Following in the footsteps of the mock data test, we start by analysing the effective masses of the Wilson line correlator on the quenched lattices in fig. 4.1. The observation we have both for the isotropic

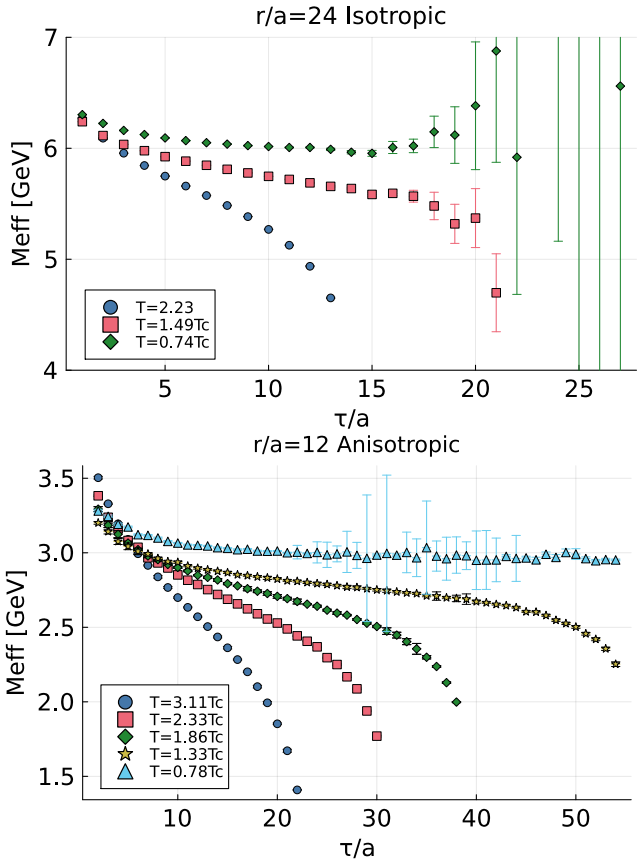

Figure 4.1: A representative selection of effective masses, obtained from the Coulomb-gauge Wilson line correlator computed on (top) isotropic ($\beta = 7.196$) and (bottom) anisotropic ($\beta = 7, \xi = 4$) quenched lattices.

and anisotropic lattices is that for $T < T_c$ the effective masses show a tendency to plateau at intermediate τ. The small τ behaviour in the correlation function represents the large frequency contribution (UV) in the spectral function. The presence of a plateau at intermediate τ suggests the spectral function comprises of a lowest lying delta peak plus additional UV contribution that comes from the small τ regime; this is reminiscent of zero temperature behaviour where one expects there to be a well defined lowest lying peak described by a delta function. Such

behaviour is to be expected since in the absence of dynamical fermions there exists a first order transition from the confined to the deconfined phase.

At $T > T_c$ we see that the effective masses obtain a non-zero slope at intermediate τ, which suggests the presence of a finite width in the spectral function. The structure of the small τ behaviour is rather interesting. On the one hand, for the anisotropic lattices for $T = 3.11T_c$ and $T = 2.33T_c$ there are significant deviations at small τ when comparing the $T > T_c$ and $T < T_c$ case. These differences are diminished as the temperatures are reduced to around $1.86T_c$ and below. On the other hand, for the isotropic lattices we find agreement at small τ for both available temperatures ($T = 2.23T_c$ and $T = 1.49T_c$) as compared with a recent study of $(2+1)$-flavour QCD [38]. However, as all recent QCD studies were based on the improved Lüscher-Weisz gauge action, and also on gradient flow smearing in the case of [38], these two factors might contribute to the different observations as well. Qualitatively similar to the mock tests, we see a bending in the effective masses at large τ. We understand this bending effect at $\tau \lesssim 1/T$ as being due to the interaction of a forward propagating static quark-antiquark pair and backward propagating states of the medium [49].

The behaviour in quenched QCD is quantitatively different from the behaviour of effective masses in the mock HTL Wilson line data. There are significantly more UV contributions present in the lattice data which is manifested in the upward bending at small τ. However, the magnitude of UV contribution is less than that the case of Wilson loop HTL mock data. The magnitude of the UV contributions in lattice data lie in between those of the Wilson line and the Wilson loop mock data. From the analysis of effective masses alone we cannot make a statement about the structure of the high frequency behaviour of the spectral function.

Despite different behaviour of M_{eff} on anisotropic quenched lattices at small τ, we follow the steps as described in section 2.4 and section 3.2 and show the subtracted correlator analysis. We also note the fact that

we might be over-subtracting or under-subtracting the high-frequency part. If we are indeed over-subtracting we might be doing something non-trivial to the spectral function that is relevant for the potential effects. An example of the high-frequency subtracted effective masses are shown at $T = 2.23T_c$ (isotropic) and $T = 2.33T_c$ (anisotropic) in fig. 4.2. We carry out the subtraction procedure for all temperatures on the anisotropic lattices for $T > T_c$ at all but the highest temperature as the small τ behaviour is very far from being compatible with the zero temperature behaviour for the $T = 3.11T_c$ anisotropic lattices. The details of these fits are shown in fig. 4.24 and fig. 4.25 in the appendix.

Thus, for each temperature we obtain two different correlators to perform spectral reconstructions on, i.e. the subtracted correlator and the raw correlator. We expect the spectral functions of the raw correlator to show structures at large frequencies owing to the high-frequency effects at small τ and these effects will be suppressed on the subtracted correlator. Since these high-frequency structures are related to be non-potential effects there is little need in reconstructing them accurately. Thus, the subtraction procedure attempts to get rid of irrelevant information while at the same time keeps the number of points in the τ direction fixed from the input data, in turn the information content on the small frequency regime should increase thus improving the outcome of spectral reconstruction. However, the subtraction procedure could affect the analysis in other ways. The subtraction is done by dividing the zero temperature raw correlator data into 16 jackknife bins and then performing a weighted fit to a single exponential. Once the fit parameters are obtained, the single exponential is subtracted from each jackknife bin. The remaining part of the correlator is used for subtraction from the finite temperature case. The subtraction will introduce new errors (coming from a mismatch in statistics in zero and finite temperature data) in the data and the spectral reconstruction will be limited by the statistics of the zero temperature data. The statistics on the zero temperature data for anisotropic lattices is limited in our case (we have about 175 uncorrelated measurements). Nevertheless, we

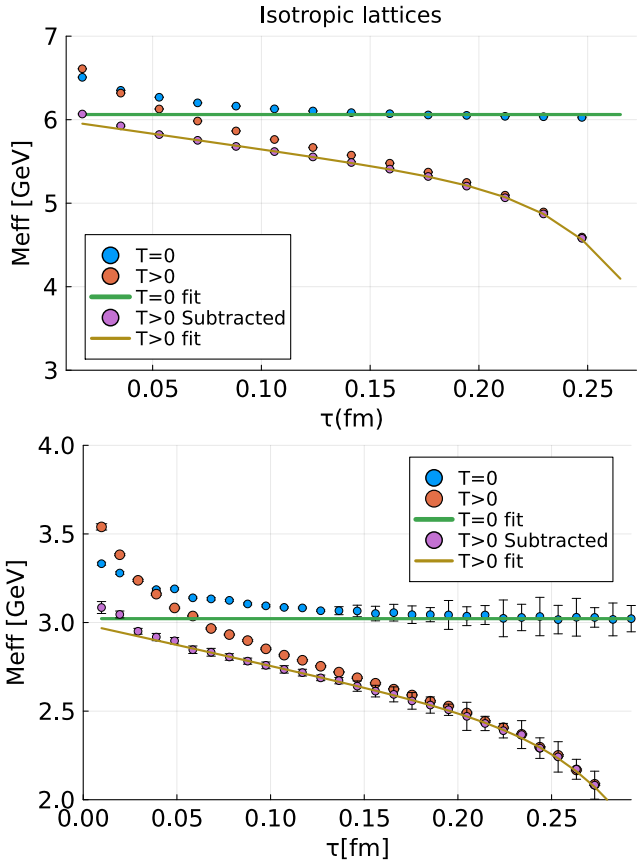

Figure 4.2: An example of subtracted effective masses for (top) r = 0.441 fm for the $T = 2.23T_c$ isotropic lattices and (bottom) r = 0.467 fm at $T = 2.33T_c$ for anisotropic lattices. Here the $N_\tau = 48(0.74T_c)$ and $N_\tau = 96(T = 0.78T_c)$ lattices are used as the zero temperature reference .

expect that the gains made from reducing the severeness of ill-posed problem will outweigh the losses coming from limited statistics in the subtracted data.

Next we show the HTL-inspired fits as outlined in section 2.3 and use the fit form as described in eq. (2.23) to obtain the value of the potential. We were able to fit the data quite well upto a large τ region with two

higher order terms c_1 and c_2. The fit on effective masses are shown in fig. 4.3. We were able to get the fit within the margin of error for all but the smallest and largest τ data. We have shown the details of the fits in fig. 4.27 and fig. 4.26 in the appendix. We find that the fits are somewhat worse than the Gaussian fits. For eg, considering the case of $T = 2.33Tc$ anisotropic lattices ($N_\tau = 32$), at a separation distance of $r = 0.585$fm with first 5 and last 3 points excluded we get an error (χ as usual in statistics) of 4.16 per degree of freedom (number of τ points) as compared with the Gaussian fits where this number is 0.172 for the same. The HTL fits perform considerably better when the τ range is restricted close to $\tau = \beta/2$. The same quantity reduces to about 0.24 when the first 8 and the last 5 points are excluded in the HTL fits. The somewhat counterintuitive observation that the HTL-inspired fits work better at lower temperatures is understood from the fact that a smaller fraction of the points are affected by discretization artifacts at $\tau \approx 0$ or $\tau \lesssim 1/T$ that is not accounted for at all in the HTL inspired Ansatz.

4.2.1 Spectral Reconstructions

In this section we use the Bayesian BR method and the Padé interpolation method to reconstruct the spectral function from the Wilson line correlators. We use a large frequency range $\omega \in [-56, 112]$ GeV for isotropic lattices and $\omega \in [-101, 202]$ GeV for anisotropic lattices with $N_\omega = 2000$ in both cases, starting with the most uninformative default model i.e. $m(\omega) = \text{const}$. The natural second step now is to compute the spectral functions from UV continuum subtracted data. This does present a challenge since the subtracted correlator will now have statistical errors dominated by the zero temperature data, since those are the ensembles where we have the lowest statistics (table 4.1 and table 4.2). The available statistics are thus reduced by a factor of 5-10 when the analysis will be carried out on the subtracted correlator. Nonetheless, we still perform the subtraction procedure (see section 2.4 and section 3.2) and proceed with running the BR reconstructions. We

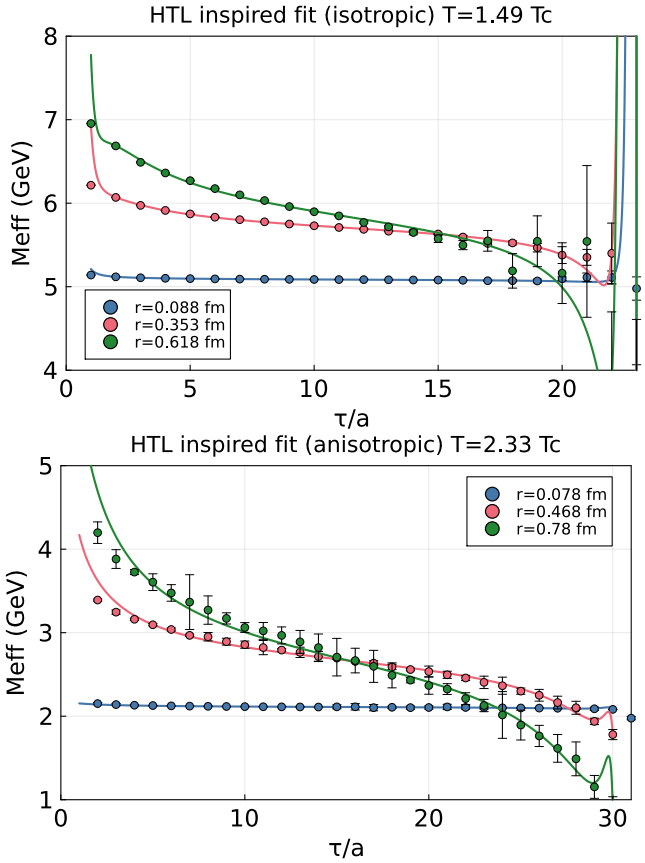

Figure 4.3: The figure shows HTL-inspired fits on effective mass data on isotropic (top) and anisotropic (bottom) lattices at three different separation distances.

proceed in the following way: the mean of the UV contribution is subtracted from each measurement of the correlator. Then, we account for the larger errors in this new subtracted data by multiplying the covariance matrix with the appropriate factor which is determined by comparing relative errors of the zero and finite temperature data. The actual procedure for spectral reconstruction is the same as with the raw correlators. We first show a comparison of the spectral functions at different temperatures at a fixed separation distance of $r = 0.53$fm in

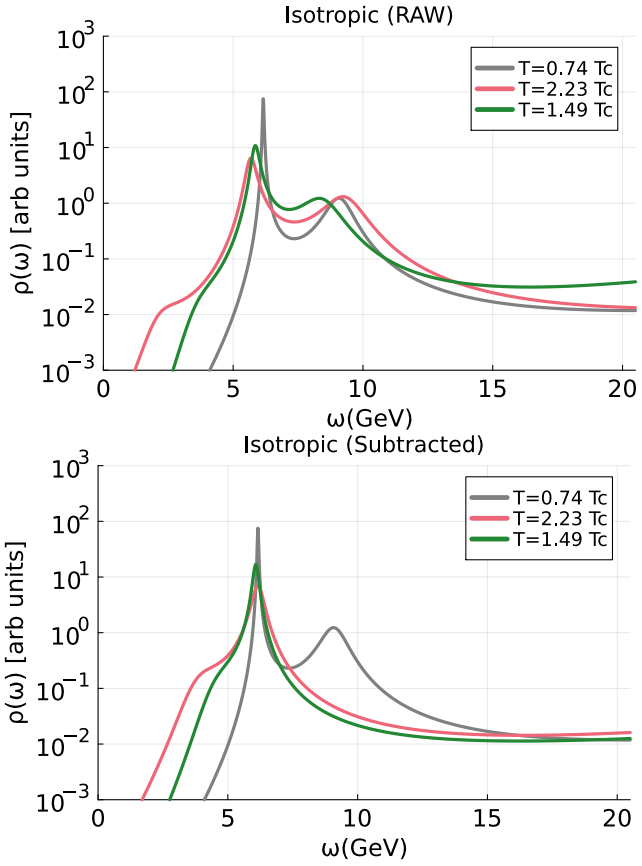

Figure 4.4: Comparison of BR reconstructed spectral functions at different temperatures $T \in (2.23, 1.49, 0.74)T_c$ at a separation distance of $r = 0.53$fm. The figure on the top shows $\rho(\omega)$ for raw correlators and the figure on the bottom shows $\rho(\omega)$ for subtracted correlator.

fig. 4.4 (isotropic) and $r = 0.702$fm in fig. 4.5 (anisotropic).

When compared to reconstructed spectral functions of HTL Wilson Line correlators we see more structure in the spectral function. The spectral functions from the raw data on isotropic lattices show some shoulder structures at small positive frequencies below the main dominant peak, whereas in the case of anisotropic lattices the shoulder structures appear at a negative frequency. In addition, we also find other

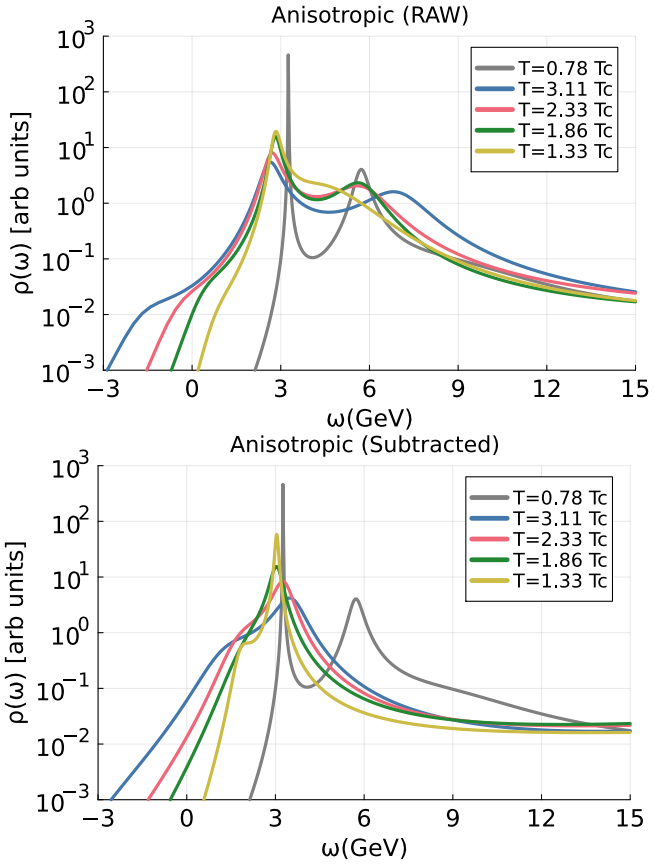

Figure 4.5: Comparison of BR reconstructed spectral functions at different temperatures at a separation distance of $r = 0.702$ fm. The figure on the top shows functions for raw correlators and the figure on the bottom shows the functions for subtracted correlator.

structures at higher frequencies (around 8-10 GeV for isotropic and 5-6 GeV for anisotropic lattices) which correspond to UV continuum artifacts affecting the small τ behaviour in the correlator. Performing the same analysis on the subtracted correlator still shows a dominant peak and some shoulder structures at small frequencies remain, but the frequencies at which these structures appear are slightly higher and the amplitude is also lower. These changes might be due to τ-dependent statistical fluctuations of the $T = 0$ correlators at large times, where

one would otherwise naively expect just the stable ground state contribution. Comparing the raw or subtracted effective masses at large τ in full QCD [49; 38] suggests milder changes in the low-frequency region of the spectrum, which however, is known to be strongly operator dependent and susceptible to lattice artifacts. The structures at higher frequencies that we observe from the raw data do not appear anymore, suggesting that the subtraction procedure has indeed removed the high frequency parts of the spectral function as intended. In addition, the position of the dominant peak in the spectral function also appears to have shifted to slightly higher frequencies. In all cases the width of the spectral peak increases with increasing temperatures, which suggests the presence of an imaginary part which grows with temperature.

Next we compare the spectral functions at a fixed temperature for different separation distances to analyse the change in peak position and width. Figure 4.6 shows spectral reconstructions using the BR method for raw correlators $T = 2.23T_c$ (isotropic) and $T = 2.33T_c$ (anisotropic) at different separation distances and fig. 4.7 shows the same for the subtracted correlators. We observe that the position of the dominant peak for raw correlators stabilises at a fixed position at around $r = 0.45$fm (isotropic) and $r = 0.39$fm (anisotropic). This suggests the presence of screening in the real part of potential. However, for the subtracted correlators no stabilization of the peak position is seen, and hence, no screening. We hence confirm results obtained in previous studies. The width of the spectral peak also appears to broaden over increasing separation distance suggesting the presence of an increasing imaginary part with separation distance in the potential. We discuss the potential extraction from spectral functions in section 4.2.2 where we also discuss the systematic and statistical error-budget in our analysis where is presented.

We proceed to do the same with the Padé interpolation reconstruction. We will display here the spectral functions obtained from the Padé, however, note that we compute the potential from the pole analysis in the next section. As mentioned earlier, the Padé requires very high

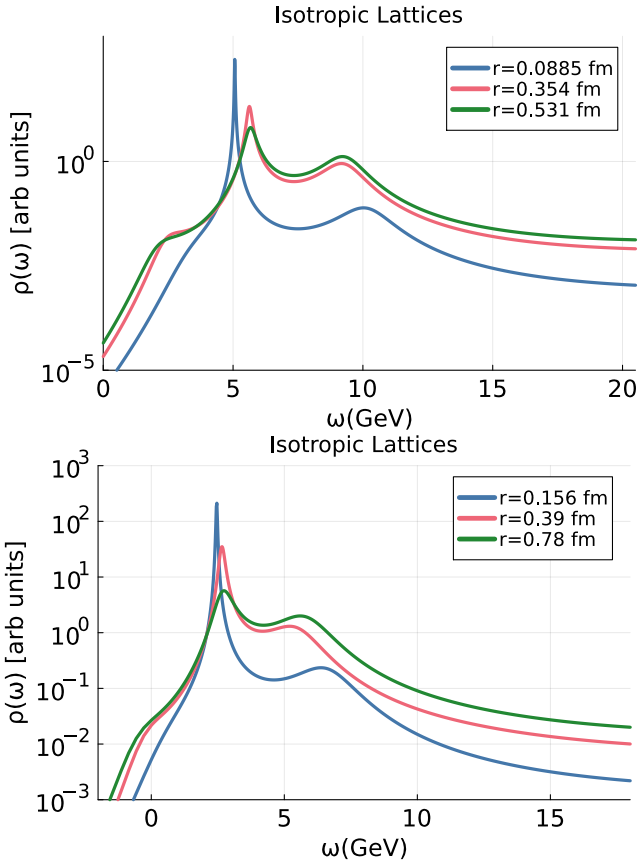

Figure 4.6: BR reconstructed spectral functions of the (top) isotropic lattices at $T = 2.23T_c$ and (bottom) anisotropic lattices at $T = 2.33T_c$ using the raw correlator data. The three curves each denote spectra at different spatial separation distances.

statistics, which makes it less reliable on the subtracted correlator. The subtraction procedure is carried out in a slightly different way from the BR reconstructions. We divide our data into 16 jackknife bins and first obtain the high-frequency part of the $T = 0$ correlator for each bin. This continuum part is then subtracted from the finite temperature data for each jackknife bin. This was only possible for the isotropic lattices where the statistics were high enough, the interpolation fails

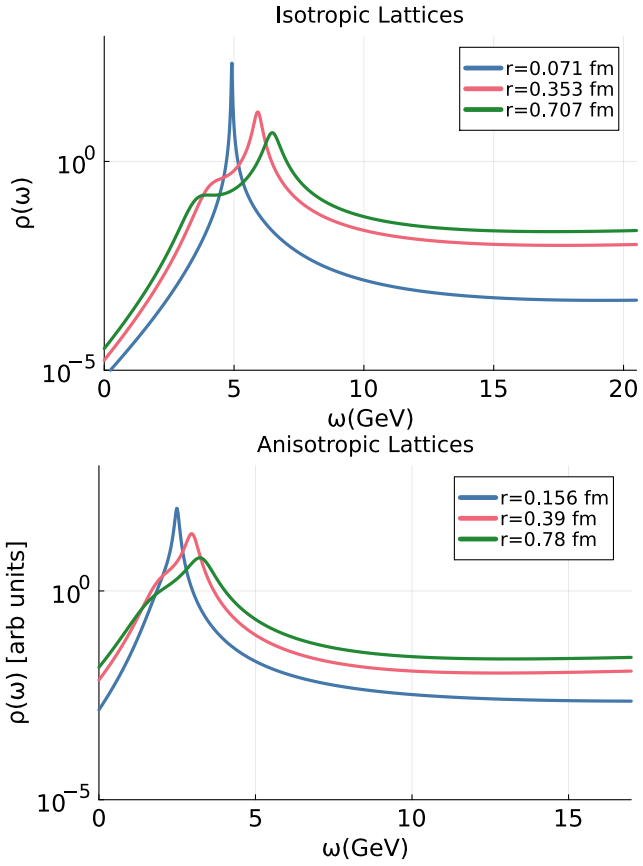

Figure 4.7: BR reconstructed spectral functions of the isotropic lattices at $T = 2.23T_c$ and anisotropic lattices at $T = 2.33T_c$ using the subtracted correlator data. The three curves each denote spectra at different spatial separation distances.

for the anisotropic case. Figure 4.8 shows a comparison of the Padé extracted spectral functions on isotropic lattices for the raw correlators (top) and subtracted correlators (bottom) at a separation distance of $r = 0.53$fm. Firstly, the spectral peak of the vacuum ($T = 0.74T_c$) is now somewhat broader than the peak obtained from the BR reconstruction on the same lattice. The spectral functions for raw correlators at all temperatures show a main dominant peak, followed by a second bump

at high frequencies at about 7-12 GeV. These bumps correspond to high frequency structures in the UV which dominate the correlator at small τ. These bumps are not observed in the spectral functions of the subtracted correlator. This is an additional indication that the structures in the UV are indeed removed by the subtraction procedure. The shoulder structures that are observed in the BR also seem to be absent in the Padé reconstructions which could very well be because the Padé is unable to capture them. Furthermore, the subtraction procedure changes the peak position of the spectral function in a non-trivial way. The peak has been shifted to a higher frequency for both the temperatures alike. The reconstructed peak for the subtracted correlator now even sits at a higher position than the vacuum peak obtained from the raw correlators. This suggests that the presence of some non-trivial structures at high frequency can affect the Padé and could lead it to underestimate the peak position or that the subtraction affects the low lying part of the spectral function itself. This is reminiscent of the changes to the low-frequency shoulder structures seen in the BR reconstructed spectra.

Next, we compare the spectral functions at the same temperatures but at different separation distances. fig. 4.9 shows spectral functions of the raw correlator on isotropic (top) and anisotropic (bottom) lattices and fig. 4.10 shows the same for the subtracted correlator but now only for the isotropic lattices. We find that when using the raw correlator, the position of the dominant peak approaches a constant at a separation distance (around 0.4 fm) suggesting the presence of screening in the real part of the potential. This changes drastically when using the subtracted correlator as the peak position keeps increasing even up to separation distances of 0.7 fm. This behaviour is not compatible with a screened potential and could be interpreted as a vacuum-like rising real part.

We have described and compared spectral functions of the raw and subtracted correlators on both isotropic and anisotropic lattices in this section. Visual analysis suggests that the subtraction procedure removes high frequency structures. At the same time the subtraction affects the

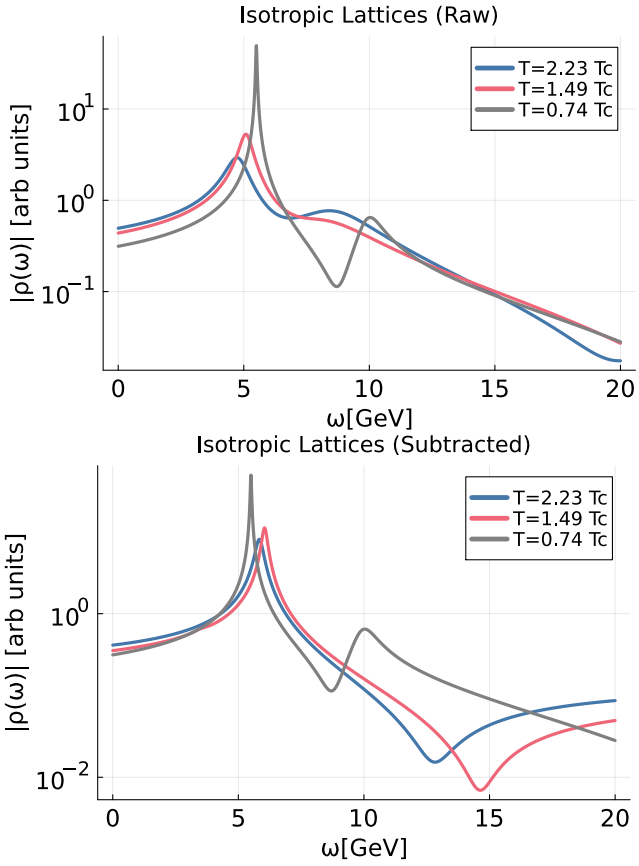

Figure 4.8: Comparison of Padé reconstructed spectral functions at different temperatures at a separation distance of $r = 0.53$ fm. The figure on the top shows functions for raw correlators and the figure on the bottom shows the spectral functions for subtracted correlator. The zero temperature reconstruction is performed on the raw correlator in both the plots.

reconstructed peaks at small frequency. It also suggests that the raw correlators show signs of screening confirming results from previous studies. However, the subtracted correlators show behaviour compatible with the vacuum. In the next section we will present the real part of the potential extracted using all the methods discussed in this paper along with providing statistical and systematic uncertainty budgets.

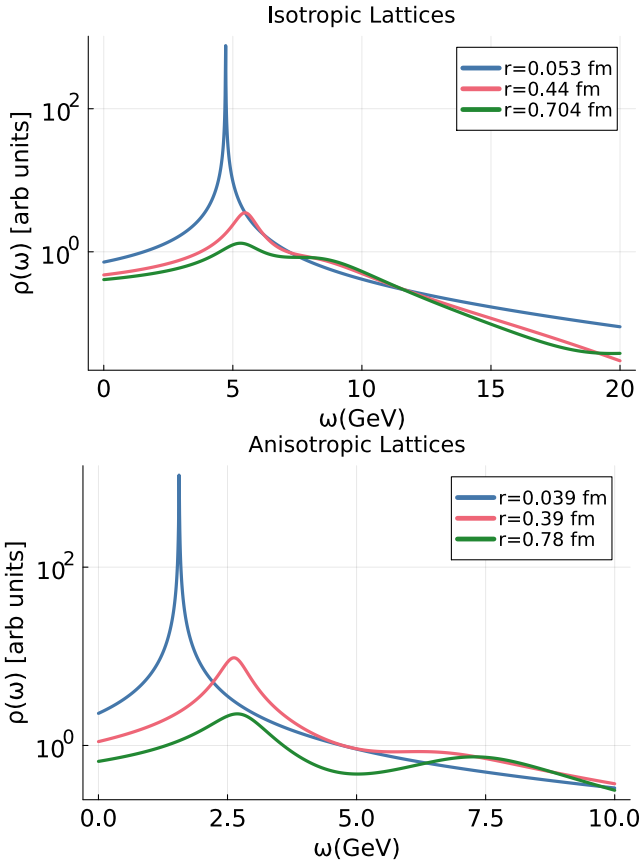

Figure 4.9: Padé interpolation reconstructed spectral functions of the (top) isotropic lattices at $T = 2.23T_c$ and (bottom) anisotropic lattices at $T = 3.11T_c$ using the raw correlator data. The three curves each denote spectra at different spatial separation distances.

4.2.2 Real part of the potential

We now discuss the real part of the potential from each of the methods described in the previous sections. We extract the potential from spectral functions by fitting to a functional form according to eq. (1.33). In HTL mock data tests we observed that the BR reconstructions can approach a failure mode resulting in ringing behaviour (see fig. 2.6) when the errors on the data are reduced without increasing the number of data

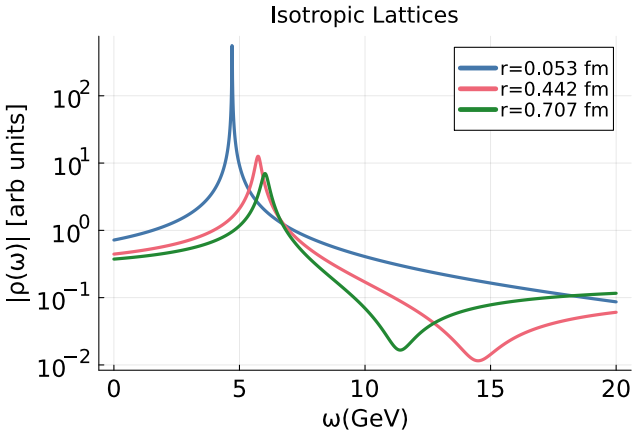

Figure 4.10: Padé interpolation reconstructed spectral functions of the isotropic lattices at $T = 2.23T_c$ using the subtracted correlator data. The three curves each denote spectra at different spatial separation distances.

points. This could result in a sudden jump in the extracted potential above at a certain separation distance (see fig. 2.8). To check whether we observe such effects in the lattice data we artificially reduce the statistics on our data to a factor of 2/3 and 1/3 of total measurements. The top part of fig. 4.11 shows the real part of potential extracted using a constant default model for with varying statistics at $T = 3.11T_c$ ($N_\tau = 24$) on anisotropic lattices. Seeing no jump in the extracted real part suggests the reconstruction is unaffected by ringing artifacts.

We then proceed with estimating the systematics of the extracted potential. Generally, the least informative default model is used in Bayesian reconstruction i.e. a constant default model. To test the default model dependence we choose four different default models in addition to the constant default model; $m(\omega) = \frac{m_0}{(\omega-\omega_{min}+1)^\kappa}$ where $\kappa = [1, 2, -1, -2]$. For the highest temperature ($N_\tau = 24$ anisotropic lattices) we also choose an additional value $\kappa = -3$ since we expect the dependence to be the highest at this temperature. The resulting values of the real part for the anisotropic lattices of $T = 3.11T_c$ ($N_\tau = 24$) is shown in the bottom panel of fig. 4.11. We estimate the systematic error in the

extracted potential from the maximal variation among these data points. We point out that the residual slope for some of the default models is much weaker than the slope due to the effective string tension in the confined phases, c.f. fig. 4.12, such that the default model dependence does not hinder distinction between screening or no screening.

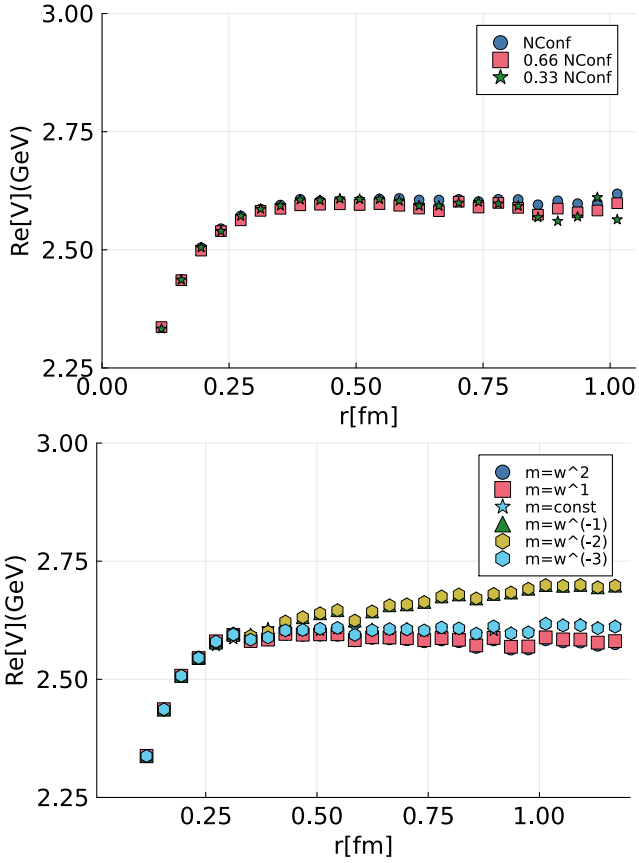

Figure 4.11: Assessing the dependence of the Bayesian reconstruction extracted values of $\mathrm{Re}[V]$ on (top) variation in the statistical error of the input data (bottom) on changes in the default model (anisotropic ensemble at $T = 3.11T_c$).

In our simulations, the temperature is changed by changing the number of lattice points while keeping the lattice spacing fixed. Thus, at

higher temperatures we have fewer imaginary time steps and thereby less information. Since it is known from precise data in full QCD [79] that the low-lying excited states become negligible at $T = 0$ only after $\tau \gtrsim 0.4$ fm, one might be concerned that the $T > 0$ analysis could be affected by uncontrolled excited state contamination due to the restricted time range. To investigate these effects, we carry out the BR reconstruction on the low temperature ($T = 0.78T_c$, $N_\tau = 96$) data with artificially truncated Euclidean time range to $\tau/a < 24$ as shown in fig. 4.12.

We observe that truncating the data to $N_\tau = 24$ introduces a small upward shift in the potential in line with the expected excited state contamination. This behaviour is similar to what was observed in a previous study on lattice NRQCD S- and P-wave bottomonium states [80]. This artifact only leads to over-estimation of $\mathrm{Re}[V]$ and does not mimic artificial screening.

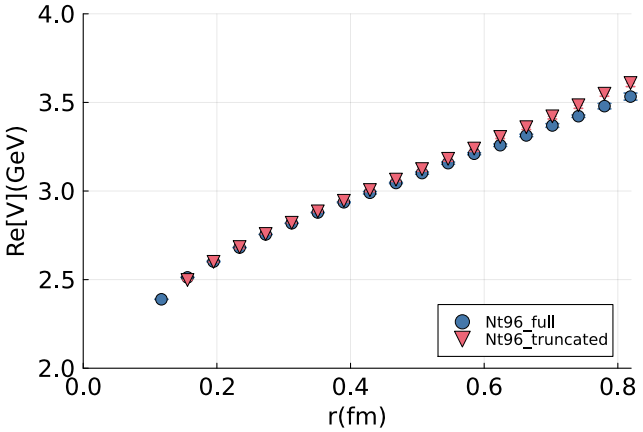

Figure 4.12: Assessing the dependence of the Bayesian reconstruction at $T = 0.78T_C$ on the available extent in imaginary time. Each of these was computed using the full statistics with the same constant default model (isotropic ensemble at $T = 0.78T_c$).

After combining the statistical and systematic errors the real part of the potential extracted from the raw correlators is shown in fig. 4.13

and from the subtracted correlator in fig. 4.14. The BR analysis on the raw correlator suggests the presence of screening at $T > T_c$ for both the isotropic lattices and anisotropic lattices. However, when applied to the subtracted correlator, we see a substantially different behaviour, the screening has diminished if not disappeared, and the real part is– within the sizable uncertainty–compatible with the zero temperature potential. For the isotropic lattices the real part shows almost no temperature dependence within error bars. For the anisotropic lattices, there is some inconclusive temperature dependenceincompatible with the screened behaviour found from the raw correlators. This is an intriguing finding and further investigation is needed to find the sources of the discrepancy of the real part of the potential between subtracted and unsubtracted correlator.

Given that we see such different behaviour of the real part of the potential in the Bayesian reconstruction we proceed with the extraction of the potential using the Padé interpolation to confirm whether it, too, shows similar results. We calculate the potential by inspecting the dominant pole of the Padé interpolation function in eq. (2.15) as described in section 2.2. The error budget is estimated in two ways. The first one is the statistical errors. These are obtained from a jackknife procedure with 16 jackknife bins. Since the Padé does not have any explicit regularization we have to be conservative in estimating systematic errors. We proceed in the following way. Let us choose the minimum number of points at which a good interpolation[2] with a smooth function is seen. Then we add one and two more points from the negative frequency side. This gives us three different realisations of the potential and thus a range of uncertainty. In our tests we have observed that the systematic uncertainty dominates the statistical uncertainty at higher temperatures and gradually starts reducing when decreasing temperatures. This is primarily due to the fact that more points in the τ direction become available, so adding additional points in the interpolation has less of an

[2]By good interpolation we mean an interpolation function which passes through all the data points which are not used as in explicit input for the interpolation function along with having no kinks or discontinuities.

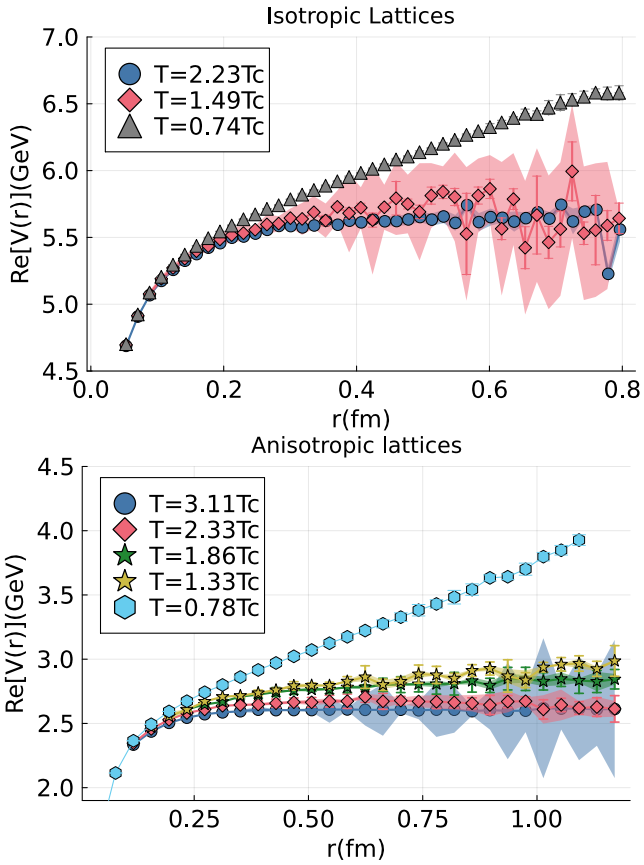

Figure 4.13: Real part of the potential at different temperatures using the BR method from (top) isotropic and (bottom) anisotropic lattices. The error bands denote systematic errors and the error bars refer to statistical errors. The zero (T_c) temperature potentials are calculated by fitting the effective masses to a constant in the regime where a plateau is observed.

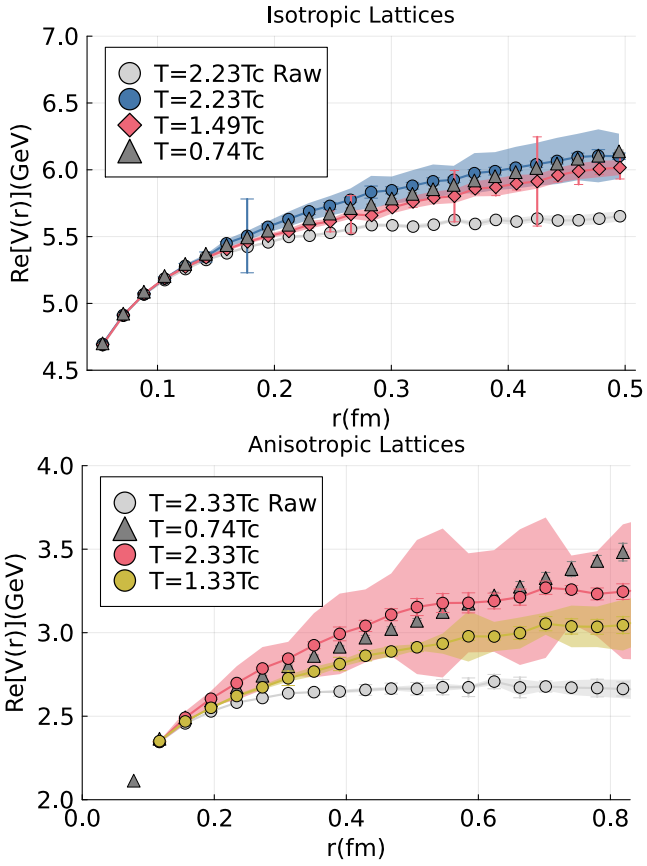

Figure 4.14: Real part of the potential at different temperatures using the BR method from subtracted (top) isotropic and (bottom) anisotropic lattices. The error bands denote systematic errors and the error bars refer to statistical errors. To understand the effects of subtraction we show (in light grey) the potential obtained from the raw correlator at one temperature.

effect. The real part of the extracted potential using the Padé on raw correlators is shown in fig. 4.15 and using the subtracted correlators is shown in fig. 4.16.

We observe that even though the systematic errors are large, the real part of the Padé interpolated potential flattens off at large distances

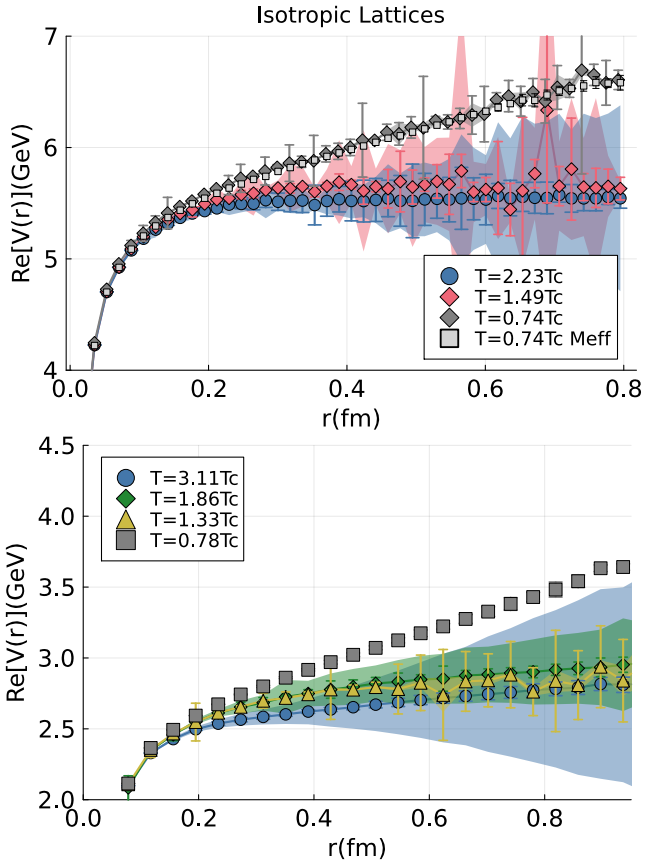

Figure 4.15: Real part of the potential at different temperatures using the Padé method from (top) isotropic and (bottom) anisotropic lattices. The error bands denote systematic errors and the error bars refer to statistical errors.

for the raw correlators. The extracted potential on the raw correlators for both isotropic and anisotropic lattices is in agreement with the BR reconstructed real part, i.e. it is compatible with screening. The subtracted correlator analysis can only be performed reliably on the isotropic lattices due to the lack of statistics in the zero temperature lattices in the anisotropic case. The real part extracted in this way shows more of a temperature dependence when compared to the BR reconstructions, but, still does not flatten out at large distances as one

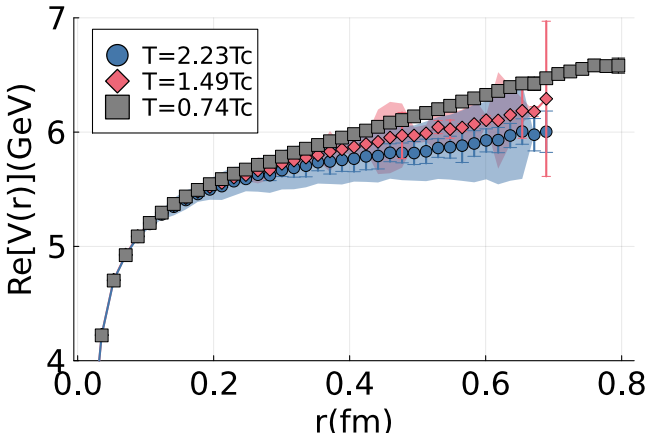

Figure 4.16: Real part of the potential at different temperatures using the Padé method from isotropic lattices with the subtracted correlator. The error bands denote systematic errors and the error bars refer to statistical errors.

would expect from a screened potential. The Padé analysis confirms the behaviour observed with the Bayesian reconstruction.

The next method we discuss is the potential extraction from the subtracted correlator using the Gaussian fit Ansatz. In fig. 4.2 we observed that after the zero temperature subtraction, the effective masses showed linear behaviour at intermediate τ followed by a downward bending. The agreement with the linear model extends to small τ values with decreasing temperatures. The downward bend at large τ can be parameterized in terms of a sum of delta functions at frequencies much lower than the peak: as in QCD [45; 49; 38] we find a single delta function sufficient given the data. We thus parameterise the UV subtracted correlator as:

$$C_{sub}(r,t) \approx A \exp\left(-\Omega\tau + \frac{1}{2}\Gamma^2\tau^2 + O(\tau^3)\right) + A_{cut}\exp(-\omega_{cut}\tau) \quad (4.1)$$

The spectral function can thus be represented as, suggested in [49]

$$\rho(\omega,T) = A(T)\exp\left(-\frac{|\omega-\Omega(T)|^2}{2\Gamma(T)^2}\right) + A^{cut}(T)\delta(\omega-\omega^{cut}(T)) \quad (4.2)$$

The real part of the potential as obtained from the Gaussian fits is shown in fig. 4.17. The error bars represent statistical uncertainty and are obtained by the jackknife procedure with 16 bins. We observe that for the isotropic lattices the behaviour of $\mathrm{Re}[V]$ is compatible with that at zero temperature without a clear trend of temperature dependence. For the anisotropic lattices, there is more temperature dependence present, but, without a clear trend the behaviour is still compatible with an unscreened potential. We discuss the goodness of these fits in section 4.4.

The last method we present in our discussion is the HTL-inspired fits described in section 2.3. In the previous study on (2+1)-flavour HISQ lattices we had observed that the results of $\mathrm{Re}[V]$ from this method were different from results obtained from Padé and the Gaussian fits. Here, we wish to establish whether that is still the case. When two higher order terms c_1 and c_2 in eq. (2.23) are included in the fits in the data fits the functional form up to a significantly large τ region away from $\tau = \beta/2$ (see fig. 4.3), and the potential is estimated from the parameters of this fit. The goodness of these fits is shown in section 4.4. We show the extracted potential using the HTL-inspired fits in fig. 4.18. The error bars represent statistical errors obtained from a jackknife analysis with 16 bins. The figure shows the real part as a function of separation distance using the raw correlator data, but we find that the results remain unchanged when using the subtracted data. We observe a screened potential from all of these fits.

4.2.3 Imaginary part of the potential

The mock data analyses carried out in chapter 2 indicated that with the currently available data quality of $N_\tau \sim 20$ and $\Delta D/D = 10^{-2}$, only a robust reconstruction of the real-part is possible. Both the BR and the Padé method applied to the HTL Wilson line data underestimated the imaginary part by around a factor of $1/2$. In light of these limitations the goal of this section is quite modest: we investigate whether there exists a non-zero imaginary part of the in-medium static potential. A

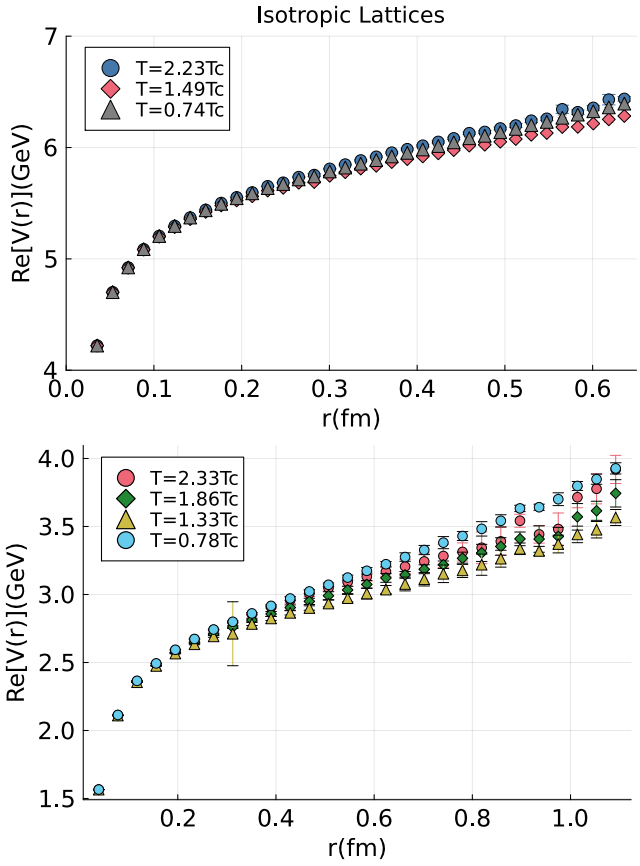

Figure 4.17: The figure shows the real part of the potential using Gaussian Fits on isotropic (top) and anisotropic (bottom) lattices. The potential below T_c is computed by fitting the effective mass with a constant in the regime where a clear plateau is observed.

careful estimate of the total uncertainty budget will be provided.

Our analysis indicates that despite the sizable uncertainties, a non-zero imaginary part is present for temperatures in the deconfined phase $T > T_c$. At the same time we confirm that in the confined phase $T < T_c$ both methods show an imaginary part that is compatible with zero.

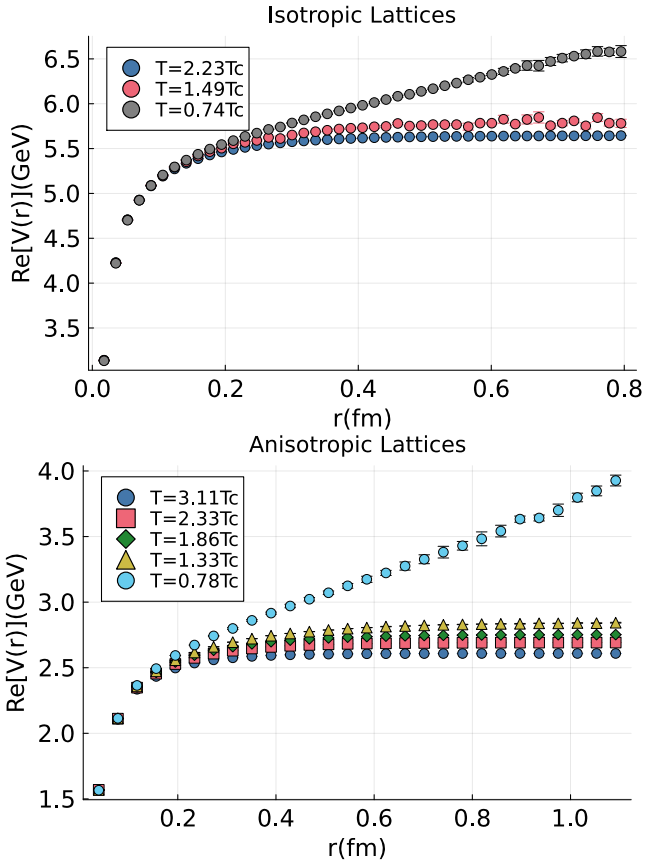

Figure 4.18: Real part of the potential at different temperatures using the HTL inspired method from (top) isotropic and (bottom) anisotropic lattices. The error error bars refer to statistical errors.

We start first by revisiting the effective masses in fig. 4.1. For both isotropic and anisotropic lattices they exhibit a plateau at intermediate τ values for $T < T_c$ which is compatible with a delta-function like spectral function and thus a zero imaginary part. For the higher temperature lattices ($T > T_c$) the plateau is absent and instead one finds a finite slope at intermediate τ. As discussed before, this linear behaviour extends over an even longer imaginary time duration in the subtracted correlator as shown in fig. 4.2. The presence of this slope may be interpreted as the finite width of a Gaussian or cut-off Lorentzian spectral peak encoding

the imaginary part of the potential. The corresponding Gaussian model fits were discussed in section 4.2.2, and we show the width parameter as a proxy for width in fig. 4.19. As the authors of Refs. [38] have pointed out, while the width parameter is model dependent, while the associated second cumulant is not.

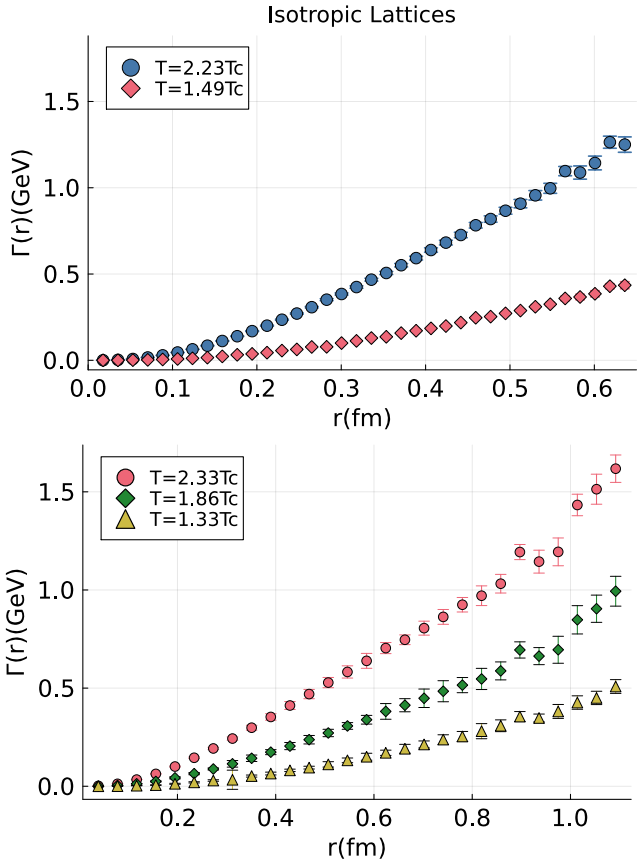

Figure 4.19: The figure shows the extracted Gaussian width parameter Γ (related to the imaginary part of the potential) on isotropic (top) and anisotropic (bottom) lattices. The error bars refer to statistical errors computed from the jackknife analysis.

Besides the Gaussian model Ansatz, the HTL-inspired Ansatz with two extra terms, too, is able to fit the data within the errors except

for the first and the last few points (number of points depend on the temperature and separation distances) as shown in figs. 4.26 and 4.27), with the error per degree of freedom being slightly worse. The slope in the effective masses is attributed to a finite imaginary part, the extracted values of which are given in eq. (2.23) in fig. 4.20.

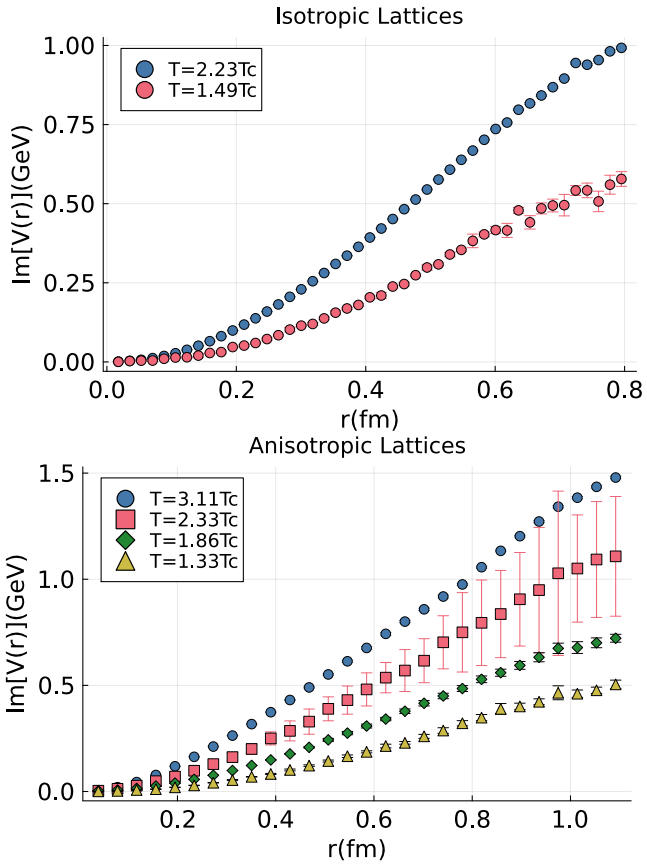

Figure 4.20: Imaginary part of the potential at different temperatures using the HTL inspired method from (top) isotropic and (bottom) anisotropic lattices. The error bars refer to statistical errors computed from the jackknife analysis

.

In order to determine the presence or absence of an imaginary part in a model independent fashion using the BR or Padé method, we

need to obtain a reliable uncertainty estimate of the extracted spectral widths.

One known artifact is related to the fact that the temperature is changed by changing the physical length of the Euclidean time domain. Because it is known that this change can affect the resolution of Bayesian reconstruction methods, we need to make sure that it does not artificially introduces a finite width. To this end we carry out the BR reconstruction on the low temperature ($T = 0.78T_c$, $N_\tau = 96$) correlator data, after artificially truncating the Euclidean time to only 24 points, the same extent as available at the highest temperature. We then compare the outcome of this reconstruction with the results from reconstruction on the fully available data-points in fig. 4.21. In both cases we find a statistically non-vanishing imaginary part for $r > 0.4$ fm even in the confined phase, but more than one order of magnitude smaller than in the deconfined phase. We observe that the mean of the extracted imaginary part from the truncated data has a tendency to sit slightly below the one from the full data. However, when error bars are considered the two are virtually indistinguishable.

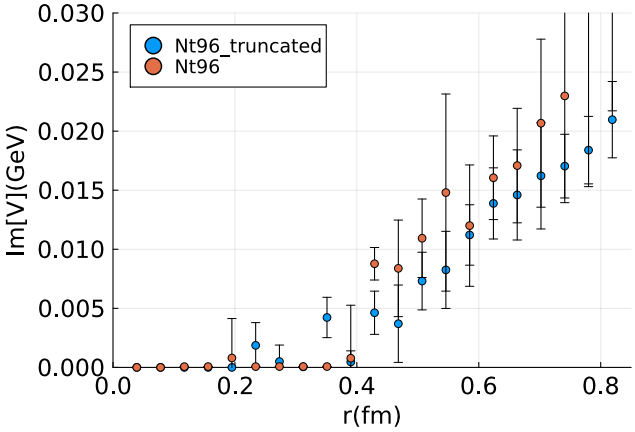

Figure 4.21: Assessing the dependence of the Bayesian reconstruction at $T = 0.78T_C$ on the available extent in imaginary time. Each of these was computed using the full statistics with the same constant default model.

The BR extracted imaginary part is shown in fig. 4.22 using the raw correlator. For the isotropic case, and the anisotropic case wewsee that the high temperature lattices show a finite imaginary part for both, while the low temperature lattices show a behaviour that is compatible with zero up to $r > 0.7$ fm). The error-bars are computed in the same way as in the real part (see section 4.2.2).

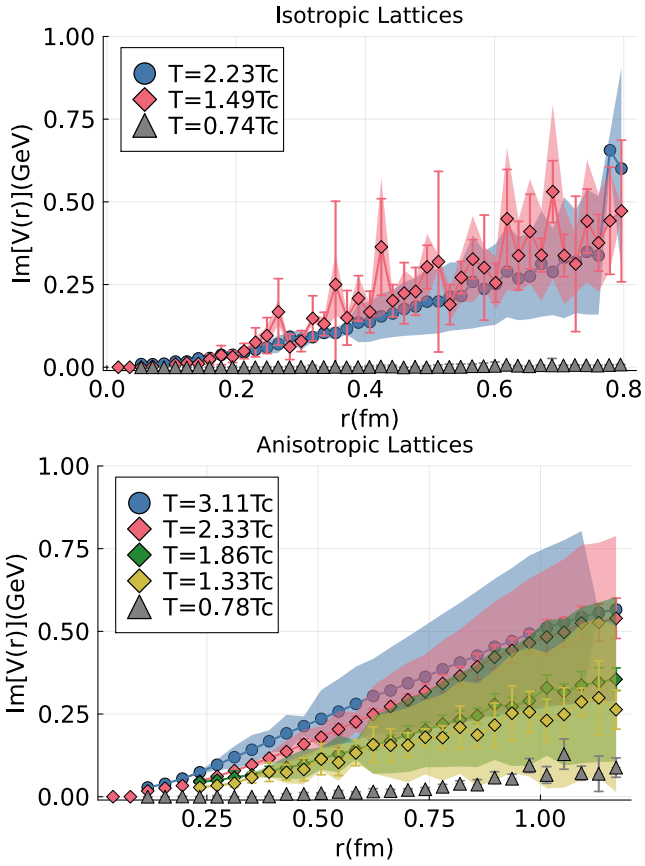

Figure 4.22: Imaginary part of the potential at different temperatures using the BR method from subtracted (top) isotropic and raw (bottom) anisotropic lattices. The error bands denote systematic errors and the error bars refer to statistical errors. The imaginary part is consistent with zero till around 0.6 fm.

Lastly, in fig. 4.23 we show the extracted imaginary part from the Padé

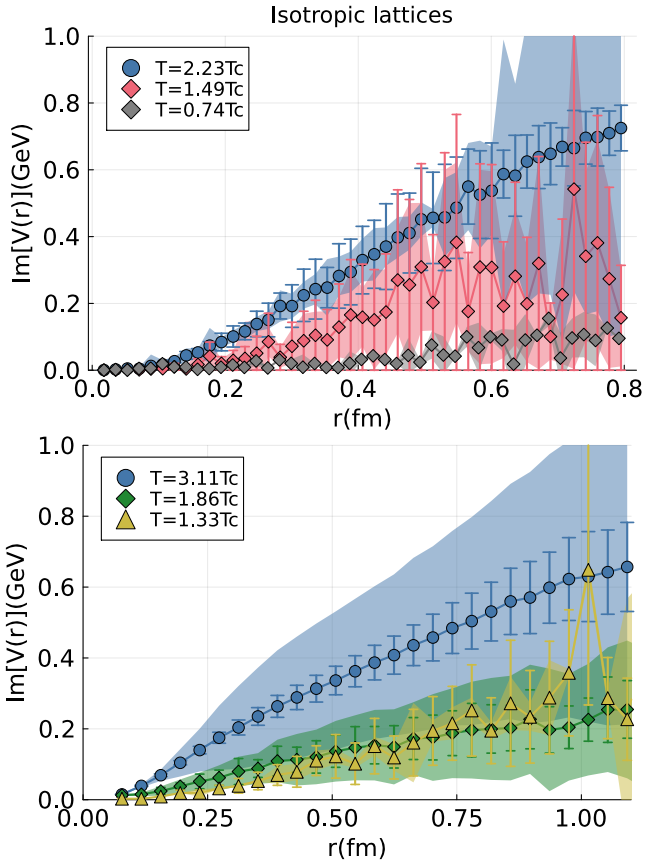

Figure 4.23: Imaginary part of the potential at different temperatures using the Padé method from (top) isotropic and (bottom) anisotropic lattices. The error bands denote systematic errors and the error bars refer to statistical errors. We observe that for both isotropic and anisotropic the imaginary part is zero up to 0.7 fm after which we see a small increase.

interpolation from the raw correlator. The imaginary part is nothing but the imaginary part of the dominant pole of the Matsubara correlator whose real part had been used to extract the real part of the potential. The statistical and systematic errors have been computed using the same procedure as for the real part. For the isotropic lattices we clearly see that there is a non-zero imaginary part for $T = 2.23T_c$ even when the

large uncertainties are considered. The uncertainties are too large for the case with $T = 1.49T_c$ to make such a claim, but nonetheless the obtained mean is non-zero. For the low temperature case $T = 0.74T_c$ the extracted imaginary part is compatible with zero up to at least $r > 0.6$ fm. For the anisotropic lattices, we see that there is a positive imaginary part for all $T > T_c$. Our attempt to extract real and imaginary part of the dominant pole fails for the low temperature ($T = 0.78T_c$, $N_\tau = 96$) case due to lack of statistics for those ensembles.

4.3 Summary and Conclusions

We have re-investigated the static quark-antiquark potential in a gluonic medium at finite temperature using high resolution isotropic and anisotropic quenched QCD lattices. We deploy four different independent methods, all of which have different underlying assumptions in analyzing the spectral structure of Euclidean correlators. We first started with analysing the correlation functions and their effective masses. The small τ behaviour of the latter showed non-trivial temperature dependence (on anisotropic lattices) unlike what the authors of [49] reported. Yet the case for zero temperature subtraction can still be made keeping in mind the possibility of under-subtracting and over-subtracting which could affect the reconstruction adversely.

After analysing the correlation functions themselves we investigated the real part of the potential using each of the methods described in the paper on both the subtracted and raw correlator. We find that the results from the raw correlator using the BR, Padé and HTL-inspired fits agreed with previous studies on quenched lattices and showed the presence of screening in the real part of the potential for both isotropic and anisotropic lattices. Since the Gaussian fit Ansatz is only applicable to the subtracted correlator we do not deploy it on the raw correlator. In contrast when the same analysis (except HTL-inspired fit, which is hardly impacted by data outside of $\beta/4 < \tau < 3\beta/4$) is performed on the subtracted correlators we observe that the real part of the potential no longer shows screening. These different outcomes due to the subtraction

are rather puzzling and further analysis is needed to identify the source of these differences.

The intention behind the subtraction procedure is to remove structures in the spectral function that are irrelevant for the potential physics by allowing the lowest lying peak to dominate more of the available data it attempts to reduce the severity of the ill-posed inverse problem. Since the Bayesian reconstruction relies on properties such as smoothness in the spectral function, presence of some non-smooth structures induced e.g. by the lattice cutoff in the UV can distort the spectral reconstruction and one may speculate that they could cause it to systematically underestimate the peak position. In such a hypothetical scenario it is possible that the subtracted correlator does not suffer from these discontinuities and thus allows for a more accurate determination of the actual spectral function. On the other hand, even though the motivation for subtraction is well motivated in full QCD and on isotropic lattices in quenched QCD, the agreement of effective masses at small τ is not as good on anisotropic lattices in quenched QCD.

The BR is able to reconstruct the Wilson loop peak in our mock data analysis with a spectrum that is rising at its high-frequency end, see fig. 2.2. However, the raw Wilson line correlator on the lattice has instead a second, bumpy structure at higher frequencies, see Figures 4.4 or 4.5. This is apparently much more difficult for Bayesian inference. Such a second bump also shows up in the Padé analysis of the raw Wilson line correlator on the lattice. Therefore, we suggest focusing the attention on such high-frequency bumps.

Given the quality of data with $N_\tau \sim 24$ and $\Delta D/D = 10^{-2}$, our mock data tests underestimated the imaginary part of the potential. For this reason we decided to focus on merely determining the presence or absence of an imaginary part of the potential at different temperatures. We have shown that all our methods indicate the presence of a non-zero imaginary part in the deconfined phase that increases with temperature and separation distance.

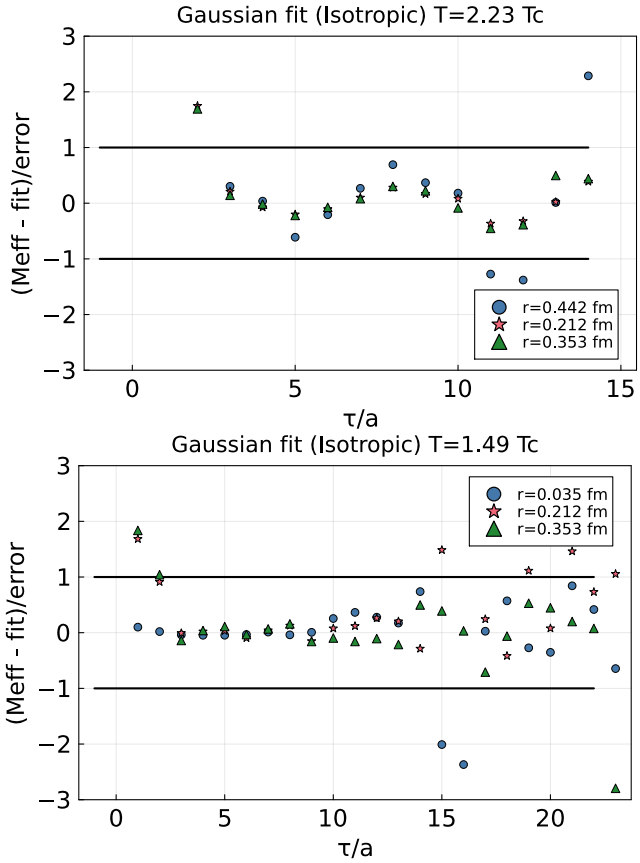

Figure 4.24: Goodness of gaussian fit on subtracted isotropic lattices at three different separation distances.

4.4 Appendix-Quality of fits

In this section we discuss the goodness of fits on the euclidean correlator. Figure 4.24 and fig. 4.25 show the goodness of the gaussian fits on isotropic and anisotropic lattices respectively. See eq. (4.1) for the fit form. The gaussian fits the subtracted correlator throughout the τ range upto a relatively large separation distance except for the first few points and the last couple of points in some cases.

Figure 4.26 and figs. 4.27 and 4.28 show the goodness of the HTL-

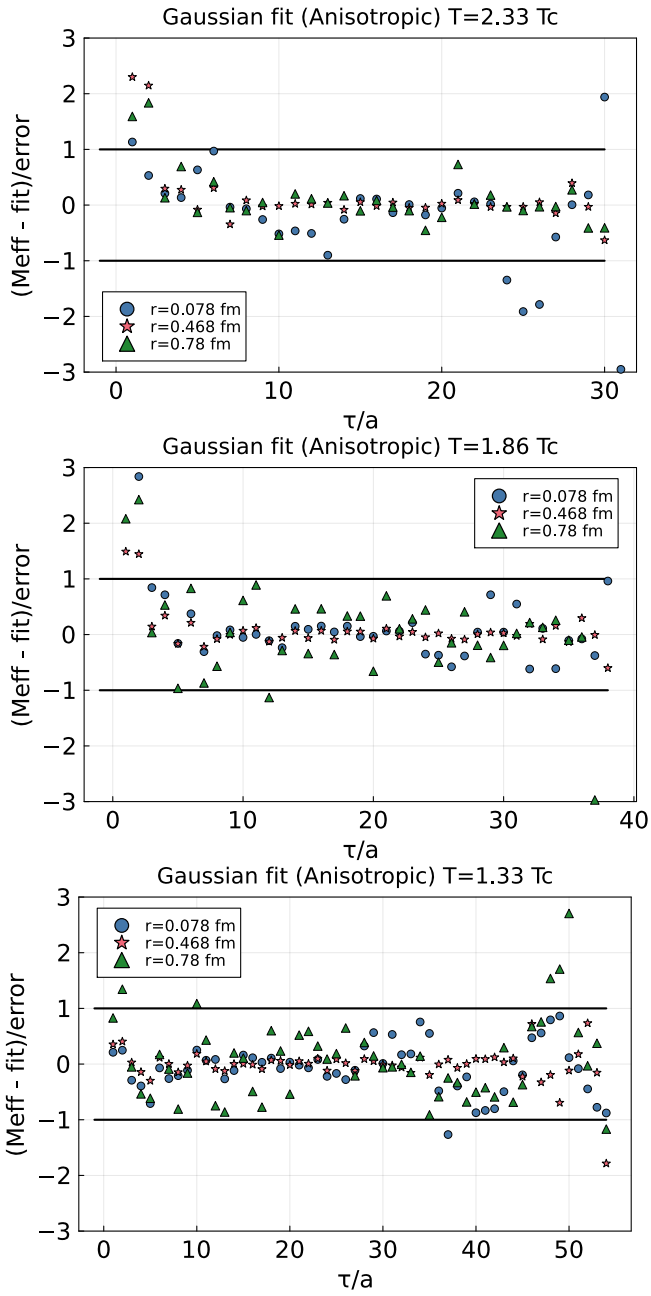

Figure 4.25: Goodness of gaussian fit on subtracted anisotropic lattices at three different separation distances.

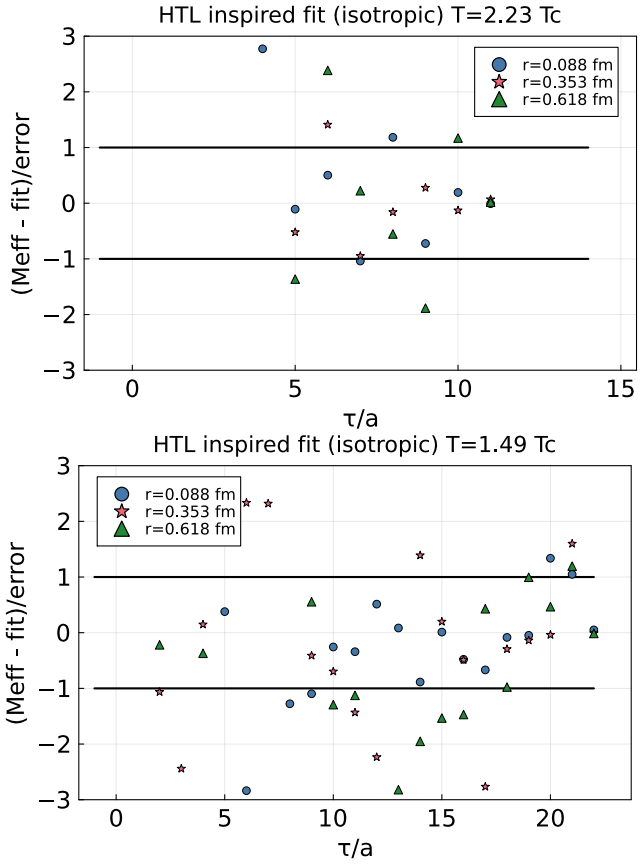

Figure 4.26: Goodness of HTL inspired fit on isotropic lattices at three different separation distances.

inspired fits on isotropic and anisotropic lattices respectively. See eq. (2.23) for the fit form. We observe that the form fits the data quite well through a large τ range outside of $\tau = \beta/2$. The fitting range is increased with decreasing temperature.

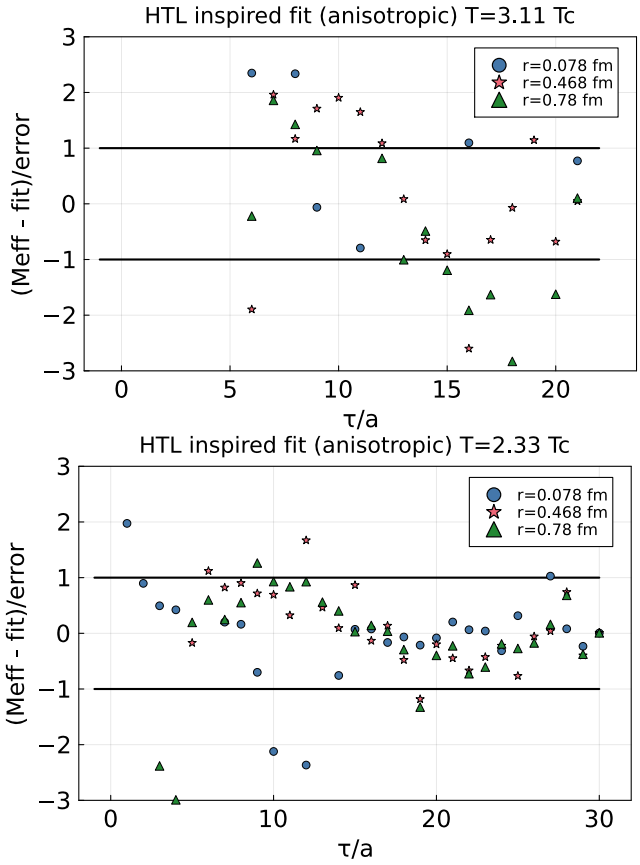

Figure 4.27: Goodness of HTL inspired fit on anisotropic lattices at three different separation distances.

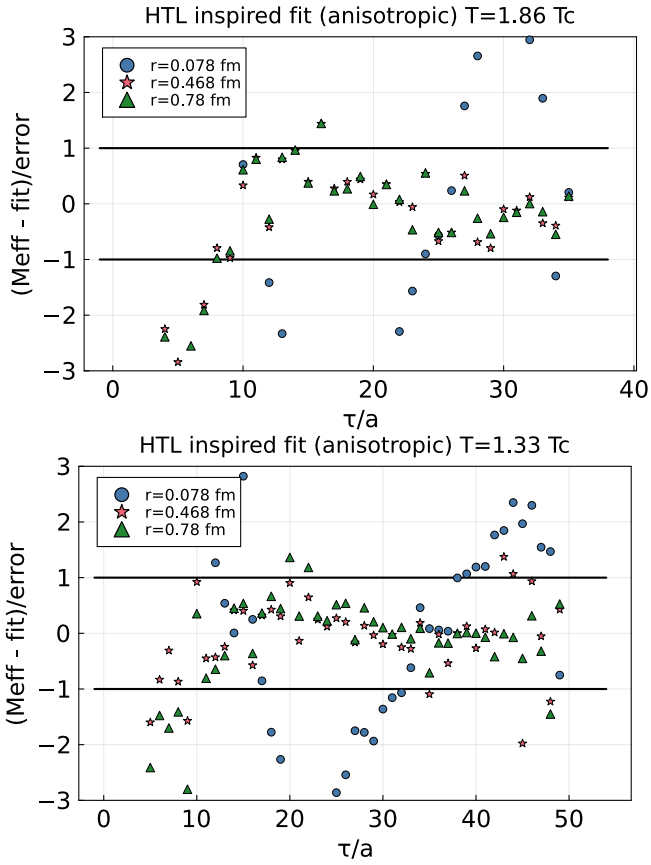

Figure 4.28: Goodness of HTL inspired fit on anisotropic lattices at three different separation distances.

5 Conclusion

In this thesis, we have studied the in-medium properties of the bound state of the quark and anti-quark pair (quarkonium) through the static potential. The central challenge that we address is to establish whether such a potential model exists at finite temperature and if it does what is the functional form of such a potential.

We have presented extraction methods of the static heavy quark potential from lattice QCD. We started with defining the potential as a Wilson coefficient of an effective theory of heavy quarkonium called pNRQCD. The complex potential can be described through the Wilson loop in Miknowski time. This Wilson loop correlator can be linked with the Euclidean Wilson loop via the spectral function. The real part of the potential is linked to the position of the dominant peak in the spectral function and the imaginary part is linked to the width of this dominant peak. Computation of the spectral function from finite number of discrete and noisy Euclidean lattice data is an ill-posed inverse problem. In chapter 2 we discussed, and bench-marked different four different independent methods i.e *Bayesian BR method, Padé interpolation, HTL inspired fits* and *Gaussian fits and zero temperature subtraction* for the extraction of spectral function from lattice data. Later, as the main part of the thesis, we presented two recent studies based on these four extraction methods, the first one on state of the art 2+1 flavour lattices based on the Luscher-Weisz gauge action and the HISQ fermionic action and the other being on Quenched lattices with the Wilson action.

The first study discussed in chapter 3 and published in [49] showed the existence of a complex potential with an unscreened real-part and an imaginary part that increases with temperature and separation distance. These results were very different from those observed on previous studies on both quenched and full QCD with asqtad action. The BR method was rendered inapplicable for this study due to the non-positivity of the spectral function manifested in non-monotonicity of effective masses

at high temperatures. This motivated us to re-investigate the potential on quenched lattices in chapter 4 and confirm the robustness of our methods and compare them to the BR method as it was used it those previous studies. This was possible due to the absence of non-monotonicity in effective masses of the Wilson line correlator, which made the BR method applicable in the quenched case. Our studies using the BR, Padé, and HTL inspired method confirmed results from previous studies showing the presence of a complex potential with a screened real part. However, when we performed the analysis on the subtracted correlator, the Padé, BR and the Gaussian fits all showed the presence of a complex potential but now with an unscreened real part.

Clearly, the subtraction procedure has a non-trivial effect on the spectral function and thus affects the behaviour of the extracted potential quite drastically. The subtraction procedure in the Quenched study on anisotropic lattices is not as exact as with the HISQ study as the effective masses at small τ do not line up exactly, this disagreement disappears in isotropic lattices. In our study, we observed that the subtraction procedure indeed removes structures at high frequencies, but also affect the lowest lying peak. More work is needed to fully understand the effect of the subtraction procedure on the reconstruction of the spectral function.

Through both these studies with all our methods, we have also established that the potential is indeed complex, with the imaginary part growing with temperature and separation distance in both full QCD and quenched QCD (in quenched only for $T > T_c$). This is manifested by the presence of a finite width in the spectral function reconstruction and through a non-zero slope in the effective masses. However, we are still far away from determining the imaginary part of the spectral function accurately with the current data quality. None of our methods agree with each other on the imaginary part of the potential or width of spectral function.

The results from 2+1 flavour QCD lattices [49] were used in [81]

between the potential to experimental observables. Yeilds and nuclear modification factors R_{AA} of bottomonium in Pb-Pb collisions were calculated at $\sqrt{s_{NN}} = 5.02$ TeV. Calculations showed a large suppression of nuclear modification factors when compared to experiment. These calculations where done with bottomonium formation time of $\tau_\Upsilon = 0.6$ fm/c which is the start time of hydrodynamics. However, when a large

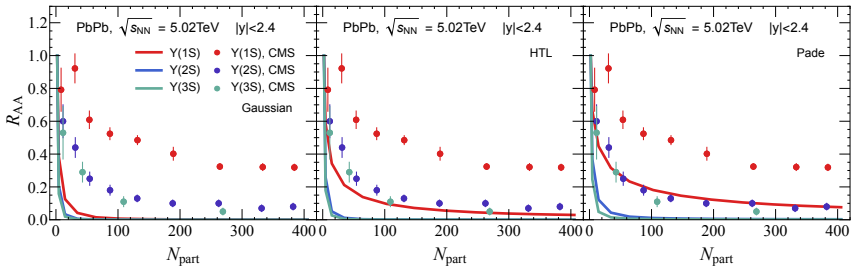

Figure 5.1: The nuclear modification factors of bottomonium $\Upsilon(1s, 2s, 3s)$ as a function of the number of participants N_{part} in the central rapidity of Pb-Pb collisions at $\sqrt{s_{\text{NN}}} = 5.02$TeV. The potential is taken from Gaussian fits (left), HTL inspired method (middle) and Padé fits (right) with $\tau_\Upsilon = 0.6$ fm/c [81].

formation time of $\tau_\Upsilon = 3$ fm/c the suppression of R_{AA} is reduced and the calculations with the Padé fit agree well with experimental data. Phenomenological modelling of the unscreened potential with an

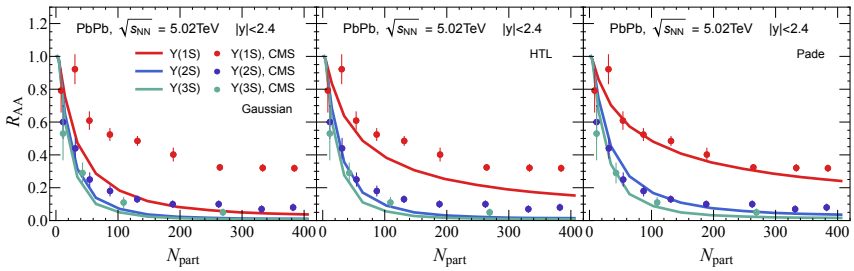

Figure 5.2: Same as fig. 5.1 but with $\tau_\Upsilon = 3$ fm/c.

imaginary part currently does not agree with experimental data given a realistic formation time.

References

[1] N. Haque, *Some Applications of Hard Thermal Loop Perturbation Theory in Quark Gluon Plasma*. PhD thesis, Saha Inst., 7 2014.

[2] E. Witten, "Cosmic Separation of Phases," *Phys. Rev. D*, vol. 30, pp. 272–285, 1984.

[3] E. Annala, T. Gorda, A. Kurkela, J. Nättilä, and A. Vuorinen, "Evidence for quark-matter cores in massive neutron stars," *Nature Phys.*, vol. 16, no. 9, pp. 907–910, 2020.

[4] J. N. Guenther, "Overview of the QCD phase diagram: Recent progress from the lattice," *Eur. Phys. J. A*, vol. 57, no. 4, p. 136, 2021.

[5] A. Bazavov, P. Petreczky, and J. H. Weber, "Equation of State in 2+1 Flavor QCD at High Temperatures," *Phys. Rev. D*, vol. 97, no. 1, p. 014510, 2018.

[6] J. E. Bernhard, J. S. Moreland, S. A. Bass, J. Liu, and U. Heinz, "Applying Bayesian parameter estimation to relativistic heavy-ion collisions: simultaneous characterization of the initial state and quark-gluon plasma medium," *Phys. Rev. C*, vol. 94, no. 2, p. 024907, 2016.

[7] A. Rothkopf, "Heavy Quarkonium in Extreme Conditions," *Phys. Rept.*, vol. 858, pp. 1–117, 2020.

[8] F. Gelis, E. Iancu, J. Jalilian-Marian, and R. Venugopalan, "The Color Glass Condensate," *Ann. Rev. Nucl. Part. Sci.*, vol. 60, pp. 463–489, 2010.

[9] E. Shuryak, "Why does the quark gluon plasma at RHIC behave as a nearly ideal fluid?," *Prog. Part. Nucl. Phys.*, vol. 53, pp. 273–303, 2004.

[10] A. Bazavov *et al.*, "Chiral crossover in QCD at zero and non-zero chemical potentials," *Phys. Lett. B*, vol. 795, pp. 15–21, 2019.

[11] G. I. Veres, "Heavy ion physics at CMS and ATLAS: hard probes," in *54th Rencontres de Moriond on QCD and High Energy Interactions*, pp. 229–232, ARISF, 5 2019.

[12] A. Tumasyan *et al.*, "Observation of the Υ(3S) meson and suppression of Υ states in PbPb collisions at $\sqrt{s_{\mathrm{NN}}}$ = 5.02 TeV," 3 2023.

[13] T. Matsui and H. Satz, "J/ψ Suppression by Quark-Gluon Plasma Formation," *Phys. Lett.*, vol. B178, pp. 416–422, 1986.

[14] T. Hashimoto, O. Miyamura, K. Hirose, and T. Kanki, "Mass shift of charmonium near deconfining temperature and possible detection in lepton-pair production," *Phys. Rev. Lett.*, vol. 57, pp. 2123–2126, Oct 1986.

[15] F. Becattini, "An Introduction to the Statistical Hadronization Model," in *International School on Quark-Gluon Plasma and Heavy Ion Collisions: past, present, future*, 1 2009.

[16] P. Braun-Munzinger and J. Stachel, "Charmonium from Statistical Hadronization of Heavy Quarks – a Probe for Deconfinement in the Quark-Gluon Plasma," *Landolt-Bornstein*, vol. 23, p. 424, 2010.

[17] A. Andronic, P. Braun-Munzinger, K. Redlich, and J. Stachel, "The statistical model in Pb-Pb collisions at the LHC," *Nucl. Phys. A*, vol. 904-905, pp. 535c–538c, 2013.

[18] C. E. Berger, L. Rammelmüller, A. C. Loheac, F. Ehmann, J. Braun, and J. E. Drut, "Complex Langevin and other approaches to the sign problem in quantum many-body physics," *Phys. Rept.*, vol. 892, pp. 1–54, 2021.

[19] W. Caswell and G. Lepage, "Effective Lagrangians for Bound State Problems in QED, QCD, and Other Field Theories," *Phys. Lett. B*, vol. 167, pp. 437–442, 1986.

[20] G. T. Bodwin, E. Braaten, and G. P. Lepage, "Rigorous QCD analysis of inclusive annihilation and production of heavy quarkonium," *Phys. Rev. D*, vol. 51, pp. 1125–1171, 1995. [Erratum: Phys.Rev.D 55, 5853 (1997)].

[21] C. T. H. Davies, K. Hornbostel, A. Langnau, G. P. Lepage, A. Lidsey, J. Shigemitsu, and J. H. Sloan, "Precision Upsilon spectroscopy from nonrelativistic lattice QCD," *Phys. Rev.*, vol. D50, pp. 6963–6977, 1994.

[22] N. Brambilla, A. Pineda, J. Soto, and A. Vairo, "Potential NRQCD: An Effective theory for heavy quarkonium," *Nucl. Phys. B*, vol. 566, p. 275, 2000.

[23] N. Brambilla, M. A. Escobedo, J. Soto, and A. Vairo, "Quarkonium suppression in heavy-ion collisions: an open quantum system approach," *Phys. Rev. D*, vol. 96, no. 3, p. 034021, 2017.

[24] N. Brambilla, M. A. Escobedo, J. Soto, and A. Vairo, "Heavy quarkonium suppression in a fireball," *Phys. Rev. D*, vol. 97, no. 7, p. 074009, 2018.

[25] N. Brambilla, M. A. Escobedo, A. Vairo, and P. Vander Griend, "Transport coefficients from in medium quarkonium dynamics," *Phys. Rev. D*, vol. 100, no. 5, p. 054025, 2019.

[26] N. Brambilla, M. A. Escobedo, M. Strickland, A. Vairo, P. Vander Griend, and J. H. Weber, "Bottomonium suppression in an open quantum system using the quantum trajectories method," *JHEP*, vol. 05, p. 136, 2021.

[27] Y. Akamatsu, "Quarkonium in Quark-Gluon Plasma: Open Quantum System Approaches Re-examined," 9 2020.

[28] M. Laine, O. Philipsen, P. Romatschke, and M. Tassler, "Real-time static potential in hot QCD," *JHEP*, vol. 03, p. 054, 2007.

[29] C. Gattringer, R. Hoffmann, and S. Schaefer, "Setting the scale for the Luscher-Weisz action," *Phys. Rev. D*, vol. 65, p. 094503, 2002.

[30] G. P. Lepage and P. B. Mackenzie, "Viability of lattice perturbation theory," *Phys. Rev. D*, vol. 48, pp. 2250–2264, Sep 1993.

[31] H. B. Nielsen and M. Ninomiya, "Absence of Neutrinos on a Lattice. 1. Proof by Homotopy Theory," *Nucl. Phys. B*, vol. 185, p. 20, 1981. [Erratum: Nucl.Phys.B 195, 541 (1982)].

[32] H. B. Nielsen and M. Ninomiya, "Absence of Neutrinos on a Lattice. 2. Intuitive Topological Proof," *Nucl. Phys. B*, vol. 193, pp. 173–194, 1981.

[33] E. Follana, Q. Mason, C. Davies, K. Hornbostel, G. P. Lepage, J. Shigemitsu, H. Trottier, and K. Wong, "Highly improved staggered quarks on the lattice, with applications to charm physics," *Phys. Rev. D*, vol. 75, p. 054502, 2007.

[34] A. Ali Khan *et al.*, "Equation of state in finite temperature QCD with two flavors of improved Wilson quarks," *Phys. Rev. D*, vol. 64, p. 074510, 2001.

[35] A. Rothkopf, T. Hatsuda, and S. Sasaki, "Proper heavy-quark potential from a spectral decomposition of the thermal Wilson loop," *PoS*, vol. LAT2009, p. 162, 2009.

[36] A. Rothkopf, T. Hatsuda, and S. Sasaki, "Complex Heavy-Quark Potential at Finite Temperature from Lattice QCD," *Phys. Rev. Lett.*, vol. 108, p. 162001, 2012.

[37] Y. Burnier and A. Rothkopf, "Complex heavy-quark potential and Debye mass in a gluonic medium from lattice QCD," *Phys. Rev. D*, vol. 95, no. 5, p. 054511, 2017.

[38] A. Bazavov, D. Hoying, O. Kaczmarek, R. N. Larsen, S. Mukherjee, P. Petreczky, A. Rothkopf, and J. H. Weber, "Un-screened forces in Quark-Gluon Plasma?," 8 2023.

[39] L. Mazur, *Topological Aspects in Lattice QCD*. PhD thesis, Bielefeld U., 2021.

[40] R. N. Larsen, G. Parkar, A. Rothkopf, and J. H. Weber, "In-medium static inter-quark potential on high resolution quenched lattices," 2 2024.

[41] Y. Burnier and A. Rothkopf, "Bayesian Approach to Spectral Function Reconstruction for Euclidean Quantum Field Theories," *Phys. Rev. Lett.*, vol. 111, p. 182003, 2013.

[42] L. Schlessinger, "Use of analyticity in the calculation of nonrelativistic scattering amplitudes," *Phys. Rev.*, vol. 167, pp. 1411–1423, Mar 1968.

[43] D. Bala and S. Datta, "Nonperturbative potential for the study of quarkonia in QGP," *Phys. Rev. D*, vol. 101, no. 3, p. 034507, 2020.

[44] D. Bala and S. Datta, "Effective thermal potential between static Q and $\bar{Q}$ in SU(3) gauge theory," *PoS*, vol. LATTICE2019, p. 164, 2019.

[45] R. Larsen, S. Meinel, S. Mukherjee, and P. Petreczky, "Thermal broadening of bottomonia: Lattice nonrelativistic QCD with extended operators," *Phys. Rev. D*, vol. 100, no. 7, p. 074506, 2019.

[46] Y. Burnier and A. Rothkopf, "A hard thermal loop benchmark for the extraction of the nonperturbative $Q\bar{Q}$ potential," *Phys. Rev.*, vol. D87, p. 114019, 2013.

[47] M. Asakawa, T. Hatsuda, and Y. Nakahara, "Maximum entropy analysis of the spectral functions in lattice QCD," *Prog. Part. Nucl. Phys.*, vol. 46, pp. 459–508, 2001.

[48] D. Dudal, O. Oliveira, M. Roelfs, and P. Silva, "Spectral representation of lattice gluon and ghost propagators at zero temperature," *Nucl. Phys. B*, vol. 952, p. 114912, 2020.

[49] D. Bala *et al.*, "Static quark-antiquark interactions at nonzero temperature from lattice QCD," *Phys. Rev. D*, vol. 105, no. 5, p. 054513, 2022.

[50] A. K. Cyrol, J. M. Pawlowski, A. Rothkopf, and N. Wink, "Reconstructing the gluon," *SciPost Phys.*, vol. 5, no. 6, p. 065, 2018.

[51] R. Larsen, S. Meinel, S. Mukherjee, and P. Petreczky, "Excited bottomonia in quark-gluon plasma from lattice QCD," *Phys. Lett. B*, vol. 800, p. 135119, 2020.

[52] A. P. Valentine and M. Sambridge, "Gaussian process models—I. A framework for probabilistic continuous inverse theory," *Geophysical Journal International*, vol. 220, pp. 1632–1647, 11 2019.

[53] J. Horak, J. M. Pawlowski, J. Rodríguez-Quintero, J. Turnwald, J. M. Urban, N. Wink, and S. Zafeiropoulos, "Reconstructing QCD spectral functions with Gaussian processes," *Phys. Rev. D*, vol. 105, no. 3, p. 036014, 2022.

[54] F. Gao and J. M. Pawlowski, "Qcd phase structure from functional methods," *Phys. Rev. D*, vol. 102, p. 034027, Aug 2020.

[55] F. Gao, J. Papavassiliou, and J. M. Pawlowski, "Fully coupled functional equations for the quark sector of QCD," *Phys. Rev. D*, vol. 103, no. 9, p. 094013, 2021.

[56] J. Horak, J. Papavassiliou, J. M. Pawlowski, and N. Wink, "Ghost spectral function from the spectral Dyson-Schwinger equation," *Phys. Rev. D*, vol. 104, 2021.

[57] J. Fei, C.-N. Yeh, and E. Gull, "Nevanlinna analytical continuation," *Physical Review Letters*, vol. 126, feb 2021.

[58] L. Kades, J. M. Pawlowski, A. Rothkopf, M. Scherzer, J. M. Urban, S. J. Wetzel, N. Wink, and F. P. Ziegler, "Spectral reconstruction with deep neural networks," *Physical Review D*, vol. 102, nov 2020.

[59] M. Hansen, A. Lupo, and N. Tantalo, "Extraction of spectral densities from lattice correlators," *Physical Review D*, vol. 99, may 2019.

[60] R.-A. Tripolt, I. Haritan, J. Wambach, and N. Moiseyev, "Threshold energies and poles for hadron physical problems by a model-independent universal algorithm," *Phys. Lett. B*, vol. 774, pp. 411–416, 2017.

[61] Y. Burnier, O. Kaczmarek, and A. Rothkopf, "Static quark-antiquark potential in the quark-gluon plasma from lattice QCD," *Phys. Rev. Lett.*, vol. 114, no. 8, p. 082001, 2015.

[62] Y. Burnier, O. Kaczmarek, and A. Rothkopf, "Quarkonium at finite temperature: Towards realistic phenomenology from first principles," *JHEP*, vol. 12, p. 101, 2015.

[63] A. Bazavov, Y. Burnier, and P. Petreczky, "Lattice calculation of the heavy quark potential at non-zero temperature," *Nucl. Phys.*, vol. A932, pp. 117–121, 2014.

[64] P. Petreczky and J. Weber, "Lattice Calculations of Heavy Quark Potential at Finite Temperature," *Nucl. Phys. A*, vol. 967, pp. 592–595, 2017.

[65] A. Bazavov *et al.*, "The chiral and deconfinement aspects of the QCD transition," *Phys. Rev.*, vol. D85, p. 054503, 2012.

[66] A. Bazavov, H. T. Ding, P. Hegde, F. Karsch, C. Miao, S. Mukherjee, P. Petreczky, C. Schmidt, and A. Velytsky, "Quark number susceptibilities at high temperatures," *Phys. Rev. D*, vol. 88, no. 9, p. 094021, 2013.

[67] A. Bazavov *et al.*, "Equation of state in (2+1)-flavor QCD," *Phys. Rev.*, vol. D90, p. 094503, 2014.

[68] H. T. Ding, S. Mukherjee, H. Ohno, P. Petreczky, and H. P. Schadler, "Diagonal and off-diagonal quark number susceptibilities at high temperatures," *Phys. Rev. D*, vol. 92, no. 7, p. 074043, 2015.

[69] A. Bazavov, N. Brambilla, P. Petreczky, A. Vairo, and J. H. Weber, "Color screening in (2+1)-flavor QCD," *Phys. Rev. D*, vol. 98, no. 5, p. 054511, 2018.

[70] A. Bazavov *et al.*, "Determination of the QCD coupling from the static energy and the free energy," *Phys. Rev. D*, vol. 100, no. 11, p. 114511, 2019.

[71] A. Bazavov *et al.*, "Results for light pseudoscalar mesons," *PoS*, vol. LATTICE2010, p. 074, 2010.

[72] R. Larsen, S. Meinel, S. Mukherjee, and P. Petreczky, "Bethe-Salpeter amplitudes of Upsilons," *Phys. Rev. D*, vol. 102, p. 114508, 2020.

[73] S. Shi, K. Zhou, J. Zhao, S. Mukherjee, and P. Zhuang, "Heavy Quark Potential in QGP: DNN meets LQCD," 5 2021.

[74] D. Bala and S. Datta, "Interaction potential between heavy $Q\overline{Q}$ in a color octet configuration in the QGP from a study of hybrid Wilson loops," *Phys. Rev. D*, vol. 103, no. 1, p. 014512, 2021.

[75] P. Petreczky, A. Rothkopf, and J. Weber, "Realistic in-medium heavy-quark potential from high statistics lattice QCD simulations," *Nucl. Phys. A*, vol. 982, pp. 735–738, 2019.

[76] Y. Burnier, H. T. Ding, O. Kaczmarek, A. L. Kruse, M. Laine, H. Ohno, and H. Sandmeyer, "Thermal quarkonium physics in the pseudoscalar channel," *JHEP*, vol. 11, p. 206, 2017.

[77] J. R. Glesaaen and B. Jäger, "openqcd-fastsum," Dec. 2018.

[78] L. Mazur *et al.*, "SIMULATeQCD: A simple multi-GPU lattice code for QCD calculations," 6 2023.

[79] N. Brambilla, R. L. Delgado, A. S. Kronfeld, V. Leino, P. Petreczky, S. Steinbeißer, A. Vairo, and J. H. Weber, "Static energy in $(2+1+1)$-flavor lattice QCD: Scale setting and charm effects," *Phys. Rev. D*, vol. 107, no. 7, p. 074503, 2023.

[80] S. Kim, P. Petreczky, and A. Rothkopf, "Lattice NRQCD study of S- and P-wave bottomonium states in a thermal medium with $N_f = 2 + 1$ light flavors," *Phys. Rev. D*, vol. 91, p. 054511, 2015.

[81] G. Chen, B. Chen, and J. Zhao, "Bottomonium evolution with in-medium heavy quark potential from lattice QCD," 2 2024.